

---

### 1.1 One-Degree-of-Freedom Model

The mass–spring–damper model, shown in Figure 1.1, is the *starting point* for understanding mechanical vibrations. A thorough understanding of this most elementary vibration model and its full range of vibration characteristics is absolutely essential to a comprehensive and insightful study of the rotating machinery vibration field. The fundamental physical law governing all vibration phenomena is Newton’s Second Law, which in its most commonly used form says that *the sum of the forces acting upon an object is equal to its mass times its acceleration*. Both force and acceleration are vectors, so Newton’s Second Law, written in its general form, yields a vector equation. For the one-degree-of-freedom (1-DOF) system, this reduces to a scalar equation, as follows:

$$F = ma \quad (1.1)$$

where  $F$  is the sum of forces acting upon the body,  $m$  is the mass of the body, and  $a$  is the acceleration of the body.

For the system in Figure 1.1,  $F = ma$  yields its differential equation of motion as follows:

$$m\ddot{x} + c\dot{x} + kx = f(t) \quad (1.2)$$

For the system in Figure 1.1, the forces acting upon the mass include the externally applied time-dependent force,  $f(t)$ , plus the spring and damper motion-dependent connection forces,  $-kx$  and  $-c\dot{x}$ . Here, the minus signs account for the spring force resisting displacement ( $x$ ) in either direction from the equilibrium position and the damper force resisting velocity ( $\dot{x}$ ) in either direction. The weight ( $mg$ ) and static deflection force ( $k\delta_{st}$ ) that the weight causes in the spring cancel each other. Equations of motion are generally written about the static equilibrium position state and then need not contain weight and weight-balancing spring deflection forces.

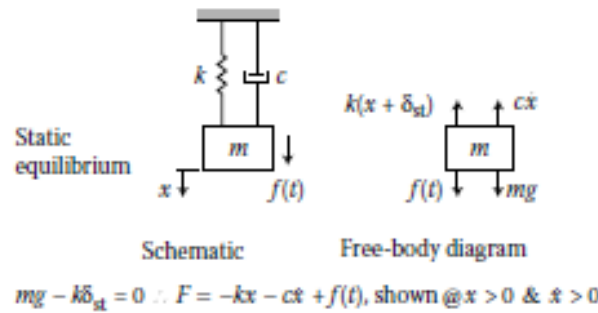


FIGURE 1.1 One-DOF linear spring-mass-damper model.

to) their respective driving parameters, that is, displacement ( $x$ ) across the spring and velocity ( $\dot{x}$ ) across the damper. These forces are therefore related to their respective driving parameters by proportionality factors, stiffness “ $k$ ” for the spring and “ $c$ ” for the damper. Linearity is a simplifying assumption that permeates most vibration analyses because the *equations of motion* are then made *linear*, even though real systems are never completely linear. Fortunately, the assumption of linearity leads to adequate answers in most vibration engineering analyses and simplifies considerably the tasks of making calculations and understanding what is calculated. Some specialized large-amplitude rotor vibration problems justify treating nonlinear effects, for example, large rotor unbalance such as from turbine blade loss, shock and seismic base-motion excitations, rotor rub-impact phenomena, and instability vibration limit cycles. These topics are treated in subsequent sections of this book.

### 1.1.2 Unforced System

The solution for the motion of the *unforced 1-DOF system* is important in its own right, but specifically important in laying the groundwork to study *self-excited instability rotor vibrations*. If the system is considered to be *unforced*, then  $f(t) = 0$  and Equation 1.2 becomes

$$m\ddot{x} + c\dot{x} + kx = 0 \quad (1.3)$$

This is a second-order homogeneous ordinary differential equation (ODE). To solve for  $x(t)$  from Equation 1.3, one needs to specify the two initial conditions,  $x(0)$  and  $\dot{x}(0)$ . Assuming that  $k$  and  $c$  are both positive, there are three categories of solutions that can result from Equation 1.3: (i) *underdamped*, (ii) *critically damped*, and (iii) *overdamped*. These are just the traditional labels used to describe the three distinct types of roots and the corresponding three motion categories that Equation 1.3 can potentially yield when  $k$  and  $c$  are both positive. Substituting the known solution form

$(Ce^{\lambda t})$  into Equation 1.3 and then canceling out the solution form yields the following quadratic equation for its roots (eigenvalues) and leads to the equation for the extracted two roots,  $\lambda_{1,2}$ , as follows:

$$m\lambda^2 + c\lambda + k = 0 \quad (1.4)$$

$$\lambda_{1,2} = -\frac{c}{2m} \pm \sqrt{\left(\frac{c}{2m}\right)^2 - \left(\frac{k}{m}\right)}$$

The three categories of root types possible from Equation 1.4 are listed as follows:

*Underdamped:*  $(c/2m)^2 \leq (k/m)$ , complex conjugate roots,  $\lambda_{1,2} = \alpha \pm i\omega_d$ .

*Critically damped:*  $(c/2m)^2 = (k/m)$ , equal real roots,  $\lambda_{1,2} = \alpha$ .

*Overdamped:*  $(c/2m)^2 \geq (k/m)$ , real roots,  $\lambda_{1,2} = \alpha \pm \beta$ .

The well-known  $x(t)$  time signals for these three solution categories are illustrated in Figure 1.2 along with the *undamped* system (i.e.,  $c = 0$ ). In most mechanical systems, the important vibration characteristics are contained in modes with the so-called *underdamped* roots, as is certainly the case for rotor dynamical systems. The general expression for the motion of the *unforced underdamped* system is commonly expressed in any one of the following four forms:

$$x(t) = Xe^{\alpha t} \begin{cases} \sin(\omega_d t + \phi_s^+) \text{ or } \sin(\omega_d t - \phi_s^-) \\ \text{OR} \\ \cos(\omega_d t + \phi_c^+) \text{ or } \cos(\omega_d t - \phi_c^-) \end{cases} \quad (1.5)$$

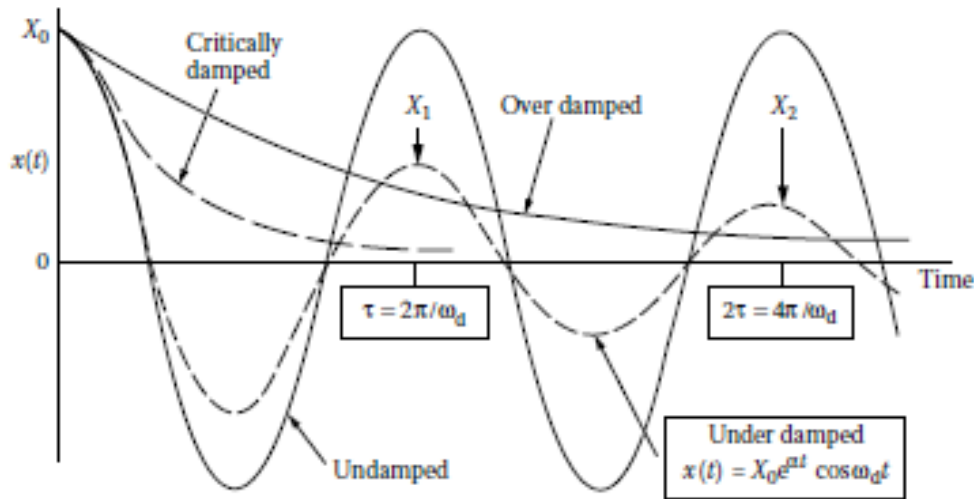


FIGURE 1.2 Motion types for the unforced 1-DOF system.

### 1.1.5 Damping

Mechanical vibratory systems typically fall into the *underdamped* category, so each individual system mode of importance can thereby be accurately handled in the modal-coordinate space (Section 1.3 of this chapter) as the 1-DOF model illustrated in Figure 1.1. This is convenient since modern digital signal processing methods can separate out each mode's *underdamped* exponential decay signal from a total transient (e.g., impact initiated) time-base vibration test signal. Each mode's linear damping coefficient can then be determined employing the *log-decrement* method, as outlined here. Referring to Figures 1.2 and 1.4c, test data for a mode's *underdamped* exponential decay signal can be used to determine the damping

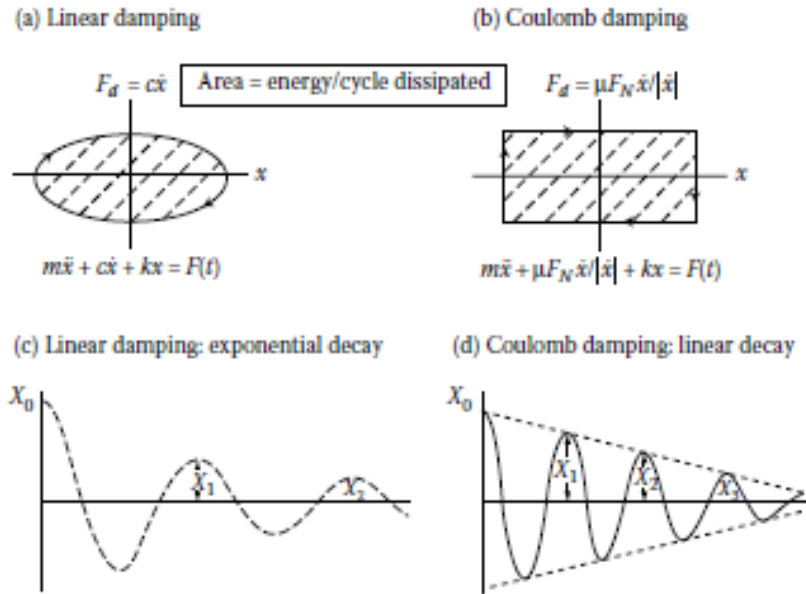


FIGURE 1.4 Damped decay and energy dissipated per cycle of periodic motion.

coefficient as follows:

$$x(n\tau) = X_0 e^{\alpha n\tau}, \quad \therefore \frac{x(n\tau)}{x(0)} = e^{\alpha n\tau}, \quad \therefore \alpha n\tau = \ln \left( \frac{X_n}{X_0} \right)$$

$$1 - \text{cycle period} \equiv \tau = \frac{2\pi}{\omega_d}$$

$$\text{Recalling } \alpha = -\frac{c}{2m} \text{ yields the damping coefficient } c = -\frac{2m}{n\tau} \ln \left( \frac{X_n}{X_0} \right) \quad (1.8)$$

coefficient as follows:

$$\begin{aligned}
 x(n\tau) &= X_0 e^{\alpha n\tau}, \quad \therefore \frac{x(n\tau)}{x(0)} = e^{\alpha n\tau}, \quad \therefore \alpha n\tau = \ln \left( \frac{X_n}{X_0} \right) \\
 1 - \text{cycle period} &\equiv \tau = \frac{2\pi}{\omega_d} \\
 \text{Recalling } \alpha &= -\frac{c}{2m} \text{ yields the damping coefficient } c = -\frac{2m}{n\tau} \ln \left( \frac{X_n}{X_0} \right)
 \end{aligned}
 \tag{1.8}$$

Vibration damping means are extremely important in nature as well as engineered devices. The standard linear model for damping is akin to a drag force proportional to velocity magnitude. But many important damping mechanisms are nonlinear, for example, Coulomb damping, internal material hysteresis damping. What is typically done to handle the modeling of nonlinear damping is to approximate it with the linear model by matching energy dissipated per cycle. This works well since modest amounts of damping have negligible effect on natural frequency. Energy/cycle dissipated by damping under single-frequency harmonic cycling is illustrated in Figure 1.4 for linear and Coulomb friction damping.

The *log-decrement* test method for determining damping was previously shown to utilize the transient decay motion of an initially displaced but unforced system. In contrast, the *half power bandwidth* test method utilizes the steady-state response to a harmonic excitation force. The steady-state linear response to a single-frequency harmonic excitation force of slowly varied frequency will correspond to a member of the family displayed in Figure 1.5a. For the single-DOF linear damped model, the following equation is applicable for low damped systems:

$$\begin{aligned}
 Q &\equiv \frac{\text{Frequency at peak vibration amplitude}}{\omega_2 - \omega_1} = \frac{1}{2\zeta} \\
 Q &\equiv \frac{\omega_{\text{peak}}}{\omega_2 - \omega_1} = \frac{1}{2\zeta}
 \end{aligned}
 \tag{1.9}$$

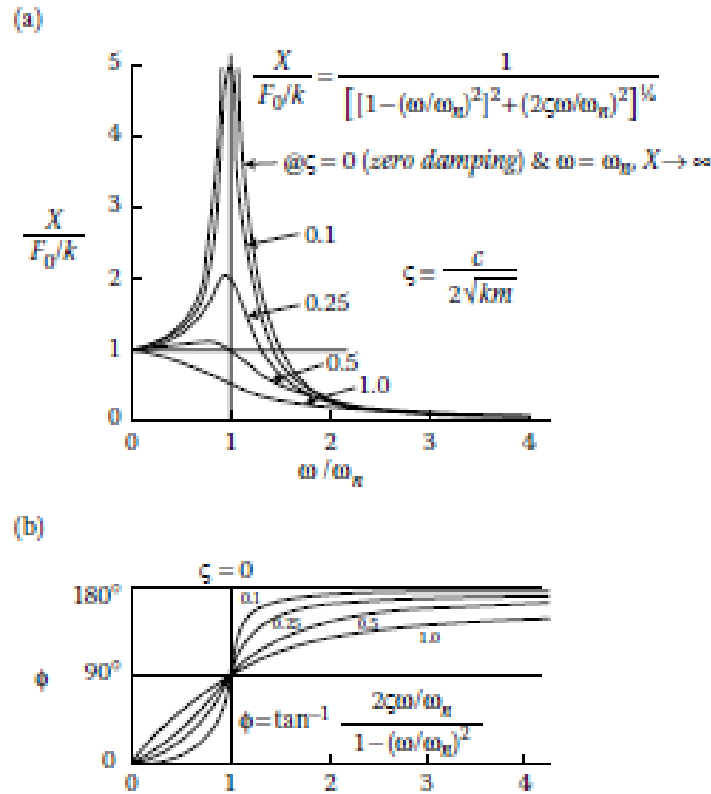


FIGURE 1.5 One-DOF steady-state response to a sinusoidal force. (a)  $X/(F_0/k)$  versus  $\omega/\omega_n$ , (b)  $\phi$  versus  $\omega/\omega_n$ ,  $\zeta = 1$  at critically damped.

sharpness-of-peak of a measured steady-state plot of vibration amplitude versus frequency provides a measure of the damping present.

### 1.1.6 Undamped Natural Frequency: An Accurate Approximation

Because of the modest amounts of damping typical of most mechanical systems, the undamped model provides good answers for natural frequencies in most situations. Figure 1.5 shows that the natural frequency of the 1-DOF model is the frequency at which an excitation force produces maximum vibration (i.e., a *forced resonance*) and is thus important. As shown in a subsequent topic of this chapter (*Modal Decomposition*), each natural mode of an undamped multi-DOF model is exactly equivalent to an undamped 1-DOF model. Therefore, the accurate approximation now shown for the 1-DOF model is usually applicable to the important modes of multi-DOF models.

The ratio ( $\zeta$ ) of *damping to critical damping* (frequently referenced as a percentage, e.g.,  $\zeta = 0.1$  is “10% damping”) is derivable as follows. Shown with Equation 1.4, the defined condition for “critically damped” is  $(c/2m)^2 = (k/m)$ , which yields  $c = 2\sqrt{km} \equiv c_c$ , the “critical damping.”

Therefore, the *damping ratio*, defined as  $\zeta \equiv c/c_c$ , can be expressed as follows:

$$\zeta \equiv \frac{c}{2\sqrt{km}} \quad (1.10)$$

With Equations 1.4 and 1.5, the following were defined:  $\omega_n = \sqrt{k/m}$  (undamped natural frequency),  $\alpha = -c/2m$  (real part of eigenvalue for an underdamped system), and  $\omega_d = \sqrt{\omega_n^2 - \alpha^2}$  (damped natural frequency). Using these expressions with Equation 1.10 for the damping ratio ( $\zeta$ ) leads directly to the following formula for the damped natural frequency:

$$\omega_d = \omega_n \sqrt{1 - \zeta^2} \quad (1.11)$$

This well-known important formula clearly shows just how well the *undamped natural frequency* approximates the *damped natural frequency* for typical applications. For example, a generous damping estimate for most potentially resonant mechanical system modes is 10–20% of critical damping ( $\zeta = 0.1$ – $0.2$ ). Substituting the values  $\zeta = 0.1$  and  $0.2$  into Equation 1.11 gives  $\omega_d = 0.995\omega_n$  for 10% damping and  $\omega_d = 0.98\omega_n$  for 20% damping, that is, 0.5% error and 2% error, respectively. For even smaller damping ratio values typical of many structures, the approximation just gets better. A fundamentally important and powerful *dichotomy*, applicable to the important modes of many mechanical and structural vibratory systems, becomes clear within the context of this accurate approximation: *A natural frequency is only slightly lowered by the damping, but the peak vibration caused by an excitation force at the natural frequency is overwhelmingly lowered by the damping.* Figure 1.5 clearly shows all this.



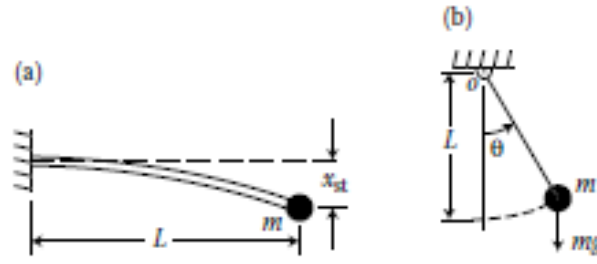


FIGURE 1.6 Two examples treated as linear 1-DOF models: (a) cantilever beam with a concentrated end mass and (b) simple pendulum.

a 1-DOF model. For *small* transverse static deflections ( $x_{st}$ ) at the free end of the cantilever beam resulting from a transverse static load ( $F_{st}$ ) at its free end, the equivalent spring stiffness is obtained directly from the cantilever beam's static deflection formula. This leads directly to the equivalent 1-DOF undamped system equation of motion, from which its undamped *natural frequency* ( $\omega_n$ ) is extracted, as follows:

$$x_{st} = \frac{F_{st}L^3}{3EI} \text{ (beam deflection formula) and } F_{st} \equiv kx_{st}$$

$$\therefore k = \frac{F_{st}}{x_{st}} = \frac{3EI}{L^3}$$

Then,

$$m\ddot{x} + \left(\frac{3EI}{L^3}\right)x = 0, \quad \therefore \omega_n = \sqrt{\frac{k}{m}} = \sqrt{\frac{3EI}{mL^3}} \quad (1.12)$$

In this example, the primary approximation is that the *beam is massless*. The secondary approximation is that the *deflections are small* enough so that simple linear beam theory provides a good approximation of beam deflection.

A second important example is illustrated in Figure 1.6b, the simple planar pendulum having a mass ( $m$ ) concentrated at the free end of a rigid link of negligible mass and length ( $L$ ). The appropriate form of Newton's Second Law for motion about the fixed pivot point of this model is  $M = J\ddot{\theta}$ , where  $M$  is the sum of moments about the pivot point "o,"  $J$  (equal to  $mL^2$  here) is the mass moment-of-inertia about the pivot point, and  $\theta$  is the single motion coordinate for this 1-DOF system. The instantaneous sum of moments about the pivot point "o" consists only of that from the gravitational force  $mg$  on the concentrated mass, which is shown as follows (minus sign because  $M$  is always opposite  $\theta$ ):

$$M = -mgL \sin \theta, \quad \therefore mL^2\ddot{\theta} + mgL \sin \theta = 0$$



Dividing by  $mL^2$  gives the following motion equation:

$$\ddot{\theta} + \left(\frac{g}{L}\right) \sin \theta = 0 \quad (1.13)$$

This equation of motion is obviously nonlinear. However, for small motions ( $\theta \ll 1$ )  $\sin \theta \cong \theta$ ; hence it can be linearized as an approximation, as follows:

$$\ddot{\theta} + \left(\frac{g}{L}\right) \theta = 0, \quad \therefore \omega_n = \sqrt{\frac{g}{L}} \quad (1.14)$$

In this last example, the primary approximation is that the *motion is small*. The secondary approximation is that the pendulum has all its *mass concentrated* at its free end. Note that the stiffness or the restoring force effect in this model is not from a spring but from gravity. It is essential to make simplifying approximations in all vibration models, in order to have feasible engineering analyses. It is, however, also essential to understand the practical limitations of those approximations, to avoid producing analysis results that are highly inaccurate or, worse, do not even make physical sense.

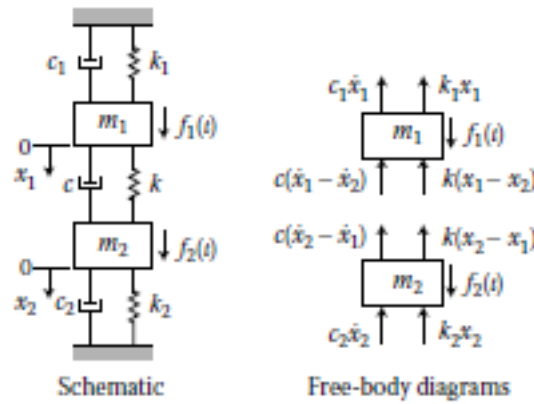


FIGURE 1.7 2-DOF model.

engineering answers over a considerably broader range of problems than the 1-DOF model. Also, first understanding the 2-DOF model is the best approach to tackling the subject of multi-DOF models. Figure 1.7 shows a common 2-DOF model. With the aid of the ever-important *free body diagrams*, application of  $F = ma$  individually to each mass yields the following two equations of motion for this model:

$$\begin{aligned} m_1 \ddot{x}_1 + (c + c_1) \dot{x}_1 + (k + k_1)x_1 - c\dot{x}_2 - kx_2 &= f_1(t) \\ m_2 \ddot{x}_2 + (c + c_2) \dot{x}_2 + (k + k_2)x_2 - c\dot{x}_1 - kx_1 &= f_2(t) \end{aligned} \quad (1.15)$$

With two or more DOFs, it is quite useful to write the equations of motion in matrix form, as follows for Equations 1.15:

$$\begin{aligned} \begin{bmatrix} m_1 & 0 \\ 0 & m_2 \end{bmatrix} \begin{Bmatrix} \ddot{x}_1 \\ \ddot{x}_2 \end{Bmatrix} + \begin{bmatrix} c + c_1 & -c \\ -c & c + c_2 \end{bmatrix} \begin{Bmatrix} \dot{x}_1 \\ \dot{x}_2 \end{Bmatrix} \\ + \begin{bmatrix} k + k_1 & -k \\ -k & k + k_2 \end{bmatrix} \begin{Bmatrix} x_1 \\ x_2 \end{Bmatrix} &= \begin{Bmatrix} f_1(t) \\ f_2(t) \end{Bmatrix} \end{aligned} \quad (1.16)$$

For a multi-DOF system with any number of DOFs, the motion equations are typically written in the following condensed matrix notation:

$$[M]\{\ddot{x}\} + [C]\{\dot{x}\} + [K]\{x\} = \{f(t)\} \quad (1.17)$$

where  $[M]$  is the mass matrix,  $[C]$  is the damping matrix, and  $[K]$  is the stiffness

$$\frac{d}{dt} \left( \frac{\partial T}{\partial \dot{q}_i} \right) - \frac{\partial T}{\partial q_i} + \frac{\partial V}{\partial q_i} = Q_i, \quad i = 1, 2, \dots, n_{\text{DOF}} \quad (1.18)$$

The  $q_i$ 's and  $\dot{q}_i$ 's are the *generalized coordinates* and *velocities*, respectively,  $T$  is the *kinetic energy*,  $V$  is the *potential energy*, and  $Q_i$ 's are the *generalized forces*. Generalized coordinates can be either straight-line displacements (e.g.,  $x, y, z$ ) or angular displacements (e.g.,  $\theta_x, \theta_y, \theta_z$ ). Thus, a generalized force associated with a straight-line displacement will in fact have units of force, whereas a generalized force associated with an angular displacement will have units of moment or torque. Here, kinetic energy can be a function of both *generalized coordinates* and *velocities* whereas potential energy is a function of *generalized coordinates* only, that is,  $T = T(\dot{q}_i, q_i)$  and  $V = V(q_i)$ . Obtaining the two equations of motion for the 2-DOF double-compound pendulum (Figure 1.8) is summarized as follows:

$$T = \frac{1}{2}m_1v_1^2 + \frac{1}{2}m_2v_2^2 \quad (1.19)$$

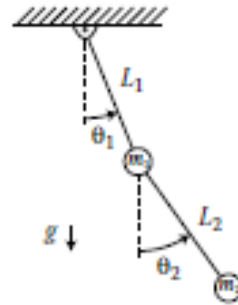


FIGURE 1.8 Planar double-compound pendulum with concentrated masses.

Here,  $v_1$  and  $v_2$  are the speeds of  $m_1$  and  $m_2$ , respectively, and their squares result in the following:

$$\begin{aligned} v_1^2 &= L_1^2 \dot{\theta}_1^2 \\ v_2^2 &= L_1^2 \dot{\theta}_1^2 + L_2^2 \dot{\theta}_2^2 + 2L_1L_2\dot{\theta}_1\dot{\theta}_2(\cos \theta_1 \cos \theta_2 + \sin \theta_1 \sin \theta_2) \\ V &= m_1gL_1(1 - \cos \theta_1) + m_2g[L_1(1 - \cos \theta_1) + L_2(1 - \cos \theta_2)] \end{aligned} \quad (1.20)$$

Here,  $v_1$  and  $v_2$  are the speeds of  $m_1$  and  $m_2$ , respectively, and their squares result in the following:

$$\begin{aligned} v_1^2 &= L_1^2 \dot{\theta}_1^2 \\ v_2^2 &= L_1^2 \dot{\theta}_1^2 + L_2^2 \dot{\theta}_2^2 + 2L_1 L_2 \dot{\theta}_1 \dot{\theta}_2 (\cos \theta_1 \cos \theta_2 + \sin \theta_1 \sin \theta_2) \\ V &= m_1 g L_1 (1 - \cos \theta_1) + m_2 g [L_1 (1 - \cos \theta_1) + L_2 (1 - \cos \theta_2)] \end{aligned} \quad (1.20)$$

Substituting the  $T$  and  $V$  expressions into the Lagrange equations ( $q_1 = \theta_1$  and  $q_2 = \theta_2$ ) leads to the two equations of motion for the double-compound pendulum model shown in Figure 1.8. These two motion equations are nonlinear just as shown in Equation 1.13 for the simple pendulum. Therefore, they can be linearized for *small motions* ( $\theta_1 \ll 1$  and  $\theta_2 \ll 1$ ) in the same manner as Equation 1.14 was obtained from Equation 1.13, to obtain the following:

$$\begin{bmatrix} (m_1 + m_2)L_1^2 & m_2 L_1 L_2 \\ m_2 L_1 L_2 & m_2 L_2^2 \end{bmatrix} \begin{bmatrix} \ddot{\theta}_1 \\ \ddot{\theta}_2 \end{bmatrix} + \begin{bmatrix} (m_1 + m_2)gL_1 & 0 \\ 0 & m_2 g L_2 \end{bmatrix} \begin{bmatrix} \theta_1 \\ \theta_2 \end{bmatrix} = \begin{bmatrix} 0 \\ 0 \end{bmatrix} \quad (1.21)$$

Since Equations 1.21 are written in matrix form, it is clear from the mass matrix and the zeros in the stiffness matrix that this model has acceleration (inertia) coupling but not displacement coupling. Also, the stiffnesses or generalized restoring forces (moments) in this model are not from springs but from gravity, just like the simple pendulum model illustrated in Figure 1.6b. Damping was not included in this model. As in the previous example, the matrices in Equation 1.21 for this example are symmetric, as they must be.

### 1.2.2 Matrix Bandwidth and Zeros

The 4-DOF model in Figure 1.9 has a characteristic common for models of many types of vibratory structures, such as many rotor vibration models, namely, *narrow bandwidth matrices*. Specifically, this system's *mass* matrix is "diagonal" (i.e., only its *diagonal* elements are nonzero) and its *stiffness* matrix is "tri-diagonal" (i.e., only its central three *diagonals* are nonzero), as shown in Figure 1.8. Obviously, a model's matrices are essentially its equations of motion. For this model, the *diagonal* nature of the mass matrix reflects that the model has no inertia coupling, in contrast to the model in Figure 1.8. For rotors, as shown in Chapter 2, the *lumped-mass* approach gives a diagonal mass matrix, in contrast to the so-called *distributed-mass* and *consistent-mass* approaches, which are preferred over the *lumped-mass* approach since they yield better model resolution

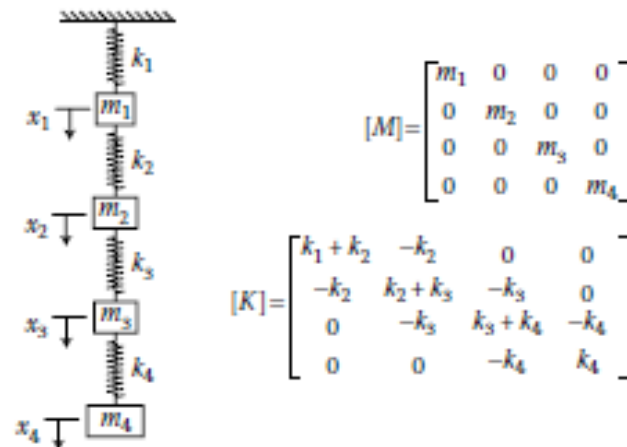


FIGURE 1.9 4-DOF lumped-mass model.

### 1.2.3 Standard Rotor Vibration Analyses

Achieving good models for rotor vibration analyses of many single-span two-bearing rotors may require models with as many as 100 DOFs. For a multispans rotor model of a complete large steam-powered turbo-generator, models of 200 or 300 DOFs are typically deemed necessary to accurately characterize the system. Obtaining the important vibration characteristics of a machine or structure from large DOF models is not nearly as daunting as one might initially think, because of the following axiom: *Rarely is it necessary in engineering vibration analyses to solve the model's governing equations of motion in their totality.* For example, *lateral rotor vibration analyses* generally entail no more than the following three categories:

- i. Natural frequencies (damped or undamped) and corresponding mode shapes.
- ii. Self-excited vibration threshold speeds, frequencies, and mode shapes.
- iii. Vibration over full speed range due to specified rotor mass unbalances.

None of these three categories of analyses actually entails obtaining the general solution for the model's coupled differential equations of motion. That is, the needed computational results can be extracted from the model's equations of motion without having to obtain their general solution, as later detailed.

In the next section, basic topics important to these *standard vibration analyses* are covered. Extraction of *natural frequencies* and *mode shapes* as well

as *instability threshold speeds* are both embedded in the classic *Eigenvalue–Eigenvector* mathematics problem associated with linear vibratory systems. Specifically, the extraction of *natural frequencies* and corresponding *mode shapes* for multi-DOF models are explained. Standard algorithms used for these analyses are treated in later chapters. *Steady-state rotor unbalance vibration* is simply an extension of the 1-DOF Equation 1.6.



### 1.3.1 Modal Decomposition

Each natural mode of an undamped model is exactly equivalent to an undamped 1-DOF model and is mathematically decoupled from the model's other natural modes, as observed when the motion equations

---

are transformed into what are called the *modal coordinates*. Such a coordinate transformation is similar and mathematically equivalent to observing material *stress components* at a point in the *principal coordinate system*, wherein viewed decoupling appears, that is, all the *shear stresses disappear* and the normal stresses are the *principal stresses*. Similarly, when an undamped mutli-DOF model's equations of motion are transformed into their *modal coordinates*, both the *mass* and *stiffness matrices* become *diagonal matrices*, that is, all zeros except for their main diagonal elements. That is, the equations of motion become *decoupled* when they are transformed from the *physical space* into the *modal space*, as explained here.

Equations of motion for free (*unforced*) and undamped multi-DOF models can be compactly expressed in matrix form as follows, where the  $q_i$ 's are the previously defined *generalized coordinates* (Section 1.2.1):

$$[M]\{\ddot{q}\} + [K]\{q\} = \{0\} \quad (1.22)$$

$$[M]\{\ddot{q}\} + [K]\{q\} = \{0\} \quad (1.22)$$

For a specified set of initial conditions,  $\{q(0)\}$  and  $\{\dot{q}(0)\}$ , this set of equations is guaranteed a unique solution by virtue of applicable theorems from differential equation theory, provided both  $[M]$  and  $[K]$  are positive-definite matrices. Therefore, if a solution is found by any means, it must be the solution. Historically, the approach that has guided the successful solution to many problems in mechanics has been the use of good physical insight to provide the correct guess of the solution form. Such is the case for the solution to Equation 1.22.

The vibratory displacement in a multi-DOF model is a function of both time and location in the model. The correct guess here is that the complete solution can be comprised of superimposed contributory solutions, each being expressible as the product of a time function,  $s(t)$ , multiplied by a spatial function of the coordinates,  $\{u\}$ . This is the classic *Separation of Variables* method, expressed as follows:

$$q_i(t) = u_i s(t), \quad i = 1, 2, \dots, N = \text{Number of DOF} \quad (1.23)$$

Substituting Equation 1.23 into Equation 1.22 yields the following equation:

$$[M]\{u\}\ddot{s}(t) + [K]\{u\}s(t) = \{0\} \quad (1.24)$$

Each of these  $N$  equations ( $i = 1, 2, \dots, N$ ) can be expressed as

$$\sum_{j=1}^N M_{ij} u_j \ddot{s}(t) + \sum_{j=1}^N K_{ij} u_j s(t) = 0 \quad (1.25)$$

rearranged to have a function of time only on one side of the equation and a function of location only on the other side of the equation, as follows:

$$-\frac{\ddot{s}(t)}{s(t)} = \frac{\sum_{j=1}^N K_{ij} u_j}{\sum_{j=1}^N M_{ij} u_j} \quad (1.26)$$

Following the usual argument of the separation of variables method, for a time-only function to be equal to a location-only function they both must equal the same constant (say  $\omega^2$ ), positive in this case. A positive constant gives harmonic motions in time, physically consistent with having finite energy in a conservative model and contrary to the exponential solutions that a negative constant gives. The following equations are thereby obtained:

$$\ddot{s}(t) + \omega^2 s(t) = 0 \quad (1.27)$$

$$\sum_{j=1}^N (K_{ij} - \omega^2 M_{ij}) u_j = 0, \quad i = 1, 2, \dots, N \quad (1.28)$$

Equation 1.27 has the same form as the equation of motion for an unforced and undamped 1-DOF model, that is, same as Equation 1.3 with  $c = 0$ . Therefore, the solution of Equation 1.27 can be surmised directly from Equation 1.5, as follows:

$$s(t) = X \begin{Bmatrix} \sin(\omega t + \phi_s^+) \text{ or } \sin(\omega t - \phi_s^-) \\ \cos(\omega t + \phi_c^+) \text{ or } \cos(\omega t - \phi_c^-) \end{Bmatrix} \quad (1.29)$$

Any of the four equation (Equation 1.29) forms can be used to represent the same harmonic signal. The following form is arbitrarily selected here:

$$s(t) = X \cos(\omega t - \phi) \quad (1.30)$$

Equation 1.30 indicates a harmonic motion with all the coordinates having the same frequency and the same phase angle. The information to determine the specific frequencies at which the model will satisfy such a harmonic motion is contained in Equation 1.28, which are a set of  $N$  linear homogeneous algebraic equations in the  $N$  unknowns,  $u_j$ . Determining the values of  $\omega^2$  that provide nontrivial solutions to Equation 1.28 is the classic characteristic value or eigenvalue problem. The trivial solution (all  $u_j$ 's = zero) is a static equilibrium state. Equation 1.28 can be compactly shown in matrix form as follows:

$$[K - \omega^2 M] \{u\} = \{0\} \quad (1.31)$$

From linear algebra it is known that for a nontrivial solution of Equation 1.31, the determinant of equation coefficients must be equal to zero, as follows:

$$D \equiv |K - \omega^2 M| = 0 \quad (1.32)$$

Expanding  $D$ , the characteristic determinant, yields an  $N$ th-order polynomial equation in  $\omega^2$ , usually referred to as the frequency or characteristic equation, which has  $N$  roots (eigenvalues) for  $\omega^2$ . These eigenvalues are real numbers because  $[M]$  and  $[K]$  are symmetric, and are positive because  $[M]$  and  $[K]$  are positive-definite matrices. Virtually any modern text devoted just to vibration theory will contain an expanded treatment on modal decomposition and rigorously develop its quite useful properties, which are summarized here.

The  $N$  roots of Equation 1.32 each provide a positive natural frequency,  $\omega_j$  ( $j = 1, 2, \dots, N$ ), for one of the model's  $N$  natural modes. These undamped natural frequencies are typically ordered by relative magnitude, as follows:

$$\omega_1 \leq \omega_2 \leq \dots \leq \omega_N$$

$[U]$ , is formed using each one of the  $N \times 1$  modal vectors as one of its columns:

$$\{q(t)\} = [U]\{\eta(t)\} \quad (1.33)$$

Here it is convenient to scale each of the modal vectors as follows ("T" denotes *transpose*):

$$\{u_p\}^T [M] \{u_p\} = 1 \quad (1.34)$$

Then the resulting modal matrix,  $[U]$ , will satisfy the following equation:

$$[U]^T [M] [U] = [I] \quad (1.35)$$

Here,  $[I]$  is the identity matrix, with 1 on each main diagonal element and zeros elsewhere. Equation 1.35 is actually a linear transformation of the mass matrix into modal coordinates, with the modal vectors scaled (normalized); hence all the modal masses are equal to 1. Applying the identical transformation on the stiffness matrix also produces a diagonal matrix, with each main diagonal element equal to one of the eigenvalues  $\omega_j^2$  as follows:

$$[U]^T [K] [U] = [\omega_{ij}^2] \quad (1.36)$$

Here, the array  $[\omega_{ij}^2]$  is defined similar to the *kroncker delta*, as follows:

$$\omega_{ij}^2 \equiv \begin{cases} \omega_j^2, & i = j \\ 0, & i \neq j \end{cases} \quad (1.37)$$

Substituting the linear transformation of Equation 1.33 into the original equations of motion Equation 1.22 and then premultiplying the result by  $[U]^T$  yield the following result:

$$[U]^T [M] [U] \{\ddot{\eta}(t)\} + [U]^T [K] [U] \{\eta(t)\} = 0 \quad (1.38)$$

Utilizing in Equations 1.38, 1.35, and 1.36, which express the modal vectors' orthogonality property, shows that the equations of motion are decoupled in the modal coordinate space. Accordingly, Equation 1.38 becomes

$$\{\ddot{\eta}(t)\} + [\omega_{ij}^2] \{\eta(t)\} = 0 \quad (1.39)$$

Equation 1.39 clearly shows that each natural mode is equivalent to an undamped 1-DOF model. Each natural mode's response to a set of initial

conditions is therefore of the same form as for the undamped 1-DOF model, shown as follows:

$$\eta_p(t) = A_p \cos(\omega_p t - \phi_p) \quad (1.40)$$

Consequently, utilizing the linear superposition of the contributions from all the model's natural modes, the motion of a free undamped multi-DOF system is expressible as follows, where the  $A_p$ 's are the single-peak amplitudes of each of the modes:

$$\{q(t)\} = \sum_{p=1}^N A_p \{u_p\} \cos(\omega_p t - \phi_p)$$

This can be expressed in matrix form as follows:

$$\{q(t)\} = [U]\{A_p \cos(\omega_p t - \phi_p)\} \quad (1.41)$$

### 1.3.2 Modal Damping

A major role of damping is to dissipate vibration energy that would otherwise lead to intolerably high vibration amplitudes at forced resonances or allow self-excited vibration phenomena to occur. As already shown for the 1-DOF model, a natural frequency is only slightly lowered by the damping, but the peak vibration caused by an excitation force at the natural frequency is overwhelmingly lowered by the damping. This clearly applies to multi-DOF models, as shown by the modal damping approach which follows.



can be incorporated into the model by adding it to each relevant mode in the modal coordinate system. Accordingly, Equation 1.39 is augmented as follows:

$$\{\ddot{\eta}(t)\} + 2[\zeta_i \omega_j]\{\dot{\eta}(t)\} + [\omega_{ij}^2]\{\eta(t)\} = 0 \quad (1.42)$$

Here,  $\zeta_i \omega_j$  is a diagonal array defined similar to the Kronecker delta, as follows:

$$\zeta_i \omega_j \equiv \begin{cases} \zeta_j \omega_j, & i = j \\ 0, & i \neq j \end{cases} \quad (1.43)$$

The often used 1-DOF version of Equation 1.42 is obtained by dividing Equation 1.3 by  $m$  and using the definition for  $\zeta$  given in Equation 1.10, yielding  $\ddot{x} + 2\zeta\omega_n\dot{x} + \omega_n^2x = 0$ .

Mathematically, an  $N$ -DOF model has  $N$  modes. However, the discrete model (e.g., finite-element model) should have the DOF number,  $N$ , several (like 10, "more or less") times the mode number,  $n$ , of the actual system's highest frequency mode of importance. This statement assumes usual mode numbering by ascending frequency,  $\omega_1 \leq \omega_2 \leq \dots \leq \omega_n \leq \dots \leq \omega_N$ . The underlying objective is for the discrete model to adequately characterize the actual continuous media system in the frequency range up to the maximum modal frequency of importance. *It is of fundamental modeling importance that at frequencies progressively higher the characteristics of the discrete model and those of the actual system progressively diverge.* The desired number of important modes will depend on the nature of the problem analysis. For example, to analyze forced resonances, one hopefully knows the actual maximum excitation-force frequency  $\omega_{\max}$ . As a rule, all modal frequencies within and somewhat above the excitation frequency range should be included even though some of these modes may be of lesser importance than others.

Consider an application in which an actual system has been tested, providing damping ratio data for the lowest frequency  $n$  modes. The first  $n$  elements ( $j = 1, 2, \dots, n < N$ ) of the  $N \times N$  diagonal modal damping matrix will each contain its own value,  $\zeta_j \omega_j$ . The modal damping matrix will otherwise consist of zeros, and thus modified from Equation 1.43 as follows:

$$\zeta_i \omega_j = \begin{cases} \zeta_j \omega_j, & i = j \leq n \\ 0, & i = j > n \\ 0, & i \neq j \end{cases} \quad (1.44)$$

1-DOF model and relevant modes of a multi-DOF model is thus shown, as follows:

$$\ddot{\eta}_j + 2\zeta_j\omega_j\dot{\eta}_j + \omega_j^2\eta_j = 0 \quad (1.45)$$

The equations of motion in the physical coordinates are then as follows:

$$[M]\{\ddot{q}\} + [C_m]\{\dot{q}\} + [K]\{q\} = \{0\} \quad (1.46)$$

The elements  $2\zeta_j\omega_j$  form a diagonal matrix in modal coordinates to incorporate the mode-by-mode damping model. Consequently, the transformation to physical coordinates to obtain  $[C_m]$  would appear to be simply the inverse of the transformation that diagonalizes  $[M]$  and  $[K]$ , as shown in the following equation:

$$[C_m] = [U^T]^{-1}[2\zeta_j\omega_j][U]^{-1} \quad (1.47)$$

### 1.3.3 Forced Systems Decoupled in Modal Coordinates

This important topic is shown by adding a system of external time-dependent forces to either the *modally damped* model of Equation 1.46 or the *undamped* model of Equation 1.22,  $[C] = [0]$ , both of which are contained within the following equation:

$$[M]\{\ddot{q}\} + [C_m]\{\dot{q}\} + [K]\{q\} = \{f(t)\} \quad (1.48)$$

Since the modal vectors span the vector space of all possible model displacement states, modal decomposition is applicable to forced systems as well. Clearly, transformation of Equation 1.48 into the modal coordinate system provides the following equivalent decoupled set of equations:

$$\{\ddot{\eta}(t)\} + 2[\zeta_i\omega_j]\{\dot{\eta}(t)\} + [\omega_{ij}^2]\{\eta(t)\} = [U]^T\{f(t)\} \quad (1.49)$$

Here, the vector of modal forces is  $\{\Phi(t)\} \equiv [U]^T\{f(t)\}$ . This shows that each modal force  $\Phi_i(t)$  is a linear combination of all the physical forces  $f_j(t)$ . And the contribution of each physical force to  $\Phi_i(t)$  is in proportion to the modal matrix element  $U_{ji}$  (or  $U_{ij}^T$ ), which is called the *participation factor* of the  $j$ th physical coordinate for the  $i$ th mode.

As an important example, Equation 1.49 shows that a physical harmonic force having a particular mode's natural frequency will produce its maximum resonance vibration effect if applied at the physical coordinate location having that mode's largest participation factor. Conversely, if the same harmonic force is applied in a physical coordinate with a zero-participation factor (called a "nodal point" for that mode), the force's contribution to that mode's vibration will be zero. This is particularly relevant to *rotor balancing problems*, explaining why both a rotor unbalance magnitude and its axial location are important.

### 1.3.4 Harmonic Excitation of Linear Multi-DOF Models

The most frequently performed type of vibration analysis is the *steady-state* response from *harmonic* excitation forces. Various single-frequency solutions at different frequencies can be superimposed to obtain a simultaneous multifrequency steady-state solution, provided the model is linear. Also, using the single-frequency case, the frequency can be varied over the desired range in a given application. Thus, the formulation and solution for the single-frequency case is the building block for vibration analyses. The generic governing equation for this case can be expressed as follows, where  $[C]$  is arbitrary and not necessarily modal:

$$[M]\{\ddot{x}\} + [C]\{\dot{x}\} + [K]\{x\} = \{F_j e^{i(\omega t + \theta_j)}\} \quad (1.50)$$

Here,  $x$  is used as the generalized coordinate symbol, and the harmonic forcing functions have individual magnitudes  $F_j$  and phase angles  $\theta_j$ . Since they have a common excitation frequency  $\omega$ , it is convenient to represent each harmonic excitation force as a planar vector rotating counter clockwise (ccw) at  $\omega$  (rad/s) in the complex-plane exponential form. The right-hand side of Equation 1.50 represents the standard notation for this representation,  $i \equiv \sqrt{-1}$ . The instantaneous projection of each planar vector onto the *real axis* of the complex plane is the instantaneous physical value of the corresponding sinusoidal time-varying scalar force component.

Equation 1.50 is the multi-DOF version of the 1-DOF model representation in Equation 1.6 whose *steady-state* solution (the so-called *particular* solution) is harmonic, Equation 1.7. For the multi-DOF Equation 1.50, the steady-state solution is also harmonic, and shown as follows using the exponential complex form:

$$x_j = X_j e^{i(\omega t + \phi_j)} \quad (1.51)$$

Here,  $X_j$  is the single-peak amplitude of the  $j$ th coordinate's harmonic motion at frequency  $\omega$  and phase angle  $\phi_j$ . Substitution of this known solution form, Equation 1.51, into the equations of motion, Equation 1.50, and then dividing through by  $e^{i\omega t}$ , yields the following simultaneous set of complex algebraic equations:

$$[-\omega^2 M + i\omega C + K][X_j e^{i\phi_j}] = \{F_j e^{i\theta_j}\} \quad (1.52)$$

In this set of equations, the known inputs are the model's  $M$ ,  $C$ , and  $K$  matrices, the excitation forcing frequency  $\omega$  and magnitude  $F_j$ , and the phase angle  $\theta_j$  for each of the excitation forces. The outputs are the single-peak amplitude  $X_j$  and the phase angle  $\phi_j$  for each  $j$ th physical motion coordinate of the model.

### 1.3.5 Dynamic Instability: The Complex Eigenvalue Problem

Consider the unforced general multi-DOF linear model, expressed as follows:

$$[M][\ddot{x}] + [C][\dot{x}] + [K][x] = \{0\} \quad (1.53)$$

**TABLE 1.1**

Eigenvalue Categories and Associated Types of Unforced Motion

Eigenvalue Category	Mode Motion: $\eta(t) = Ae^{\alpha t} \cos(\omega t - \phi)$
1. $\alpha = 0, \omega \neq 0$	Zero damped, steady-state sinusoidal motion
2. $\alpha < 0, \omega \neq 0$	Underdamped, sinusoidal, exponential decay
3. $\alpha > 0, \omega \neq 0$	Negatively damped, sinusoidal, exponential growth
4. $\alpha = 0, \omega = 0$	So-called rigid-body mode, constant momentum
5. $\alpha < 0, \omega = 0$	Overdamped, nonoscillatory, exponential decay
6. $\alpha > 0, \omega = 0$	(i) Negatively damped more than "critical" amount (ii) Statically unstable nonoscillatory exponential growth

restrictions are made here on  $[K]$ ,  $[C]$ , or  $[M]$ . Solutions of Equation 1.53 have the following form:

$$\{x\} = \{X\}e^{\lambda t}, \quad \text{where } \lambda = \alpha \pm i\omega \quad (1.54)$$

(positively damped) to Category 3 (negatively damped). Exactly on such a transition boundary, the mode in question is in Category 1 (zero damped).

Equation 1.53 is a set of  $N$  second-order ODEs. The usual approach to formulate the associated eigenvalue problem entails first transforming Equation 1.53 into an equivalent set of  $2N$  first-order differential equations. To that end, the following associated vectors are defined,

$$\{y\} \equiv \{\dot{x}\}, \quad \therefore \{\dot{y}\} = \{\ddot{x}\} \quad \text{and} \quad \{z\} \equiv \begin{Bmatrix} \{y\} \\ \{x\} \end{Bmatrix}, \quad \therefore \{\dot{z}\} \equiv \begin{Bmatrix} \{\dot{y}\} \\ \{\dot{x}\} \end{Bmatrix}$$

so that Equation 1.53 is transformed into the following:

$$\begin{bmatrix} [0] & [M] \\ [M] & [C] \end{bmatrix} \{\dot{z}\} + \begin{bmatrix} [-M] & [0] \\ [0] & [K] \end{bmatrix} \{z\} = \{0\} \quad (1.55)$$

Naturally, Equation 1.53 and Equation 1.55 have solutions of the same form, Equation 1.54 as follows:

$$\{z\} = \{Z\}e^{\lambda t}, \quad \text{where } \lambda = \alpha \pm i\omega \quad (1.56)$$

A  $2N \times 2N$  matrix  $[A]$  is defined as

$$[A] \equiv \begin{bmatrix} [0] & [M] \\ [M] & [C] \end{bmatrix}^{-1} \begin{bmatrix} [-M] & [0] \\ [0] & [K] \end{bmatrix} \quad (1.57)$$

Compact Equation 1.55 is shown as follows:

$$\{\dot{z}\} + [A]\{z\} = \{0\} \quad (1.58)$$

Substituting Equation 1.56 into Equation 1.58 and dividing the result by  $e^{\lambda t}$  yields the following *complex eigenvalue problem*:

$$[A + I\lambda]\{Z\} = \{0\} \quad (1.59)$$



---

# *Lateral Rotor Vibration Analysis Models*

---

## **2.1 Introduction**

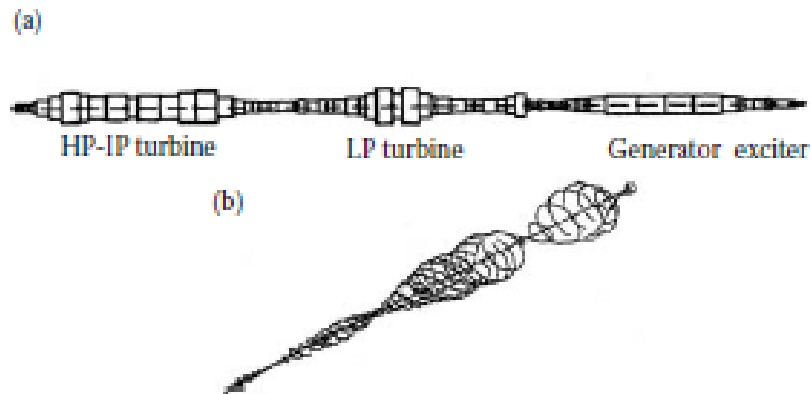
*Lateral rotor vibration* (LRV) is radial-plane orbital motion of the rotor spin axis. *Transverse rotor vibration* is used synonymously with LRV. Figure 2.1 shows the sketch of a complete steam turbine generator rotor (minus turbine blades) and a sample of its computed LRV vibration orbits, shown grossly enlarged. Actual LRV orbits are typically only a few thousandths of an inch (a few hundredths of a millimeter) across. LRV is an important design consideration in many types of rotating machinery, particularly turbo-electrical machines such as steam and combustion gas turbine generators sets, compressors, pumps, gas turbine jet engines, turbochargers, and electric motors. Thus, LRV impacts several major industries.

Usually, but not always, the potential for rotor dynamic beam-bending-type deflections significantly contributes to the LRV characteristics. The significance of LRV rotor bending increases with bearing-to-rotor stiffness ratio and with rotor spin speed. Consequently, in some rotating machines with low operating speed and/or low bearing-to-rotor stiffness ratio, the LRV is essentially of a rigid rotor vibrating in flexible bearings/supports. The opposite case (i.e., a flexible rotor in essentially rigid bearings) is also possible but rotor dynamically less desirable, because it lacks some vibratory motion at the bearings which often provide that essential ingredient, *damping*, to keep vibration amplitudes at resonance conditions within tolerable levels.

For the same reason, it is generally undesirable to have journal bearings located at *nodal points* of important potentially resonant modes, that is, the squeeze-film damping capacity of a bearing cannot dissipate vibration energy without some vibratory motion across it. Figure 2.1 is a case with significant participation of both rotor bending and relative motion at the bearings. This is the most interesting and challenging LRV category to analyze.

A rotor's flexibility and mass distributions and its bearings' flexibilities combined with its maximum spin speed essentially determine whether or not residual rotor unbalance can produce forced LRV resonance. That is, these aforementioned factors determine if the rotor-bearing system has one or more *lateral natural frequency* modes below the operating speed.





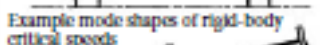

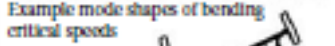


**FIGURE 2.1** LRV example; vibration orbits show rotor dynamic flexibility: (a) steam turbo-generator rotor sketch (minus turbine blades) and (b) sample vibration orbits of above turbo-generator (isometric view).

If so, then the rotor must pass through the speed(s) (called “critical speeds”) where the residual mass unbalances act as once-per-rev (synchronous) harmonic forces to excite the one or more natural frequencies the rotor speed traverses when accelerating to operating speed and when coasting down. Resonant mode shapes at critical speeds are also determined by the same aforementioned rotor and bearing properties. Many types of modern rotating machinery are designed to operate above one or more (sometimes several) *critical speeds*, because of demands for compact high-performance machines.

TABLE 2.1

## Three Elementary LRV Complexity Categories

No	System category	Design considerations
1	Max. speed below 80% of lowest critical speed 	Two-plane low-speed rigid-body balancing is all that is required. No elaborate analyses required.
2	Max. speed is near lowest critical speed or above one or two critical speeds, but bearings are sufficiently soft that critical-speed modes are rigid-body-like.  Example mode shapes of rigid-body critical speeds 	Must calculate critical speed(s) to avoid continuous operation at or near a critical speed. Recommend analysis prediction of vibration amplitudes at critical speeds versus amount of available damping. Should also check for self-excited instability rotor vibration. Two-plane low-speed rigid-body balancing is adequate because rotor dynamic flexibility is not significant.
3	Max. speed near or above one or two more critical speeds and rotor flexing is a significant part of critical-speed mode shapes.  Example mode shapes of bending critical speeds 	Some recommendations as category 2, except that it will probably be necessary to perform multiplane flexible-rotor balancing at speeds up to maximum operating speed because of the importance of bending critical speeds (see Sec. 11, Chapter 12.)

dynamic coupling to exist between *LRV* and *TRV* characteristics. Consequently, these two types of rotor vibration, while potentially coexisting to significant degrees in the same rotor, practically do not significantly interact. There are a few exceptions to this, for example, high-speed refrigerant centrifugal compressors for high-capacity refrigeration and air conditioning systems. Such compressor units are typically comprised of two parallel *rotor dynamically flexible* shafts coupled by a two-gear single-stage speed increaser. In that specific type of rotating machinery, the gear teeth forces provide a potential mechanism for coupling the *LRV* and *TRV* characteristics. Even in that exceptional application, such *lateral-torsional coupling* is generally not factored into design analyses. Near the end of Chapter 3, subsequent to the coverage of applicable first principles for both *LRV* and *TRV*, Table 3.1 is presented to show some quite interesting and important contrasts between *LRV* and *TRV*, which are not frequently articulated and thus not widely appreciated.

## 2.2 Simple Linear Models

### 2.2.1 Point–Mass 2-DOF Model

The simplest LRV model that can encompass radial-plane orbital rotor motion has 2-DOF, as shown in Figure 2.2. In this model, the rotor point

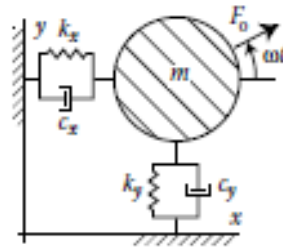


FIGURE 2.2 Simplest LRV model that can handle radial-plane orbital motion.

mass ( $m$ ) is allowed to translate in a radial  $x$ – $y$  plane. It is connected to ground through linear springs and dampers and may be excited by time-varying radial force components such as the rotating force (mass-unbalance) shown. The two equations of motion for this model with the shown rotating excitation force are easily derived from  $F = ma$  to obtain the following:

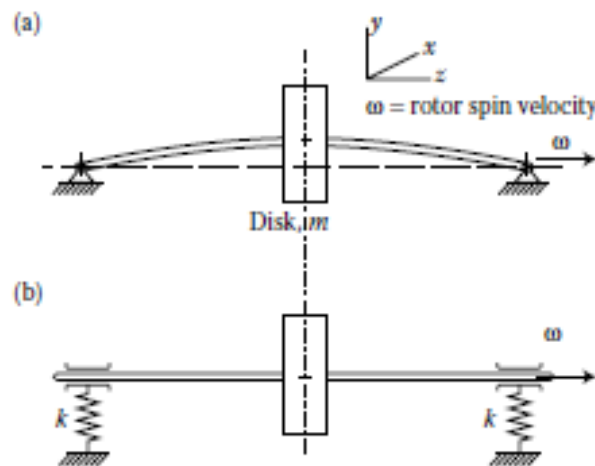
$$\begin{aligned} m\ddot{x} + c_x\dot{x} + k_x x &= F_o \cos \omega t \\ m\ddot{y} + c_y\dot{y} + k_y y &= F_o \sin \omega t \end{aligned} \tag{2.1}$$

$$\begin{bmatrix} m & 0 \\ 0 & m \end{bmatrix} \begin{Bmatrix} \ddot{x} \\ \ddot{y} \end{Bmatrix} + \begin{bmatrix} c_{xx} & c_{xy} \\ c_{yx} & c_{yy} \end{bmatrix} \begin{Bmatrix} \dot{x} \\ \dot{y} \end{Bmatrix} + \begin{bmatrix} k_{xx} & k_{xy} \\ k_{yx} & k_{yy} \end{bmatrix} \begin{Bmatrix} x \\ y \end{Bmatrix} = \begin{Bmatrix} F_x(t) \\ F_y(t) \end{Bmatrix} \quad (2.2)$$

As shown in considerably more detail later in this chapter and in Chapter 5, such  $2 \times 2$   $[c_{ij}]$  and  $[k_{ij}]$  matrices for bearings and seals are extremely important inputs for many LRV analyses, and have been the focus of extensive research to improve the accuracy for quantifying their matrix coefficients. In general, these coefficient matrices for bearings and seals cannot be simultaneously diagonalized in a single  $x$ - $y$  coordinate system, in contrast to the model shown in Figure 2.2. In fact, as explained later in this chapter, the bearing and seal stiffness coefficient matrices are often nonsymmetric and their damping coefficient matrices may also be nonsymmetric when certain fluid dynamical factors are significant (e.g., fluid inertia).

### 2.2.2 Jeffcott Rotor Model

A centrally mounted disk on a slender flexible uniform shaft comprises the model employed by H. H. Jeffcott [*Philosophical Magazine* 6(37), 1919] to analyze the lateral vibration of shafts in the neighborhood of the (lowest) critical speed. Figure 2.3a is a lateral planar view of this model and Figure 2.3b is its extension to include bearing flexibility. If the concentrated midspan disk mass  $m$  in these two models is treated strictly as a point mass, then both of these models fit the 2-DOF model in Figure 2.2. If bearing stiffness is included but bearing damping neglected, bearing



**FIGURE 2.3** Jeffcott rotor model: (a) Jeffcott model and (b) modified Jeffcott model with bearing flexibility.

$$\begin{aligned}
& \begin{bmatrix} m & 0 & 0 & 0 \\ 0 & m & 0 & 0 \\ 0 & 0 & I_T & 0 \\ 0 & 0 & 0 & I_T \end{bmatrix} \begin{Bmatrix} \ddot{x} \\ \ddot{y} \\ \ddot{\theta}_x \\ \ddot{\theta}_y \end{Bmatrix} + \begin{bmatrix} 0 & 0 & 0 & 0 \\ 0 & 0 & 0 & 0 \\ 0 & 0 & 0 & \omega I_P \\ 0 & 0 & -\omega I_P & 0 \end{bmatrix} \begin{Bmatrix} \dot{x} \\ \dot{y} \\ \dot{\theta}_x \\ \dot{\theta}_y \end{Bmatrix} \\
& + \begin{bmatrix} k_x & 0 & 0 & 0 \\ 0 & k_y & 0 & 0 \\ 0 & 0 & K_x & 0 \\ 0 & 0 & 0 & K_y \end{bmatrix} \begin{Bmatrix} x \\ y \\ \theta_x \\ \theta_y \end{Bmatrix} = \begin{Bmatrix} F_x(t) \\ F_y(t) \\ M_x(t) \\ M_y(t) \end{Bmatrix} \tag{2.3}
\end{aligned}$$

### 2.2.3 Simple Nontrivial 8-DOF Model

Even if one understands the underlying physical principles imbedded in a computationally intensive engineering analysis computer code, it is still somewhat of a “black box” to all except the individual(s) who wrote the code. In that vein, the equations of motion for a multi-DOF system are essentially contained in the elements of the model’s  $[M]$ ,  $[C]$ , and  $[K]$  matrices, which are “constructed and housed inside the computer” during computation. Therefore, prior to presenting the formulation and development of the Rotor Dynamic Analysis (RDA) Finite Element PC software supplied with this book, the complete equations of motion are here rigorously developed for a simple nontrivial 8-DOF LRV model using both the Lagrange and direct  $F = ma$  approaches. This 8-DOF model is illustrated in Figure 2.4, and contains the following features of general purpose multi-DOF LRV models:

- a. Bending of the shaft in two mutually perpendicular lateral planes.
- b. Two completely general dynamically linear bearings.

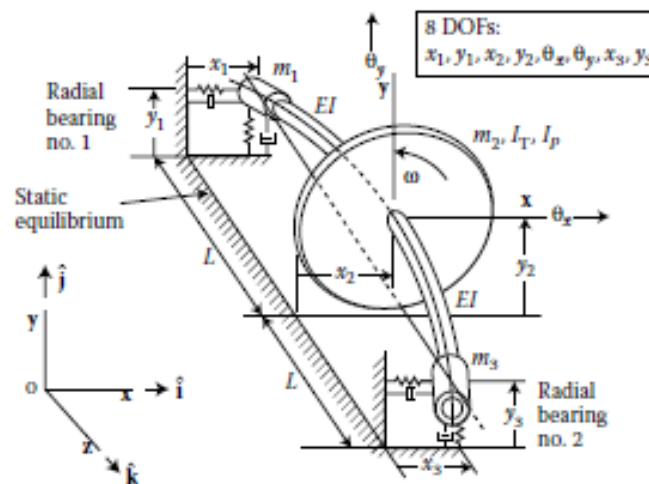


FIGURE 2.4 Simple nontrivial 8-DOF model for LRV.

- c. Three concentrated masses connected by flexible shafting.
- d. The central concentrated mass also has transverse and polar moments of inertia and associated angular coordinates.



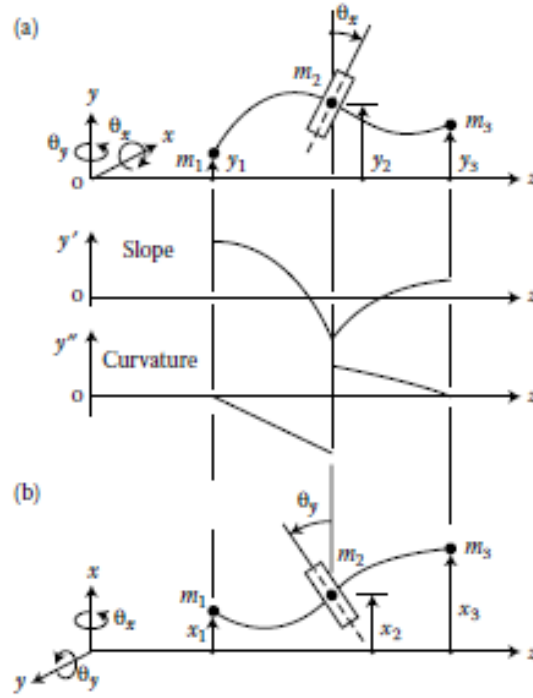


FIGURE 2.5 Rotor beam-deflection model for an 8-DOF system, with all generalized coordinates shown in their respective positive directions: (a) beam deflection, slope, and curvature in  $y$ - $z$  plane and (b)  $x$ - $z$  deflection only, but slope and curvature similar to (a).

### 2.2.3.1 Lagrange Approach (i)

Referring back in Section 1.2.1 to the description of the Lagrange equations, they can be expressed as follows:

$$\frac{d}{dt} \left( \frac{\partial T}{\partial \dot{q}_i} \right) - \frac{\partial T}{\partial q_i} + \frac{\partial V}{\partial q_i} = Q_i, \quad i = 1, 2, \dots, n_{\text{DOF}} \quad (2.4)$$

where  $T$  and  $V$  are the kinetic and potential energy functions, respectively; and  $q_i$  and  $Q_i$  are the generalized coordinates and generalized forces, respectively. In this derivation, the left-hand side of Equations 2.4 is used to develop the rotor model mass and stiffness matrices. The bearings' stiffness and damping components as well as the rotor disk's gyroscopic moment are treated as generalized forces and thus brought into the equations of motion on the right-hand side of Equations 2.4.

For a beam in bending, the potential energy can be derived by integrating the strain energy over the length of the beam. Linear beam theory is used here, so the bending strain energy in two planes ( $x$ - $z$  and  $y$ - $z$ ) can be linearly superimposed as

$$V = \int_0^{2L} \frac{M_{xz}^2 + M_{yz}^2}{2EI} dz \quad (2.5)$$

shaft is treated.

$z = 0 \text{ to } L$	Boundary conditions
$x = az^3 + bz + c$	$x(0) = x_1 = c$
$x' = 3az^2 + b$	$x(L) = x_2 = aL^3 + bL + x_1$
$x'' = 6az$	$x'(L) = \theta_y = 3aL^2 + b$
$\theta_x, \theta_y \ll 1,$	$\therefore \tan \theta_x \cong \theta_x \text{ and } \tan \theta_y \cong \theta_y$

From the above simultaneous equations with boundary conditions utilized at  $z = 0$  and  $z = L$ , the coefficient " $a$ " is determined and results in the following expression for  $x$ - $z$  plane curvature:

$$x'' = \frac{3}{L^3}(x_1 - x_2 + \theta_y L)z, \quad z = 0 \text{ to } L \quad (2.6)$$

Similarly, the  $y$ - $z$  plane curvature over  $z = 0$  to  $L$  is determined to be the following:

$$y'' = \frac{3}{L^3}(y_1 - y_2 - \theta_x L)z, \quad z = 0 \text{ to } L \quad (2.7)$$

For the right half shaft, the same polynomial form is used for beam deflection as for the left half shaft, except that  $(2L-z)$  must be put in place of  $z$ , as follows:

$z = L \text{ to } 2L$	Boundary conditions
$x = a(2L - z)^3 + b(2L - z) + c$	$x(2L) = x_3 = c$
$x' = -3a(2L - z)^2 - b$	$x(L) = x_2 = aL^3 + bL + x_3$
$x'' = 6a(2L - z)$	$x'(L) = \theta_y = -3aL^2 - b$

From these simultaneous equations with boundary conditions utilized (at  $z = L$  and  $z = 2L$ ), the coefficient " $a$ " is determined and results in the following expression for  $x$ - $z$  plane curvature:

$$x'' = \frac{3}{L^3}(x_3 - x_2 - \theta_y L)(2L - z), \quad z = L \text{ to } 2L \quad (2.8)$$

(i.e.,  $M_{xz} = Elx''$  and  $M_{yz} = Ely''$  from linear beam theory). Because of the curvature discontinuity at  $z = L$ , the integral for strain energy must be split into two pieces, as follows:

$$V = \frac{EI}{2} \left[ \int_0^L [(x'')^2 + (y'')^2] dz + \int_L^{2L} [(x'')^2 + (y'')^2] dz \right] \quad (2.10)$$

There are obvious math steps left out at this point, in the interest of space. The obtained expression for potential energy is given as follows:

$$V = \frac{3EI}{2L^3} \left( x_1^2 + 2x_2^2 + x_3^2 - 2x_1x_2 - 2x_2x_3 + 2x_1\theta_yL - 2x_3\theta_yL + 2\theta_y^2L^2 \right. \\ \left. + y_1^2 + 2y_2^2 + y_3^2 - 2y_1y_2 - 2y_2y_3 - 2y_1\theta_xL + 2y_3\theta_xL + 2\theta_x^2L^2 \right) \quad (2.11)$$

In this approach, the gyroscopic effect is treated as an external moment upon the disk, so expressing the kinetic energy is a relatively simple step since the disk's spin velocity is not included in  $T$ . Kinetic energies for  $m_1$  and  $m_3$  are just  $\frac{1}{2}m_1v_1^2$  and  $\frac{1}{2}m_3v_3^2$ , respectively. For the disk ( $m_2$ ), kinetic energy ( $T_{\text{disk}}$ ) can be expressed as the sum of its mass center's translational kinetic energy ( $T_{\text{cg}}$ ) and its rotational kinetic energy ( $T_{\text{rot}}$ ) about the mass center. The kinetic energy function is thus given as follows:

$$T = \frac{1}{2} \left[ m_1(\dot{x}_1^2 + \dot{y}_1^2) + m_2(\dot{x}_2^2 + \dot{y}_2^2) + I_T(\dot{\theta}_x^2 + \dot{\theta}_y^2) + m_3(\dot{x}_3^2 + \dot{y}_3^2) \right] \quad (2.12)$$

$$I_T = \frac{1}{4}m_2R^2 \quad \text{and} \quad I_P = \frac{1}{2}m_2R^2$$

The generalized forces for the bearings are perturbations from static equilibrium, and are treated as linear displacement and velocity-dependent forces, expressible for each bearing as follows:

$$f_x^{(n)} = -k_{xx}^{(n)}x - k_{xy}^{(n)}y - c_{xx}^{(n)}\dot{x} - c_{xy}^{(n)}\dot{y} \\ f_y^{(n)} = -k_{yx}^{(n)}x - k_{yy}^{(n)}y - c_{yx}^{(n)}\dot{x} - c_{yy}^{(n)}\dot{y} \quad (2.13)$$

where,  $n$  is the bearing no. = 1, 2.

Treating the gyroscopic effect in this approach simply employs the following embodiment of Newton's Second Law for rotation of a rigid body:

$$\dot{\vec{H}} = \vec{M} \quad (2.14)$$

( $\vec{M}$ ) upon the rigid body, both ( $\vec{H}$ ) and ( $\vec{M}$ ) being referenced to the same base point (the disk's center-of-gravity is used). Here,  $\vec{H} = \hat{i}I_T\dot{\theta}_x + \hat{j}I_T\dot{\theta}_y + \hat{k}I_P\omega$  is the angular momentum, with the spin velocity ( $\omega$ ) held constant. To make the mass moment-of-inertia components time invariant, the ( $x, y, z$ ) unit base vectors ( $\hat{i}, \hat{j}, \hat{k}$ ) are defined to precess with the disk's axis of symmetry (i.e., spin axis) at an angular velocity  $\vec{\Omega} = \hat{i}\dot{\theta}_x + \hat{j}\dot{\theta}_y$ . Since the ( $\hat{i}, \hat{j}, \hat{k}$ ) triad rotates at the precession velocity ( $\vec{\Omega}$ ), the total inertial time-rate-of-change of the rigid body's angular momentum ( $\dot{\vec{H}}$ ) is expressed as follows:

$$\dot{\vec{H}} = \dot{\vec{H}}_{\Omega} + \vec{\Omega} \times \vec{H} \quad (2.15)$$

Using the chain rule for differentiating a product,  $\dot{\vec{H}}_{\Omega} = \hat{i}I_T\ddot{\theta}_x + \hat{j}I_T\ddot{\theta}_y$  is the portion of  $\dot{\vec{H}}$  obtained by differentiating  $\dot{\theta}_x$  and  $\dot{\theta}_y$ , and  $\vec{\Omega} \times \vec{H}$  is the portion obtained by differentiating the rotating base vectors ( $\hat{i}, \hat{j}, \hat{k}$ ). The disk's angular motion displacements ( $\theta_x, \theta_y \ll 1$ ) are assumed to be very small; therefore, the precessing triad ( $\hat{i}, \hat{j}, \hat{k}$ ) has virtually the same orientation as the nonrotating  $x$ - $y$ - $z$  coordinate system. Thus, a vector referenced to the precessing ( $\hat{i}, \hat{j}, \hat{k}$ ) system has virtually the same  $x$ - $y$ - $z$  scalar components in the nonprecessing ( $\hat{i}, \hat{j}, \hat{k}$ ) system. Equation 2.14 then yields the following expressions for the  $x$  and  $y$  moment components that must be applied to the disk to make it undergo its  $x$  and  $y$  angular motions.

$$\begin{array}{ll} M_x = I_T\ddot{\theta}_x + I_P\omega\dot{\theta}_y & \text{rearranged to} \quad M_x - I_P\omega\dot{\theta}_y = I_T\ddot{\theta}_x \\ M_y = I_T\ddot{\theta}_y - I_P\omega\dot{\theta}_x & M_y + I_P\omega\dot{\theta}_x = I_T\ddot{\theta}_y \end{array} \quad (2.16)$$

The  $I_T$  acceleration terms in Equations 2.16 are included via the Lagrange kinetic energy function ( $T$ ), Equation 2.12. However, the  $I_P$  terms are not included, and these are the gyroscopic inertia components that are rearranged here to the left side of the equations, as shown, to appear as moment components (fictitious) applied to the disk. The gyroscopic moment components that are "applied" to the disk as generalized forces in Equations 2.4 are then as follows:

of motion for the model shown in Figure 2.4 are presented in the matrix form, as follows:

$$\begin{aligned}
 & \begin{Bmatrix} m_1 \ddot{x}_1 \\ m_1 \ddot{y}_1 \\ m_2 \ddot{x}_2 \\ m_2 \ddot{y}_2 \\ I_T \ddot{\theta}_x \\ I_T \ddot{\theta}_y \\ m_3 \ddot{x}_3 \\ m_3 \ddot{y}_3 \end{Bmatrix} + \begin{Bmatrix} c_{xx}^{(1)} & c_{xy}^{(1)} & 0 & 0 & 0 & 0 & 0 & 0 \\ c_{yx}^{(1)} & c_{yy}^{(1)} & 0 & 0 & 0 & 0 & 0 & 0 \\ 0 & 0 & 0 & 0 & 0 & 0 & 0 & 0 \\ 0 & 0 & 0 & 0 & 0 & 0 & 0 & 0 \\ 0 & 0 & 0 & 0 & I_P \omega & 0 & 0 & 0 \\ 0 & 0 & 0 & 0 & -I_P \omega & 0 & 0 & 0 \\ 0 & 0 & 0 & 0 & 0 & 0 & c_{xx}^{(2)} & c_{xy}^{(2)} \\ 0 & 0 & 0 & 0 & 0 & 0 & c_{yx}^{(2)} & c_{yy}^{(2)} \end{Bmatrix} \begin{Bmatrix} \dot{x}_1 \\ \dot{y}_1 \\ \dot{x}_2 \\ \dot{y}_2 \\ \dot{\theta}_x \\ \dot{\theta}_y \\ \dot{x}_3 \\ \dot{y}_3 \end{Bmatrix} \\
 & + \frac{3EI}{L^3} \begin{Bmatrix} (1 + \bar{k}_{xx}^{(1)}) & \bar{k}_{xy}^{(1)} & -1 & 0 & 0 & L & 0 & 0 \\ \bar{k}_{yx}^{(1)} & (1 + \bar{k}_{yy}^{(1)}) & 0 & -1 & -L & 0 & 0 & 0 \\ -1 & 0 & 2 & 0 & 0 & 0 & -1 & 0 \\ 0 & -1 & 0 & 2 & 0 & 0 & 0 & -1 \\ 0 & -L & 0 & 0 & 2L^2 & 0 & 0 & L \\ L & 0 & 0 & 0 & 0 & 2L^2 & -L & 0 \\ 0 & 0 & -1 & 0 & 0 & -L & (1 + \bar{k}_{xx}^{(2)}) & \bar{k}_{xy}^{(2)} \\ 0 & 0 & 0 & -1 & L & 0 & \bar{k}_{yx}^{(2)} & (1 + \bar{k}_{yy}^{(2)}) \end{Bmatrix} \\
 & \times \begin{Bmatrix} x_1 \\ y_1 \\ x_2 \\ y_2 \\ \theta_x \\ \theta_y \\ x_3 \\ y_3 \end{Bmatrix} = \{R\} \tag{2.18} \\
 & \bar{k}_{ij}^{(n)} \equiv \frac{L^3}{3EI} k_{ij}^{(n)}
 \end{aligned}$$

$\{R\} \equiv$  vector of time-varying forces and moments applied upon the system.

### 2.2.3.2 Lagrange Approach (ii)

This approach differs from the just completed previous Lagrange approach only in how the gyroscopic moment is derived; hence only that facet is shown here. Specifically, the issue is the portion of the disk's rotational kinetic energy ( $T_{\text{rot}}$ ) due to its spin velocity. Using a coordinate system with its origin at the disk's mass center and its axes aligned with principal-inertia axes through the disk's mass center, the disk's kinetic energy due to rotation can be expressed as follows:

$$T_{\text{rot}} = \frac{1}{2} \left( I_{xx} \omega_x^2 + I_{yy} \omega_y^2 + I_{zz} \omega_z^2 \right) \quad (2.19)$$

- *Initial state (all Euler angles are zero):*  $(\hat{i}, \hat{j}, \hat{k})$  aligns with  $(\hat{I}, \hat{J}, \hat{K})$ .
- *First Euler angle:* Rotate disk  $\theta_y$  about the  $y$ -axis (i.e.,  $\hat{i}, \hat{k}$  about  $\hat{j} = \hat{J}$ ),

$$(\hat{i}, \hat{j}, \hat{k}) \text{ moves to } (\hat{i}', \hat{j}', \hat{k}'), \quad \text{where } \hat{j}' = \hat{j} = \hat{J}$$

- *Second Euler angle:* Rotate disk  $\theta_x$  about the  $x$ -axis (i.e.,  $\hat{j}', \hat{k}'$  about  $\hat{i}'$ ),

$$(\hat{i}', \hat{j}', \hat{k}') \text{ moves to } (\hat{i}'', \hat{j}'', \hat{k}''), \quad \text{where } \hat{i}'' = \hat{i}'$$

- *Third Euler angle:* Rotate the disk  $\phi$  about the  $z$ -axis (i.e.,  $\hat{i}'', \hat{j}''$  about  $\hat{k}''$ ),

$$(\hat{i}'', \hat{j}'', \hat{k}'') \text{ moves to } (\hat{i}, \hat{j}, \hat{k}), \quad \text{where } \hat{k}'' = \hat{k}$$

The following angular velocity vector for the disk is now specified in components that are legitimate for use in the Lagrange approach since each velocity component is the first time derivative of a generalized coordinate:

$$\begin{aligned} \vec{\omega}_{\text{total}} &= \dot{\theta}_y \hat{j} + \dot{\theta}_x \hat{i}' + \dot{\phi} \hat{k} \\ \omega &= \dot{\phi} \end{aligned} \quad (2.20)$$

The remaining step is to transform  $\hat{J}$  and  $\hat{i}'$  in Equation 2.20 into their  $(\hat{i}, \hat{j}, \hat{k})$  components to obtain the disk's angular velocity components in a principal-inertia  $x$ - $y$ - $z$  coordinate system. This is accomplished simply by using the following associated direction-cosine orthogonal transformations:

$$\begin{aligned} \begin{Bmatrix} \hat{i}' \\ \hat{j}' \\ \hat{k}' \end{Bmatrix} &= \begin{bmatrix} \cos \theta_y & 0 & -\sin \theta_y \\ 0 & 1 & 0 \\ \sin \theta_y & 0 & \cos \theta_y \end{bmatrix} \begin{Bmatrix} \hat{I} \\ \hat{J} \\ \hat{K} \end{Bmatrix} \\ \begin{Bmatrix} \hat{i}'' \\ \hat{j}'' \\ \hat{k}'' \end{Bmatrix} &= \begin{bmatrix} 1 & 0 & 0 \\ 0 & \cos \theta_x & \sin \theta_x \\ 0 & -\sin \theta_x & \cos \theta_x \end{bmatrix} \begin{Bmatrix} \hat{i}' \\ \hat{j}' \\ \hat{k}' \end{Bmatrix} \\ \begin{Bmatrix} \hat{i} \\ \hat{j} \\ \hat{k} \end{Bmatrix} &= \begin{bmatrix} \cos \phi & \sin \phi & 0 \\ -\sin \phi & \cos \phi & 0 \\ 0 & 0 & 1 \end{bmatrix} \begin{Bmatrix} \hat{i}'' \\ \hat{j}'' \\ \hat{k}'' \end{Bmatrix} \end{aligned} \quad (2.21)$$



Multiplying these three orthogonal matrices together according to the proper Euler angle sequence yields an equation of the following form:

$$\begin{Bmatrix} \hat{\mathbf{i}} \\ \hat{\mathbf{j}} \\ \hat{\mathbf{k}} \end{Bmatrix} = [R_\phi] [R_{\theta_x}] [R_{\theta_y}] \begin{Bmatrix} \hat{\mathbf{I}} \\ \hat{\mathbf{J}} \\ \hat{\mathbf{K}} \end{Bmatrix} \quad (2.22)$$

Equation 2.22, product of the three orthogonal transformation matrices, is also an orthogonal matrix, embodying the total orthogonal transformation from the initial state to the end state orientation following application of the three Euler angles, and can be expressed as follows:

$$[R] = [R_\phi] [R_{\theta_x}] [R_{\theta_y}] \quad (2.23)$$

As an orthogonal matrix,  $[R]$  has an inverse equal to its transpose. Therefore, the  $\hat{\mathbf{J}}$  unit vector in Equation 2.20 is obtained from the second equation of the following three

$$\begin{Bmatrix} \hat{\mathbf{I}} \\ \hat{\mathbf{J}} \\ \hat{\mathbf{K}} \end{Bmatrix} = [R]^T \begin{Bmatrix} \hat{\mathbf{i}} \\ \hat{\mathbf{j}} \\ \hat{\mathbf{k}} \end{Bmatrix} \quad (2.24)$$

to obtain the following expression for  $\hat{\mathbf{J}}$ :

$$\hat{\mathbf{J}} = (\sin \phi \cos \theta_x) \hat{\mathbf{i}} + (\cos \phi \cos \theta_x) \hat{\mathbf{j}} - (\sin \theta_x) \hat{\mathbf{k}} \quad (2.25)$$

Since  $\hat{\mathbf{i}}' = \hat{\mathbf{i}}''$ , inverting the 3rd of Equations 2.21 yields the following:

$$\hat{\mathbf{i}}' = \hat{\mathbf{i}} \cos \phi - \hat{\mathbf{j}} \sin \phi \quad (2.26)$$

Substituting Equations 2.25 and 2.26 into Equation 2.20 produces the following result:

$$\begin{aligned} \bar{\omega} &= (\dot{\theta}_y \sin \phi \cos \theta_x + \dot{\theta}_x \cos \phi) \hat{\mathbf{i}} + (\dot{\theta}_y \cos \phi \cos \theta_x - \dot{\theta}_x \sin \phi) \hat{\mathbf{j}} \\ &\quad + (-\dot{\theta}_y \sin \theta_x + \omega) \hat{\mathbf{k}} \end{aligned} \quad (2.27)$$

Equation 2.27 provides the proper components for  $\omega_x$ ,  $\omega_y$ , and  $\omega_z$  to insert into Equation 2.19 for the disk's rotational kinetic energy,  $T_{\text{rot}}$ , as follows:

$$\begin{aligned} T_{\text{rot}} &= \frac{1}{2} I_T (\omega_x^2 + \omega_y^2) + \frac{1}{2} I_P \omega_z^2 = \frac{1}{2} [I_T (\dot{\theta}_y \sin \phi \cos \theta_x + \dot{\theta}_x \cos \phi)^2 \\ &\quad + I_T (\dot{\theta}_y \cos \phi \cos \theta_x - \dot{\theta}_x \sin \phi)^2 + I_P (-\dot{\theta}_y \sin \theta_x + \omega)^2] \end{aligned} \quad (2.28)$$

Simplifications utilizing  $\cos \theta_x \cong 1$ ,  $\sin \theta_x \cong \theta_x$ , and  $\sin^2 \theta_x \ll \sin \theta_x$  then yield the following expression for the disk's rotational kinetic energy:

$$T_{\text{rot}} = \frac{1}{2} \left[ I_T (\dot{\theta}_x^2 + \dot{\theta}_y^2) + I_P (\omega^2 - 2\omega \dot{\theta}_y \theta_x) \right] \quad (2.29)$$

A potential point of confusion is avoided here if one realizes that  $\theta_x$  and  $\theta_y$  are both very small and are applied in the Euler angle sequence ahead of  $\phi$ , which is not small ( $\phi = \omega t$ ). Thus,  $\dot{\theta}_x$  and  $\dot{\theta}_y$  are directed along axes that are basically aligned with the nonrotating inertial  $x$ - $y$  coordinates, not those spinning with the disk. As with the Lagrange approach (i), the disk's total kinetic energy is expressible as the sum of the mass-center kinetic energy plus the rotational kinetic energy as follows:

$$T_{\text{disk}} = T_{\text{cg}} + T_{\text{rot}} \quad (2.30)$$

The total system kinetic energy is thus expressible for this Lagrange approach by the following equation:

$$T = \frac{1}{2} \left[ m_1 (\dot{x}_1^2 + \dot{y}_1^2) + m_2 (\dot{x}_2^2 + \dot{y}_2^2) + I_T (\theta_x^2 + \theta_y^2) + I_P (\omega^2 - 2\omega \dot{\theta}_y \theta_x) + m_3 (\dot{x}_3^2 + \dot{y}_3^2) \right] \quad (2.31)$$

Equation 2.31 differs from its Lagrange approach (i) counterpart, Equation 2.12, only by its  $I_P$  term that contains the disk's gyroscopic effect.

The potential energy formulation and bearing dynamic force expressions used here are identical to those in Lagrange approach (i), Equations 2.11 and 2.13, respectively. However, here the gyroscopic effect is contained within the kinetic energy function in Equation 2.31. Therefore, Equations 2.17 used in the Lagrange approach (i) for gyroscopic moment components upon the disk are not applicable here. Implementing the clearly indicated math steps implicit in Equations 2.4, this approach yields the same eight equations given by Equations 2.18.

### 2.2.3.3 Direct $F = ma$ Approach

In this approach, the sum of  $x$ -forces and the sum of  $y$ -forces on  $m_1$ ,  $m_2$ , and  $m_3$  equated to their respective  $m\ddot{q}$  terms yields six of the eight motion equations. The sum of  $x$ -moments and the sum of  $y$ -moments on the disk equated to their respective  $I_T\ddot{\theta}$  terms yields the other two motion equations. This can be summarized as follows.

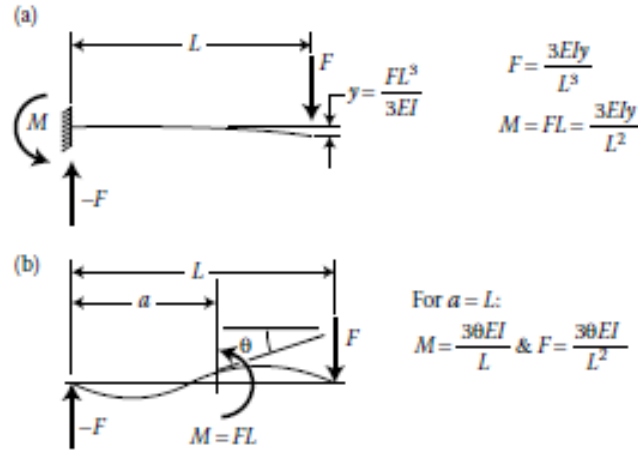


FIGURE 2.6 Beam deflection formulas.

Bearing forces and gyroscopic moment are taken directly from Equations 2.13 and 2.17, respectively. Thus, only the beam-deflection reaction forces and moments need developing here, and these can be derived using superposition of the two cases given in Figure 2.6. All reaction force and moment components due to  $x$  and  $y$  translations with  $\theta_x$  and  $\theta_y$  both zero are obtained using the *cantilever beam* end-loaded case given in Figure 2.6a. Likewise, all reaction force and moment components due to  $\theta_x$  and  $\theta_y$  with  $x$  and  $y$  translations both zero are obtained using the *simply supported beam* with an end moment, that is, case with  $a = L$  in Figure 2.6b. Superimposing these two cases provides all the beam reaction force and moment components due to all eight displacements and these are summarized as follows:

Beam-Deflection Reaction	Force and Moment Components	
$f_{1x} = \frac{3EI}{L^3}(-x_1 + x_2 - \theta_y L)$	$M_{2x} = \frac{3EI}{L^3}(y_1 L - 2\theta_x L^2 - y_3 L)$	
$f_{1y} = \frac{3EI}{L^3}(-y_1 + y_2 + \theta_x L)$	$M_{2y} = \frac{3EI}{L^3}(-x_1 L - 2\theta_y L^2 + x_3 L)$	(2.32)
$f_{2x} = \frac{3EI}{L^3}(x_1 - 2x_2 + x_3)$	$f_{3x} = \frac{3EI}{L^3}(x_2 - x_3 + \theta_y L)$	
$f_{2y} = \frac{3EI}{L^3}(y_1 - 2y_2 + y_3)$	$f_{3y} = \frac{3EI}{L^3}(y_2 - y_3 - \theta_x L)$	

The eight equations of motion are constructed from  $F = ma$  and  $M = I\ddot{\theta}$  utilizing Equations 2.13 for bearing forces, Equations 2.17 for gyroscopic

moments, and Equations 2.32 for beam-bending force and moment reactions, as follows:

$$\begin{aligned}
 m_1 \ddot{x}_1 &= f_{1x} + f_x^{(1)} & I_T \ddot{\theta}_x &= M_{2x} + M_{gyro,x} \\
 m_1 \ddot{y}_1 &= f_{1y} + f_y^{(1)} & I_T \ddot{\theta}_y &= M_{2y} + M_{gyro,y} \\
 m_2 \ddot{x}_2 &= f_{2x} & m_3 \ddot{x}_3 &= f_{3x} + f_x^{(2)} \\
 m_2 \ddot{y}_2 &= f_{2y} & m_3 \ddot{y}_3 &= f_{3y} + f_y^{(2)}
 \end{aligned} \tag{2.33}$$

Substituting the appropriate expressions from Equations 2.13, 2.17, and 2.32 into Equations 2.33 yields the 8-DOF model's equations of motion given in Equations 2.18.

Equations 2.18 have been derived here in three somewhat different approaches. However, all three approaches are based on Newton's second law and thus must yield the same result.

The right-hand side of Equations 2.18,  $\{R\}$ , is strictly for time-dependent forcing functions and viewed as being externally applied on the system. No specific examples of  $\{R\}$  were needed to develop the three derivations of Equations 2.18, but two important cases are now delineated: (i) *eigenvalue extraction* and (ii) *steady-state unbalance response*. For eigenvalue extraction, such as performed in searching for operating zones where dynamic instability (self-excited vibration) is predicted,  $\{R\} = 0$  can be used since  $\{R\}$  does not enter into that mathematical process (see Section 1.3, subheading "Dynamic Instability: The Complex Eigenvalue Problem"). For an unbalance response example, the combination of so-called *static unbalance* and *dynamic unbalance* are simultaneously applied on the 8-DOF model's disk, as shown in Figure 2.7. An unbalance is modeled by its equivalent centrifugal force.

Here, the static unbalance mass is chosen as the angular reference point (*key phaser*) on the rotor and  $\phi$  ( $90^\circ$  for illustrated case in Figure 2.7) is the phase angle between  $m_s$  and the rotating moment produced by the two  $180^\circ$  out-of-phase  $m_d$  dynamic unbalance masses. Equations 2.18 then have the

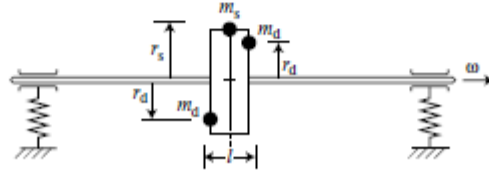


FIGURE 2.7 Combination of static and dynamic rotor disk unbalance.

right-hand side  $\{R\}$  shown in the following equations:

$$[M]\{\ddot{q}\} + [C]\{\dot{q}\} + [K]\{q\} = \omega^2 \begin{Bmatrix} 0 \\ 0 \\ m_s r_s \cos \omega t \\ m_s r_s \sin \omega t \\ m_d r_d l \cos(\omega t + \phi) \\ m_d r_d l \sin(\omega t + \phi) \\ 0 \\ 0 \end{Bmatrix} \quad (2.34)$$

The four zeros in  $\{R\}$  reflect *no unbalances* at the two bearing stations.

---

### 2.3 Formulations for RDA Software

The vibration fundamentals covered in Chapter 1 and the foregoing sections of this chapter provide ample background to follow the development of the governing formulations for the RDA code. RDA is a user-friendly PC-based user-interactive software package that is structured on the finite-element method. It was developed in the Rotor Dynamics Laboratory at Case Western Reserve University to handle the complete complement of *linear LRV analyses*, and it is supplied with this book. In this section, the focus is on formulation, solution, and computation aspects of the RDA code. In Part 2 of this book (Chapters 4, 5, and 6), the focus shifts to the use of RDA in problem solving.

#### 2.3.1 Basic Rotor Finite Element

Development of the RDA model starts with the *basic rotor finite-element building block*, which is comprised of two disks (or any  $M, I_T, I_P$ ) connected by a beam of uniform circular-cross-section (shaft), as shown in Figure 2.8.

For the rotor finite element shown in Figure 2.8, the following two lists summarize its elementary parameters.

*Shaft element properties:*

$$\begin{aligned} \text{Mass, } M^{(s)} &= \frac{\gamma_s \pi (d_o^2 - d_i^2) L}{4g} \\ \text{Transverse inertia at c.g., } I_T^{(s)} &= \frac{1}{12} M^{(s)} \left[ 3 \left( \frac{d_o^2 + d_i^2}{4} \right) + L^2 \right] \\ \text{Polar inertia, } I_P^{(s)} &= \frac{1}{2} M^{(s)} \left( \frac{d_o^2 + d_i^2}{4} \right) \end{aligned} \quad (2.35a)$$



Development of the RDA model starts with the *basic rotor finite-element building block*, which is comprised of two disks (or any  $M, I_T, I_P$ ) connected by a beam of uniform circular-cross-section (shaft), as shown in Figure 2.8.

For the rotor finite element shown in Figure 2.8, the following two lists summarize its elementary parameters.

*Shaft element properties:*

$$\begin{aligned} \text{Mass, } M^{(s)} &= \frac{\gamma_s \pi (d_o^2 - d_i^2) L}{4g} \\ \text{Transverse inertia at c.g., } I_T^{(s)} &= \frac{1}{12} M^{(s)} \left[ 3 \left( \frac{d_o^2 + d_i^2}{4} \right) + L^2 \right] \\ \text{Polar inertia, } I_P^{(s)} &= \frac{1}{2} M^{(s)} \left( \frac{d_o^2 + d_i^2}{4} \right) \end{aligned} \quad (2.35a)$$

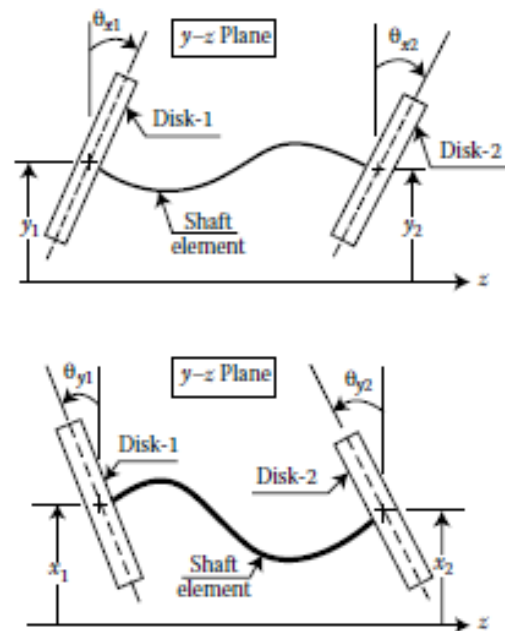


FIGURE 2.8 Basic rotor finite-element building block.

$$\text{Area moment of inertia, } I = \frac{\pi (d_o^4 - d_i^4)}{64}$$

Modulus of elasticity,  $E$

where  $d_o$  is the shaft outside diameter (OD),  $d_i$  is the shaft inside diameter (ID) (optional concentric hole),  $L$  is the shaft length,  $\gamma_s$  is the shaft weight density and  $g$  is the gravity constant



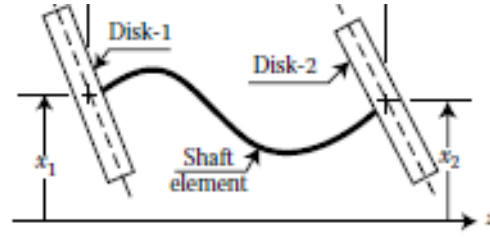


FIGURE 2.8 Basic rotor finite-element building block.

$$\text{Area moment of inertia, } I = \frac{\pi(d_o^4 - d_i^4)}{64}$$

Modulus of elasticity,  $E$

where  $d_o$  is the shaft outside diameter (OD),  $d_i$  is the shaft inside diameter (ID) (optional concentric hole),  $L$  is the shaft length,  $\gamma_s$  is the shaft weight density, and  $g$  is the gravity constant.

The formulas for concentrated disk masses are essentially the same as those for the shaft element, and thus listed here as follows.

*Concentrated disk mass properties:*

Any axially symmetric mass specified by its  $M$ ,  $I_T$ , and  $I_P$  can be used, for example, couplings, impellers, gears, and so on

$$\text{Mass, } M^{(d)} = \frac{\gamma_d \pi (D_o^2 - D_i^2) l}{4g}$$

$$\text{Transverse inertia at c.g., } I_T^{(d)} = \frac{1}{12} M^{(d)} \left[ 3 \left( \frac{D_o^2 + D_i^2}{4} \right) + l^2 \right] \quad (2.35b)$$

$$\text{Polar inertia, } I_P^{(d)} = \frac{1}{2} M^{(d)} \left( \frac{D_o^2 + D_i^2}{4} \right)$$

theorem, shown as follows:

$$I_{Ti} = \frac{1}{12} \left( \frac{M^{(s)}}{2} \right) \left[ 3 \left( \frac{d_o^2 + d_i^2}{4} \right) + \left( \frac{L}{2} \right)^2 \right] + \frac{M^{(s)}}{2} \left( \frac{L}{4} \right)^2 \quad (2.36)$$

With the coordinate vector ordering  $\{x_1, y_1, \theta_{x1}, \theta_{y1}, x_2, y_2, \theta_{x2}, \theta_{y2}\}$  employed, the shaft element *lumped mass* matrix is then as follows:

$$[M]_i^l = \begin{bmatrix} \frac{1}{2}M_i^{(s)} & 0 & 0 & 0 & 0 & 0 & 0 & 0 \\ 0 & \frac{1}{2}M_i^{(s)} & 0 & 0 & 0 & 0 & 0 & 0 \\ 0 & 0 & I_{Ti} & 0 & 0 & 0 & 0 & 0 \\ 0 & 0 & 0 & I_{Ti} & 0 & 0 & 0 & 0 \\ 0 & 0 & 0 & 0 & \frac{1}{2}M_i^{(s)} & 0 & 0 & 0 \\ 0 & 0 & 0 & 0 & 0 & \frac{1}{2}M_i^{(s)} & 0 & 0 \\ 0 & 0 & 0 & 0 & 0 & 0 & I_{Ti} & 0 \\ 0 & 0 & 0 & 0 & 0 & 0 & 0 & I_{Ti} \end{bmatrix} \quad (2.37)$$

### 2.3.3 Shaft Element Distributed Mass Matrix

The underlying assumption for the distributed mass formulation is that the shaft element's lateral acceleration varies linearly in the axial direction, a logical first-order improvement over the axial step-change approximation implicit in the lumped mass formulation. An axial linear variation of lateral acceleration requires that the element's lateral velocity also varies linearly in the axial direction. The derivation here considers two adjacent mass stations, as shown in Figure 2.9, to formulate the linear variation of lateral velocity.

The linear variation of  $x$ -velocity is expressed as follows:

$$\dot{x} = \dot{x}_i + \frac{1}{L_i} (\dot{x}_{i+1} - \dot{x}_i) z \quad (2.38)$$

expressed as follows (similar for  $y$ -translation kinetic energy):

$$T_i^{(x)} = \frac{1}{2} \frac{M_i^{(s)}}{L_i} \int_0^{L_i} \dot{x}^2 dz \quad (2.39)$$

Substituting Equation 2.38 into Equation 2.39 and integrating yields the portion of the total system's kinetic energy function that is needed to extract the shaft element's lateral acceleration terms associated with the  $x_i$  and  $x_{i+1}$  Lagrange equations of motion. This leads to the following two results:

$$\begin{aligned} \frac{d}{dt} \left( \frac{\partial T}{\partial \dot{x}_i} \right) &= \frac{1}{3} M_i^{(s)} \ddot{x}_i + \frac{1}{6} M_i^{(s)} \ddot{x}_{i+1} \\ \frac{d}{dt} \left( \frac{\partial T}{\partial \dot{x}_{i+1}} \right) &= \frac{1}{6} M_i^{(s)} \ddot{x}_i + \frac{1}{3} M_i^{(s)} \ddot{x}_{i+1} \end{aligned} \quad (2.40)$$

Since the beam element transverse rotary inertia effect is secondary to its lateral mass acceleration effect, the inclusion of shaft element transverse rotary inertia is included here, as already shown for the lumped mass formulation, Equations 2.36. That is, beam element transverse moment of inertia is not “distributed” in the manner just derived for the lateral mass acceleration components. With the coordinate vector ordering  $\{x_1, y_1, \theta_{x1}, \theta_{y1}, x_2, y_2, \theta_{x2}, \theta_{y2}\}$  employed, the shaft element’s *distributed mass* matrix thus obtained is as follows:

[illegible]

### 2.3.4 Shaft Element Consistent Mass Matrix

When the spatial distribution of acceleration (and therefore velocity) in a finite element is formulated with the same shape function as static deflection, it is referred to as the consistent mass approach. The shaft element in Figure 2.8 is postulated to be a uniform cross-section beam in bending. Thus, its static beam deflection can be expressed as cubic functions in the

$x$ - $z$  and  $y$ - $z$  planes, as follows ( $z$  referenced to left mass station, as shown in Figure 2.9):

$$\Psi(z) = az^3 + bz^2 + cz + d \quad (2.42)$$

A general state of shaft element deflection in a plane ( $x$ - $z$  or  $y$ - $z$ ) can be expressed as a linear superposition of four cases, each having a unity displacement for one of the four generalized coordinates in the plane with zero displacement for the other three coordinates in the plane. These four cases are specified by the following tabulated sets of boundary conditions.

*Correspondence between  $\Psi_j, \Psi'_j$  and Rotor Element Coordinates*

$x$ - $z$ plane $\rightarrow$	$x_1$	$\theta_{y1}$	$x_2$	$\theta_{y2}$
$y$ - $z$ plane $\rightarrow$	$y_1$	$-\theta_{x1}$	$y_2$	$-\theta_{x2}$
Case 1:	$\Psi_1(0) = 1$	$\Psi'_1(0) = 0$	$\Psi_1(L) = 0$	$\Psi'_1(L) = 0$
Case 2:	$\Psi_2(0) = 0$	$\Psi'_2(0) = 1$	$\Psi_2(L) = 0$	$\Psi'_2(L) = 0$
Case 3:	$\Psi_3(0) = 0$	$\Psi'_3(0) = 0$	$\Psi_3(L) = 1$	$\Psi'_3(L) = 0$
Case 4:	$\Psi_4(0) = 0$	$\Psi'_4(0) = 0$	$\Psi_4(L) = 0$	$\Psi'_4(L) = 1$

Correspondence between  $\Psi_j, \Psi'_j$  and Rotor Element Coordinates

$x-z$ plane $\rightarrow$	$x_1$	$\theta_{y1}$	$x_2$	$\theta_{y2}$
$y-z$ plane $\rightarrow$	$y_1$	$-\theta_{x1}$	$y_2$	$-\theta_{x2}$
Case 1:	$\Psi_1(0) = 1$	$\Psi'_1(0) = 0$	$\Psi_1(L) = 0$	$\Psi'_1(L) = 0$
Case 2:	$\Psi_2(0) = 0$	$\Psi'_2(0) = 1$	$\Psi_2(L) = 0$	$\Psi'_2(L) = 0$
Case 3:	$\Psi_3(0) = 0$	$\Psi'_3(0) = 0$	$\Psi_3(L) = 1$	$\Psi'_3(L) = 0$
Case 4:	$\Psi_4(0) = 0$	$\Psi'_4(0) = 0$	$\Psi_4(L) = 0$	$\Psi'_4(L) = 1$

Substituting each of the four above boundary condition sets into Equation 2.42 and solving in each case for the four coefficients in Equation 2.42 yields the following four *deflection shape functions*:

$$\begin{aligned}\Psi_1(z) &= 1 - 3\left(\frac{z}{L}\right)^2 + 2\left(\frac{z}{L}\right)^3, & \Psi_2(z) &= z - 2\frac{z^2}{L} + \frac{z^3}{L^2} \\ \Psi_3(z) &= 3\left(\frac{z}{L}\right)^2 - 2\left(\frac{z}{L}\right)^3, & \Psi_4 &= \frac{z^2}{L}\left(\frac{z}{L} - 1\right)\end{aligned}\quad (2.43)$$

The general state of shaft element deflection can be expressed as follows:

$$\begin{aligned}x &= x_1\Psi_1(z) + \theta_{y1}\Psi_2(z) + x_2\Psi_3(z) + \theta_{y2}\Psi_4(z) \\ y &= y_1\Psi_1(z) - \theta_{x1}\Psi_2(z) + y_2\Psi_3(z) - \theta_{x2}\Psi_4(z)\end{aligned}\quad (2.44)$$

Thus, the general state of shaft element velocity can be expressed as follows:

$$\begin{aligned}\dot{x} &= \dot{x}_1\Psi_1(z) + \dot{\theta}_{y1}\Psi_2(z) + \dot{x}_2\Psi_3(z) + \dot{\theta}_{y2}\Psi_4(z) \\ \dot{y} &= \dot{y}_1\Psi_1(z) - \dot{\theta}_{x1}\Psi_2(z) + \dot{y}_2\Psi_3(z) - \dot{\theta}_{x2}\Psi_4(z)\end{aligned}\quad (2.45)$$

The total shaft element kinetic energy is derived by substituting Equations 2.45 into the following equation:

$$T_i = \frac{1}{2} \frac{M_i^{(s)}}{L_i} \int_0^{L_i} (\dot{x}^2 + \dot{y}^2) dz \quad (2.46)$$

The element consistent mass matrix is obtained by substituting the integrated result from Equation 2.46 into the acceleration portion for each of the eight Lagrange equations for the shaft element, as follows:

$$\frac{d}{dt} \left( \frac{\partial T_i}{\partial \dot{q}_r} \right) \equiv [M_{rs}]_i^c \{\ddot{q}_s\}, \quad r = 1, 2, \dots, 8 \quad (2.47)$$

With  $\{\ddot{q}_s\} = \{\ddot{x}_1, \ddot{y}_1, \ddot{\theta}_{x1}, \ddot{\theta}_{y1}, \ddot{x}_2, \ddot{y}_2, \ddot{\theta}_{x2}, \ddot{\theta}_{y2}\}$ , the shaft element *consistent mass matrix* thus obtained is as follows:

$$[M]_i^c = \frac{M_i^{(s)}}{420} \begin{bmatrix} 156 & 0 & 0 & 22L_i & 54 & 0 & 0 & -13L_i \\ 0 & 156 & -22L_i & 0 & 0 & 54 & 13L_i & 0 \\ 0 & -22L_i & 4L_i^2 & 0 & 0 & 0 & 0 & 0 \\ 22L_i & 0 & 0 & 4L_i^2 & 13L_i & 0 & 0 & -3L_i^2 \\ 54 & 0 & 0 & 13L_i & 156 & 0 & 0 & -22L_i \\ 0 & 54 & 0 & 0 & 0 & 156 & 22L_i & 0 \\ 0 & 13L_i & 0 & 0 & 0 & 22L_i & 4L_i^2 & 0 \\ -13L_i & 0 & 0 & -3L_i^2 & -22L_i & 0 & 0 & 4L_i^2 \end{bmatrix} \quad (2.48)$$

### 2.3.5 Shaft Element Stiffness Matrix

Borrowing from Equation 2.5, the potential energy for the shaft element in bending can be expressed as follows:

$$V_i = \frac{1}{2} E_i I_i \int_0^{L_i} [(x'')^2 + (y'')^2] dz \quad (2.49)$$



### 2.3.5 Shaft Element Stiffness Matrix

Borrowing from Equation 2.5, the potential energy for the shaft element in bending can be expressed as follows:

$$V_i = \frac{1}{2} E_i I_i \int_0^{L_i} [(x'')^2 + (y'')^2] dz \quad (2.49)$$

Substituting Equations 2.44 into Equation 2.49 provides the shaft element  $V_i$  as a function of the element's eight generalized coordinates, similar to the detailed development of Equation 2.11 for the 8-DOF "Simple Nontrivial Model." The element stiffness matrix is obtained by substituting the integrated result from Equation 2.49 into the potential energy

term for each of the eight Lagrange equations for the shaft element, as follows:

$$\frac{\partial V_i}{\partial q_r} \equiv [K_{rs}]_i \{q_s\}, \quad r = 1, 2, \dots, 8 \quad (2.50)$$

With  $\{q_s\} = \{x_1, y_1, \theta_{x1}, \theta_{y1}, x_2, y_2, \theta_{x2}, \theta_{y2}\}$ , the element *stiffness* matrix thus obtained is as follows:

$$[K]_i = \frac{2E_i I_i}{L_i^3} \begin{bmatrix} 6 & 0 & 0 & 3L_i & -6 & 0 & 0 & 3L_i \\ 0 & 6 & -3L_i & 0 & 0 & -6 & -3L_i & 0 \\ 0 & -3L_i & 2L_i^2 & 0 & 0 & 3L_i & L_i^2 & 0 \\ 3L_i & 0 & 0 & 2L_i^2 & -3L_i & 0 & 0 & L_i^2 \\ -6 & 0 & 0 & -3L_i & 6 & 0 & 0 & -3L_i \\ 0 & -6 & 3L_i & 0 & 0 & 6 & 3L_i & 0 \\ 0 & -3L_i & L_i^2 & 0 & 0 & 3L_i & 2L_i^2 & 0 \\ 3L_i & 0 & 0 & L_i^2 & -3L_i & 0 & 0 & 2L_i^2 \end{bmatrix} \quad (2.51)$$



### 2.3.8 Matrices for Complete Free-Free Rotor

The  $[M]$ ,  $[C]$ , and  $[K]$  matrices for the complete *free-free* rotor (i.e., *free of connections to ground and free of external forces*) are assembled by linking all the corresponding individual rotor-element matrices. The right mass station of each rotor element is overlaid on to the left mass station of its immediate right neighbor. Thus, the total number of rotor mass stations ( $N_{ST}$ ) is equal to the total number of rotor elements ( $N_{EL}$ ) plus one. The total

number of rotor DOFs is 4 times  $N_{ST}$ .

$$\begin{aligned} N_{ST} &= N_{EL} + 1 \\ N_{RDOF} &= 4N_{ST} \end{aligned} \quad (2.55)$$

Accordingly, the rotor matrices are expressible as follows:

$$[M]_R = \begin{bmatrix} [M'_1] & & & \\ & [M'_2] & & \\ & & [M'_3] & \\ & & & \ddots \\ & & & & [M'_{N_{EL}}] \end{bmatrix} \quad (2.56)$$

$N_{RDOF} \times N'_{RDOF}$

$$[C]_R = \begin{bmatrix} [G'_1] & & & \\ & [G'_2] & & \\ & & [G'_3] & \\ & & & \ddots \\ & & & & [G'_{N_{EL}}] \end{bmatrix} \quad (2.57)$$

$N_{RDOF} \times N'_{RDOF}$

$$[K]_R = \begin{bmatrix} [K'_1] & & & \\ & [K'_2] & & \\ & & [K'_3] & \\ & & & \ddots \\ & & & & [K'_{N_{EL}}] \end{bmatrix} \quad (2.58)$$

$N_{RDOF} \times N'_{RDOF}$

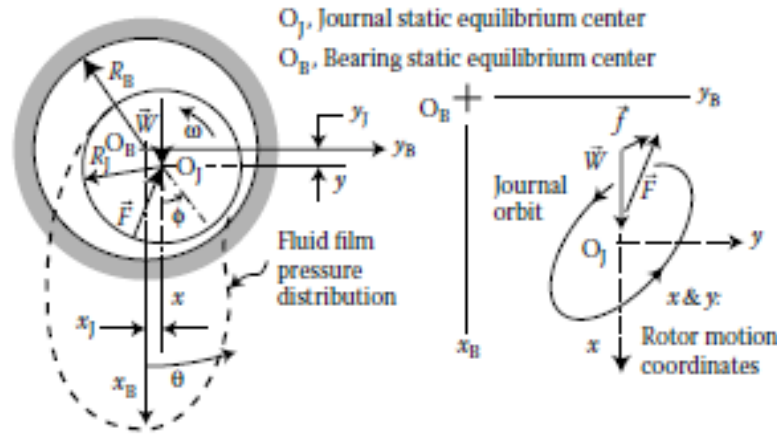


FIGURE 2.10 Force vectors and rotor-to-bearing vibration orbit at a bearing.

position and velocity components. This assumes that lubricant viscosity effects are dominant and lubricant fluid inertia effects are negligible; otherwise journal-to-bearing acceleration component effects should also be included. A continuous function that also has continuous derivatives to any order can be expanded in a Taylor series. Therefore, relative to the static equilibrium state, the  $x$  and  $y$  components of the dynamic-deviation of bearing force *upon the rotor* can be expressed as follows (under static equilibrium,  $\vec{F} + \vec{W} = 0$ ):

$$\begin{aligned} F_x + W_x = f_x &= \frac{\partial F_x}{\partial x} x + \frac{\partial F_x}{\partial \dot{x}} \dot{x} + \frac{\partial F_x}{\partial y} y + \frac{\partial F_x}{\partial \dot{y}} \dot{y} + (\text{higher-order terms}) \\ F_y + W_y = f_y &= \frac{\partial F_y}{\partial x} x + \frac{\partial F_y}{\partial \dot{x}} \dot{x} + \frac{\partial F_y}{\partial y} y + \frac{\partial F_y}{\partial \dot{y}} \dot{y} + (\text{higher-order terms}) \end{aligned} \quad (2.60)$$

it is convenient to put Equations 2.60 into the following matrix form:

$$\begin{Bmatrix} f_x \\ f_y \end{Bmatrix} = - \begin{bmatrix} k_{xx} & k_{xy} \\ k_{yx} & k_{yy} \end{bmatrix} \begin{Bmatrix} x \\ y \end{Bmatrix} - \begin{bmatrix} c_{xx} & c_{xy} \\ c_{yx} & c_{yy} \end{bmatrix} \begin{Bmatrix} \dot{x} \\ \dot{y} \end{Bmatrix} \quad (2.61)$$

$$[K]\{q\} = \left[ \begin{array}{cc} \left[ \frac{12E_i I_i}{L_i^3} + k_{xx}^{(n)} & k_{xy}^{(n)} \right] \\ k_{yx}^{(n)} & \frac{12E_i I_i}{L_i^3} + k_{yy}^{(n)} \end{array} \right]_{N_{\text{RDOF}} \times N_{\text{RDOF}}} \begin{Bmatrix} \vdots \\ x \\ y \\ \vdots \end{Bmatrix} \quad (2.62)$$

Similarly,  $[C] = [C]_R + [C]_B$ , where  $[C]_B \equiv N_{\text{RDOF}} \times N_{\text{RDOF}}$  matrix containing all the bearing damping coefficients in their proper locations.

$$[C]\{\dot{q}\} = \left[ \begin{array}{cc} \left[ \begin{array}{cc} c_{xx}^{(n)} & c_{xy}^{(n)} \\ c_{yx}^{(n)} & c_{yy}^{(n)} \end{array} \right] \\ \end{array} \right]_{N_{\text{RDOF}} \times N_{\text{RDOF}}} \begin{Bmatrix} \vdots \\ \dot{x} \\ \dot{y} \\ \vdots \end{Bmatrix} \quad (2.63)$$

where  $n$  is the bearing no.  $= 1, 2, \dots, N_B$ .

$$[M] = [M]_R \quad (2.64)$$

For this option, the total number of DOFs is  $N_{\text{DOF}} = N_{\text{RDOF}}$ . The 8-coefficient bearing model does not include any acceleration effects, thus  $[M] = [M]_R$ . At least two bearings must have nonzero principle values for their  $[k_{ij}^{(n)}]$ , for the total model stiffness matrix  $[K]$  to be nonsingular, which is a requirement fully explained at the beginning of this subsection.

$$[M] = \begin{bmatrix} \begin{bmatrix} 4 \times 4 \end{bmatrix} & \begin{bmatrix} 0 & 0 \\ 0 & 0 \\ 0 & 0 \\ 0 & 0 \end{bmatrix} & \begin{bmatrix} 4 \times N_{\text{RDOF}} \end{bmatrix} \\ \begin{bmatrix} 0 & 0 & 0 & 0 \\ 0 & 0 & 0 & 0 \end{bmatrix} & \begin{bmatrix} M_{\text{B},x}^{(1)} & 0 \\ 0 & M_{\text{B},y}^{(1)} \end{bmatrix} & \begin{bmatrix} 0 & 0 & 0 & 0 \\ 0 & 0 & 0 & 0 \end{bmatrix} \\ \begin{bmatrix} N_{\text{RDOF}} \times 4 \end{bmatrix} & \begin{bmatrix} 0 & 0 \\ 0 & 0 \\ 0 & 0 \\ 0 & 0 \end{bmatrix} & \begin{bmatrix} N_{\text{RDOF}} \times N_{\text{RDOF}} \end{bmatrix} \end{bmatrix} \quad (2.65)$$

Pedestal-expanded  $[C]$  and  $[K]$  matrices must be formulated to account for the bearing  $[k_{ij}^{(n)}]$  and  $[c_{ij}^{(n)}]$  stiffness and damping coefficients being driven by the differences between rotor and bearing pedestal displacement and velocity components, respectively. The  $[2 \times 4]$  and  $[4 \times 2]$  off-diagonal coefficient arrays shown within the following two equations accomplish that

$$[C] = \begin{bmatrix} \begin{bmatrix} 4 \times 4 \end{bmatrix} & \begin{bmatrix} -c_{xx}^{(1)} & -c_{yx}^{(1)} \\ -c_{xy}^{(1)} & -c_{yy}^{(1)} \\ 0 & 0 \\ 0 & 0 \end{bmatrix} & \begin{bmatrix} 4 \times N_{\text{RDOF}} \end{bmatrix} \\ \begin{bmatrix} -c_{xx}^{(1)} & -c_{xy}^{(1)} & 0 & 0 \\ -c_{yx}^{(1)} & -c_{yy}^{(1)} & 0 & 0 \end{bmatrix} & \begin{bmatrix} c_{xx}^{(1)} + C_{\text{B},xx}^{(1)} & c_{xy}^{(1)} + C_{\text{B},xy}^{(1)} \\ c_{yx}^{(1)} + C_{\text{B},yx}^{(1)} & c_{yy}^{(1)} + C_{\text{B},yy}^{(1)} \end{bmatrix} & \begin{bmatrix} 0 & 0 & 0 & 0 \\ 0 & 0 & 0 & 0 \end{bmatrix} \\ \begin{bmatrix} N_{\text{RDOF}} \times 4 \end{bmatrix} & \begin{bmatrix} 0 & 0 \\ 0 & 0 \\ 0 & 0 \\ 0 & 0 \end{bmatrix} & \begin{bmatrix} N_{\text{RDOF}} \times N_{\text{RDOF}} \end{bmatrix} \end{bmatrix} \quad (2.66)$$



$$[K] = \begin{bmatrix} \begin{bmatrix} 4 \times 4 \end{bmatrix} & \begin{bmatrix} -k_{xx}^{(1)} & -k_{yx}^{(1)} \\ -k_{xy}^{(1)} & -k_{yy}^{(1)} \\ 0 & 0 \\ 0 & 0 \end{bmatrix} & \begin{bmatrix} 4 \times N_{\text{RDOF}} \end{bmatrix} \\ \begin{bmatrix} -k_{xx}^{(1)} & -k_{xy}^{(1)} & 0 & 0 \\ -k_{yx}^{(1)} & -k_{yy}^{(1)} & 0 & 0 \end{bmatrix} & \begin{bmatrix} k_{xx}^{(1)} + K_{B,xx}^{(1)} & k_{xy}^{(1)} + K_{B,xy}^{(1)} \\ k_{yx}^{(1)} + K_{B,yx}^{(1)} & k_{yy}^{(1)} + K_{B,yy}^{(1)} \end{bmatrix} & \begin{bmatrix} 0 & 0 & 0 & 0 \\ 0 & 0 & 0 & 0 \end{bmatrix} \\ \begin{bmatrix} N_{\text{RDOF}} \times 4 \end{bmatrix} & \begin{bmatrix} 0 & 0 \\ 0 & 0 \\ 0 & 0 \\ 0 & 0 \end{bmatrix} & \begin{bmatrix} N_{\text{RDOF}} \times N_{\text{RDOF}} \end{bmatrix} \end{bmatrix} \quad (2.67)$$

For this example,  $\{q\} = \{x_1, y_1, \theta_{1x}, \theta_{1y}, x_{B,1x}, y_{B,1y}, x_2, y_2, \theta_{2x}, \theta_{2y}, \dots\}$  is the generalized coordinate vector. Note the additional two coordinates that are added at the end of station 1 rotor coordinates.

$M_{B,x}^{(n)}$  and  $M_{B,y}^{(n)}$  are the  $n$ th bearing pedestal's  $x$  and  $y$  modal masses, respectively.  $[C_{B,ij}^{(n)}]_{2 \times 2}$  and  $[K_{B,ij}^{(n)}]_{2 \times 2}$  are the  $n$ th bearing pedestal's damping and stiffness connection-to-ground coefficients, respectively. The total number of system DOFs is equal to the rotor DOF ( $N_{\text{RDOF}}$ ) plus 2 times the number of bearing pedestals ( $N_P$ ) employed in the model, where  $N_P \leq N_B$ .

$$N_{\text{DOF}} = N_{\text{RDOF}} + 2N_P \quad (2.68)$$

### 2.3.10 Completed RDA Model Equations of Motion

The complete RDA  $N_{\text{DOF}}$  equations of motion can now be written in the compact matrix form introduced in Equation 1.15. All the analysis options available within the RDA code have one of two  $\{f(t)\}$  right-hand sides as follows:  $\{f(t)\} = \{0\}$  for eigenvalue analyses (e.g., instability searches), and at rotor stations with unbalance inputs, for steady-state unbalance response.

$$\begin{Bmatrix} \vdots \\ f_x \\ f_y \\ \vdots \end{Bmatrix} = \omega^2 \begin{Bmatrix} \vdots \\ m_{ub} r_{ub} \cos(\omega t + \phi_{ub}) \\ m_{ub} r_{ub} \sin(\omega t + \phi_{ub}) \\ \vdots \end{Bmatrix} \quad (2.69)$$

### 2.4.3 Isotropic Model

The underlying assumptions for the isotropic model are that (i) the rotating and nonrotating members forming an annular fluid-filled gap are concentric; (ii) the annular gap has geometric variations, if any, in the axial direction only; and (iii) the inlet flow boundary conditions are rotationally symmetric. As a consequence, it is assumed that the rotor orbital vibrations impose only small dynamic perturbations upon an otherwise rotationally symmetric primary steady flow field within the annular gap. Rotational symmetry requires that the  $k_{ij}$ ,  $c_{ij}$ , and  $m_{ij}$  coefficients in Equation 2.70 be invariant to orthogonal transformation, that is, have the same values in all orientations of the radial plane  $x$ – $y$  coordinate system. It is relevant to mention here that  $k_{ij}$ ,  $c_{ij}$ , and  $m_{ij}$  are coefficients of single-point second-rank

tensors, just like stress and rigid-body mass moment of inertia, which is not typically so in the broader class of linear vibration model matrices. Thus, for the case of rotationally symmetric flow, these tensors are *isotropic*. This justifies that Equation 2.70 can be simplified to the following form for the *isotropic model*:

$$\begin{aligned} \begin{Bmatrix} f_x \\ f_y \end{Bmatrix} = & - \begin{bmatrix} k^s & k^{ss} \\ -k^{ss} & k^s \end{bmatrix} \begin{Bmatrix} x \\ y \end{Bmatrix} - \begin{bmatrix} c^s & c^{ss} \\ -c^{ss} & c^s \end{bmatrix} \begin{Bmatrix} \dot{x} \\ \dot{y} \end{Bmatrix} \\ & - \begin{bmatrix} m^s & m^{ss} \\ -m^{ss} & m^s \end{bmatrix} \begin{Bmatrix} \ddot{x} \\ \ddot{y} \end{Bmatrix} \end{aligned} \quad (2.85)$$

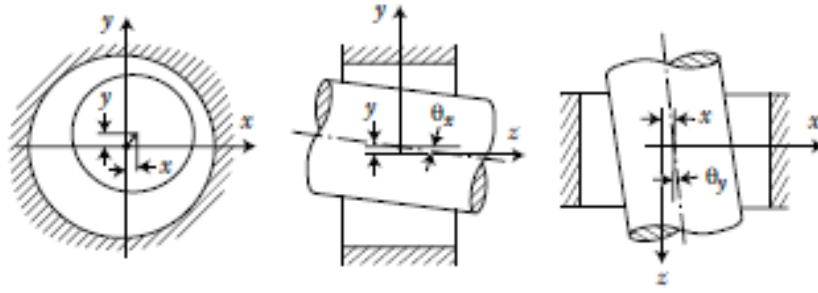


FIGURE 2.14 Radial bearing/seal radial and misalignment coordinates.

$\{x, y, \theta_x, \theta_y\}$  instead of only  $\{x, y\}$ . Consequently, the number of coefficients would increase by a factor of *four*, as shown in Equation 2.86 for such a model. Along practical lines of argument, optimum designs hopefully have minimal static and dynamic misalignment effects. While the definitive pronouncement on such effects may not have yet been rendered, other uncertainties such as from the manufacturing tolerances affecting journal-bearing clearance are more significant and prevalent (Chapter 5).

$$\begin{aligned}
 \begin{Bmatrix} f_x \\ f_y \\ M_x \\ M_y \end{Bmatrix} &= - \begin{bmatrix} k_{xx} & k_{xy} & k_{x\theta_x} & k_{x\theta_y} \\ k_{yx} & k_{yy} & k_{y\theta_x} & k_{y\theta_y} \\ k_{\theta_x x} & k_{\theta_x y} & k_{\theta_x \theta_x} & k_{\theta_x \theta_y} \\ k_{\theta_y x} & k_{\theta_y y} & k_{\theta_y \theta_x} & k_{\theta_y \theta_y} \end{bmatrix} \begin{Bmatrix} x \\ y \\ \theta_x \\ \theta_y \end{Bmatrix} \\
 &- \begin{bmatrix} c_{xx} & c_{xy} & c_{x\theta_x} & c_{x\theta_y} \\ c_{yx} & c_{yy} & c_{y\theta_x} & c_{y\theta_y} \\ c_{\theta_x x} & c_{\theta_x y} & c_{\theta_x \theta_x} & c_{\theta_x \theta_y} \\ c_{\theta_y x} & c_{\theta_y y} & c_{\theta_y \theta_x} & c_{\theta_y \theta_y} \end{bmatrix} \begin{Bmatrix} \dot{x} \\ \dot{y} \\ \dot{\theta}_x \\ \dot{\theta}_y \end{Bmatrix} \\
 &- \begin{bmatrix} m_{xx} & m_{xy} & m_{x\theta_x} & m_{x\theta_y} \\ m_{yx} & m_{yy} & m_{y\theta_x} & m_{y\theta_y} \\ m_{\theta_x x} & m_{\theta_x y} & m_{\theta_x \theta_x} & m_{\theta_x \theta_y} \\ m_{\theta_y x} & m_{\theta_y y} & m_{\theta_y \theta_x} & m_{\theta_y \theta_y} \end{bmatrix} \begin{Bmatrix} \ddot{x} \\ \ddot{y} \\ \ddot{\theta}_x \\ \ddot{\theta}_y \end{Bmatrix} \quad (2.86)
 \end{aligned}$$

### 2.5.1 Large Amplitude Vibration Sources that Yield Nonlinear Effects

Well-recognized operating conditions, albeit out of the ordinary, that cause large rotor-to-bearing vibration orbits include the following:

- *Very large rotor unbalance*, for example, sudden detachment loss of large turbine or fan blades at running speed.
- Rotor-bearing *self-excited* orbital vibration *limit cycles*.
- Explosive detonation (*shock*) near underwater naval vessels.
- Unbalance-driven resonance at an *inadequately damped critical speed*.
- Resonance build-up resulting from *earthquakes*.

When such large vibration-causing phenomena occur, the following additional rotor dynamic nonlinear phenomenon is likely to be produced in the process:

- Rotor-to-stator *rub-impacting*.

(d)



FIGURE 2.15 Continued.

bearings. In both of these cases, it is assumed that one-half of a complete last-stage turbine blade detaches at 3600 rpm. This is equivalent to a 100,000 pound corotational 3600 cpm rotating load imposed at the last-stage blade row where the lost blade piece is postulated to separate from the rotor. As a point of magnitude reference, this LP turbine rotor weighs approximately 85,000 pounds. The Figure 2.17 results show four orbit-like plots as follows:

- Journal-to-bearing orbit normalized by radial clearance
- Total bearing motion (see bearing pedestal model, Section 2.3.9.2)
- Total journal motion
- Total fluid-film force transmitted to bearing

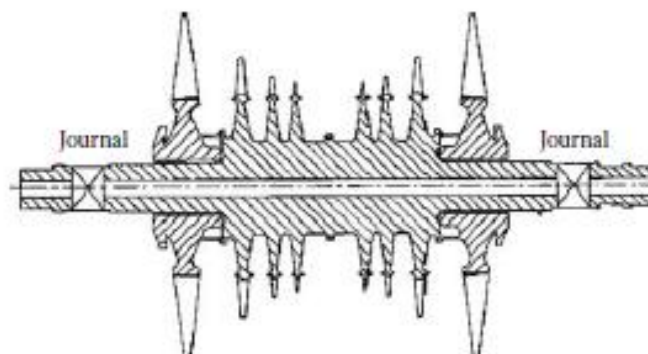
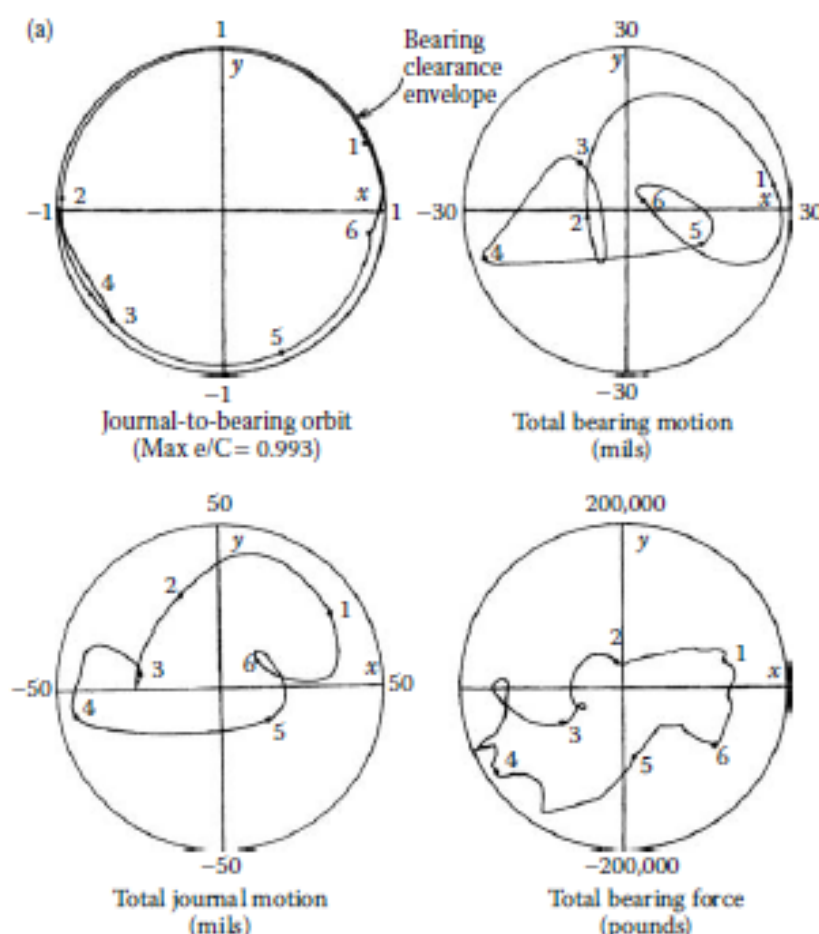


FIGURE 2.16 LP rotor portion of a 3600 rpm 700 MW steam turbine.



The normalized journal-to-bearing orbit is simply the journal motion minus the bearing motion divided by the bearing radial clearance. For the cylindrical journal bearing of the Figure 2.17a results, this clearance envelope is thus a circle of unity radius. In contrast, for the pivoted four-pad journal bearing of the Figure 2.17b results, the clearance envelope is a square of unity side. A prerequisite to presenting a detailed explanation of these results are the companion steady-state vibration and dynamic force amplitude results presented in Figure 2.18 for unbalance conditions from zero to 100,000 pounds imposed at the same last-stage blade row of the same nonlinear model.



**FIGURE 2.17** (a) Steady-state periodic response at bearing nearest the unbalance with force magnitude of 100,000 pounds, rotor supported on two identical fixed-arc journal bearings modeled after the actual rotor's two journal bearings. Timing marks at each one-half revolution, that is, 3 rev shown. (b) Steady-state periodic response at bearing nearest unbalance with force magnitude of 100,000 pounds, rotor supported on two identical four-pad pivoted-pad bearings with the gravity load directed between the bottom two pads. Bearings have same film diameter, length, and clearance as the actual fixed-arc bearings. Timings mark each one-half revolution, that is, 3 rev shown.



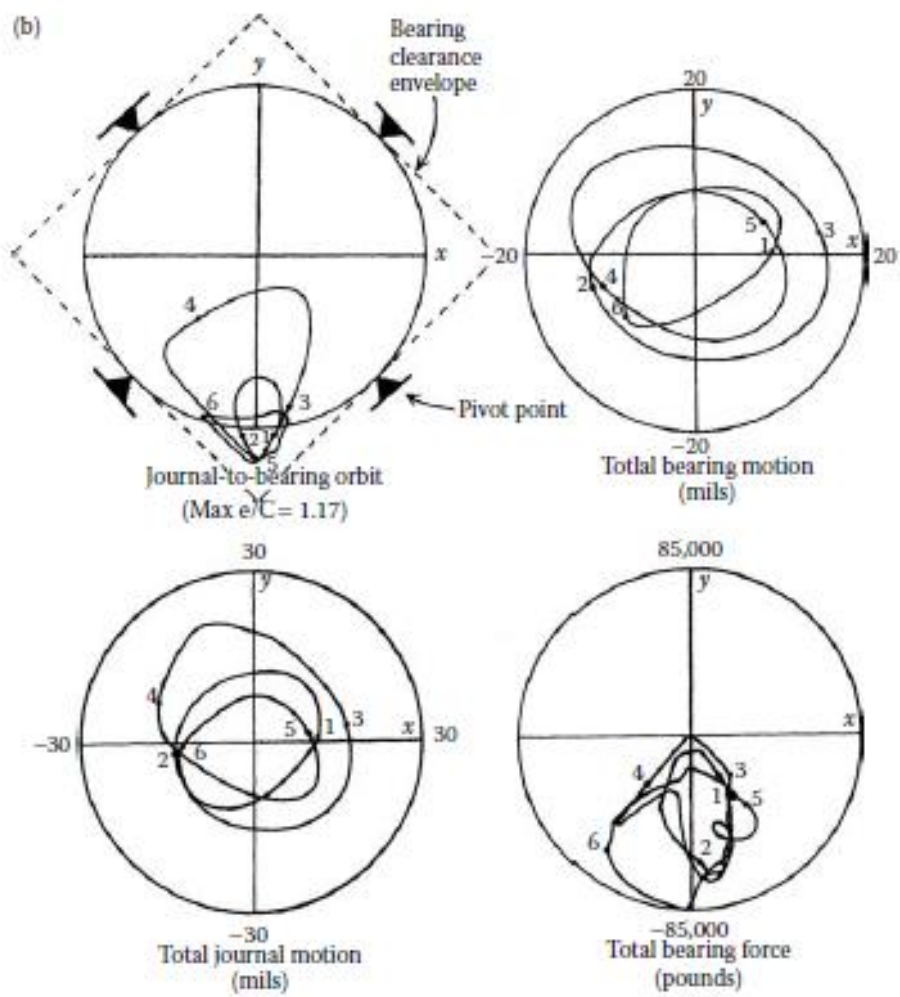
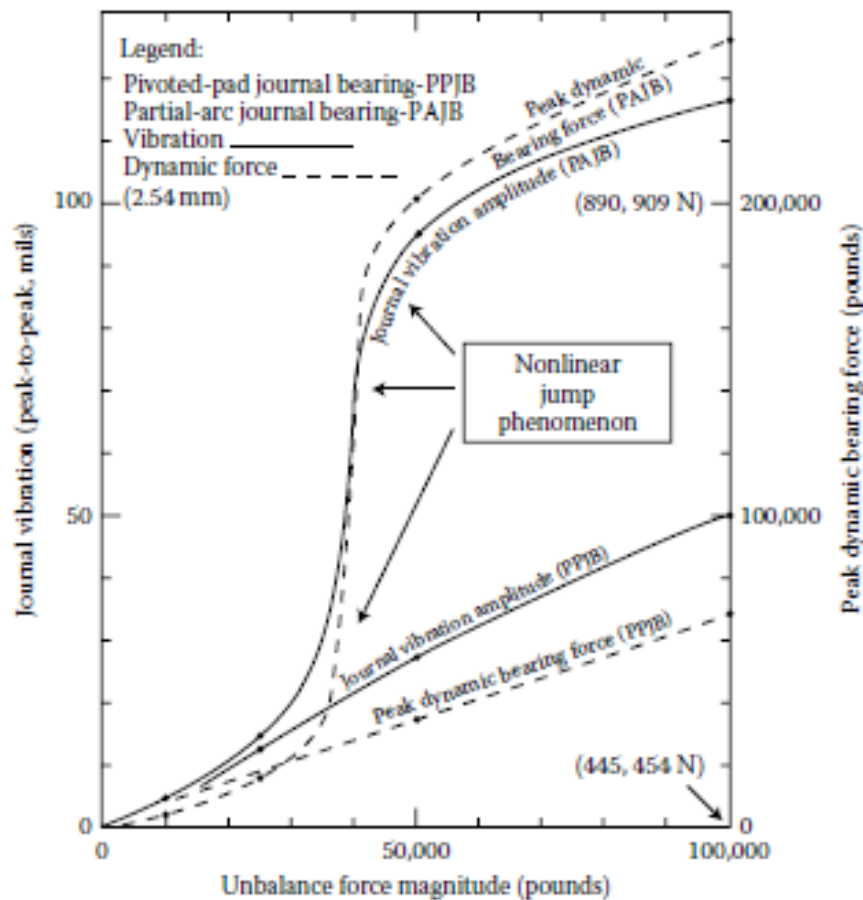
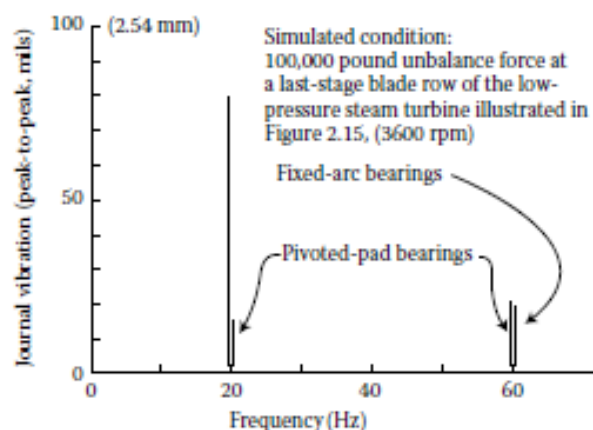


FIGURE 2.17 Continued.



**FIGURE 2.18** Comparison between partial-arc and pivoted-pad journal-bearing vibration control capabilities under large unbalance operating conditions of an LP steam turbine rotor at 3600 rpm; steady-state journal motion and transmitted peak dynamic bearing force over a range of unbalance magnitudes (data points mark computed simulation cases).



**FIGURE 2.19** Fast Fourier transform of peak-to-peak journal vibration displacement amplitudes.

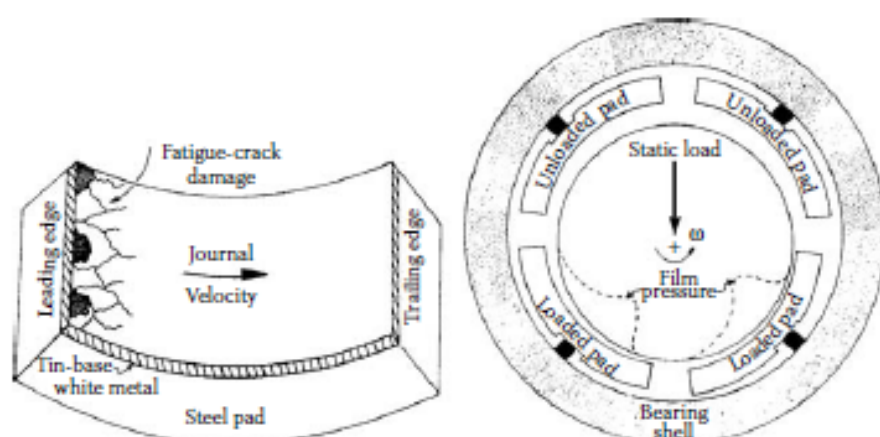


FIGURE 2.20 Four-pad tilting-pad bearing with unloaded pads.

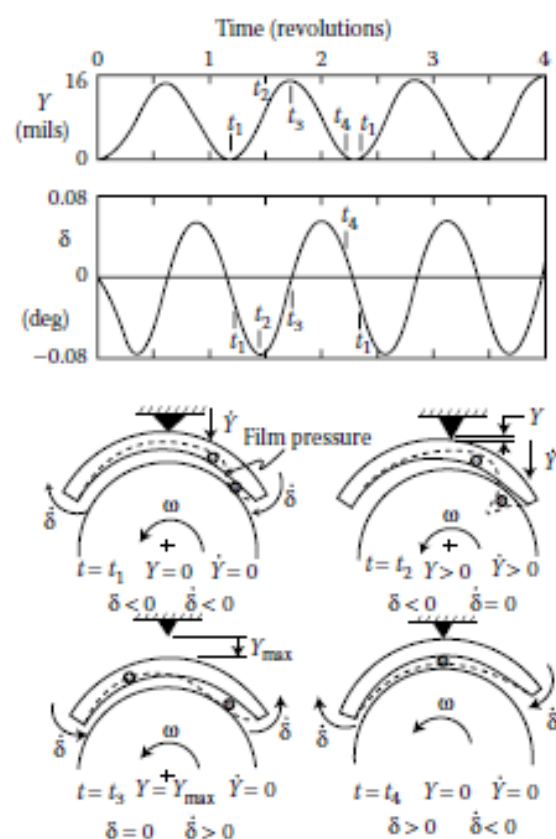


FIGURE 2.21 Simulation results of unloaded pad self-excited vibration.

## 2.5.4 Journal-Bearing Hysteresis Loop

The hysteresis loop associated with the journal bearing caused dynamic instability self-excited vibration mechanism called *oil whip* was for a long time an interesting topic for the academics. But it did not attract the close scrutiny of rotating machinery development engineers. However, in the seismically active region of Japan, a team headed by Professor Y. Hori at the University of Tokyo brought the practical importance of the journal-bearing hysteresis loop to the wider engineering community. In the paper by Hori and Kato (1990), the distinct possibility of an earthquake-initiated high-amplitude sustained self-excited rotor vibration is addressed. That work helped initiate subsequent research by the author and his team, reported in the paper by Adams et al. (1996). A generic illustration of their journal-bearing hysteresis loop and computational model are shown in Figure 2.22.

Figure 2.22 encapsulates the imbedding of the classical oil-whip phenomenon within an expanded view that shows two stable vibration solutions at speeds below the oil-whip threshold speed  $\omega_{th}$  (Hopf bifurcation) and one unstable solution, which is a boundary between the two

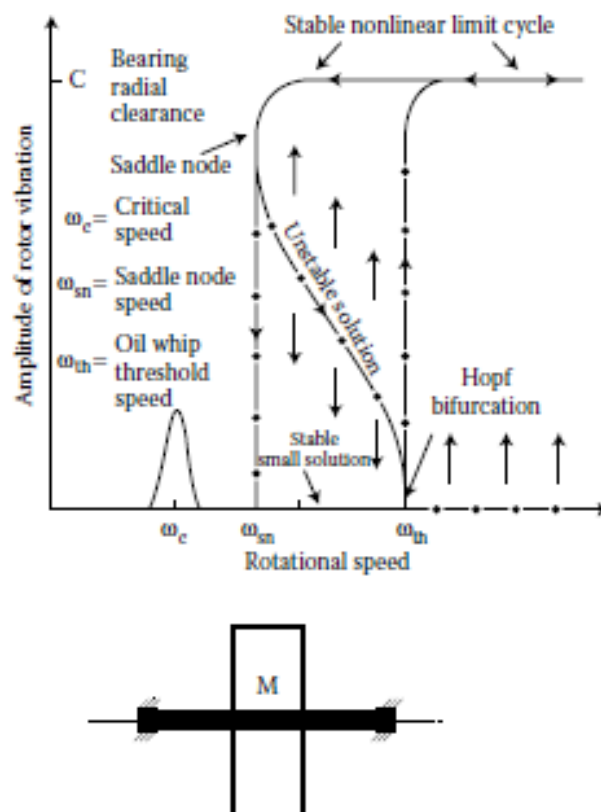


FIGURE 2.22 Journal-bearing hysteresis-loop and rotor-bearing model.

### 2.5.5 Shaft-on-Bearing Impacting

Impacting is a quite nonlinear dynamic phenomenon. In Chapter 9 Section 9.8.3, *rotor-stator rub-impacting* is treated from the point of view as a cause of excessive rotor vibration, and its identifying symptoms are treated. In order to computationally model rotor-bearing impact conditions, there is the need for an *impact restitution coefficient*, a necessary input

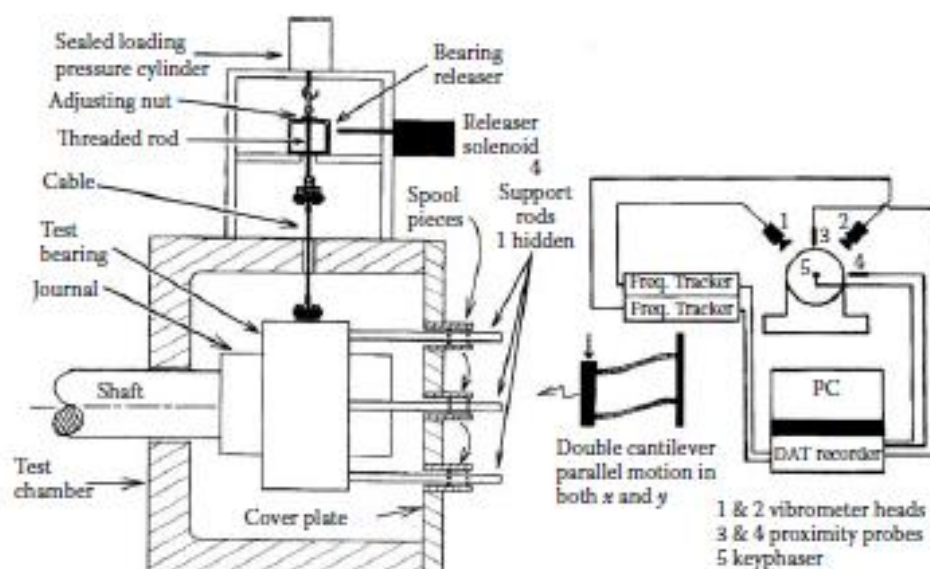


FIGURE 2.23 Test for rotor-bearing restitution coefficient measurement.



### 3.2 Rotor-Based Spinning Reference Frames

To properly visualize TRV, one must consider that the relatively small torsion-twisting angular velocities of TRV are superimposed on the considerably larger rotor spin velocity. That is, the TRV angular displacements, velocities, and accelerations are referenced to a *rotating* (noninertial) *reference frame* that rotates at the spin velocity. However, TRV equations of motion are generally derived as though the coordinate system is not rotating. The reason this produces proper motion equations warrants a fundamental explanation. As developed in Chapter 2, the rate-of-change of a rigid body's angular momentum vector, prescribed in a coordinate system rotating at  $\vec{\Omega}$ , is given by Equation 2.15. The same form of equation applies to time differentiation of any vector prescribed in a rotating reference frame. The instantaneous total angular velocity ( $\vec{\theta}_i^T$ ) at a rotor mass station is the sum of the instantaneous TRV velocity ( $\vec{\theta}_i$ ) and the instantaneous rotor spin velocity ( $\vec{\omega}$ ), shown as follows:

$$\vec{\theta}_i^T = \vec{\theta}_i + \vec{\omega} \quad (3.1)$$

Thus, the inertial angular acceleration at a rotor station is as follows:

$$\ddot{\theta}_i^T = \ddot{\theta}_i + \dot{\omega} = (\ddot{\theta}_i)_\omega + \vec{\omega} \times \vec{\theta}_i + \dot{\omega} \quad (3.2)$$

The spin and TRV velocity vectors are coaxial; thus their cross product is zero, as indicated in Equation 3.2. Furthermore, for most TRV analysis purposes, rotor spin acceleration ( $\dot{\omega}$ ) is taken as zero, that is,  $\omega \cong \text{constant}$ , so  $\ddot{\theta}_i^T = \ddot{\theta}_i$ . Inertial angular acceleration vectors for TRV can then be given as follows:

$$\ddot{\theta}_i = (\ddot{\theta}_i)_\omega \quad (3.3)$$

That TRV equations of motion are derived as though the rotor is not spinning about its axis is thus shown to be valid.



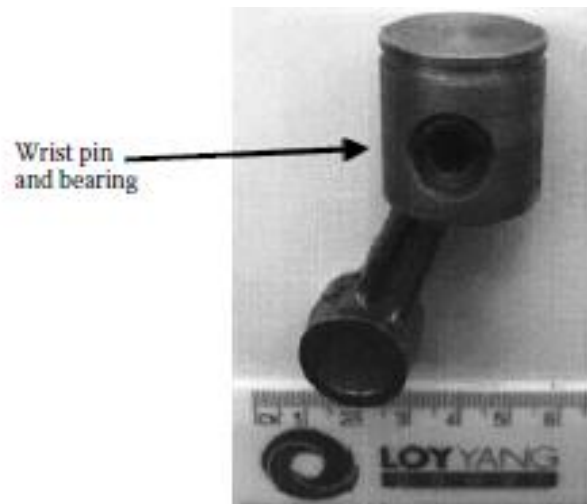


FIGURE 2.25 (See color insert following page 262.) Piston and connecting rod of a small reciprocating compressor.

That the refrigerator compressor failure rate was 4 times that of the air conditioner compressor mystified the manufacturer's top compressor engineers, because the wrist pin peak load in the air conditioner was approximately 25% higher than in the refrigerator. The wrist pin bearing radial load versus crank angle is illustrated for both applications in Figure 2.26. In an attempt to uncover the root cause for the relatively large warranty failure rate in the refrigerator application, many different analyses and tests were conducted, sort of a "fishing expedition."

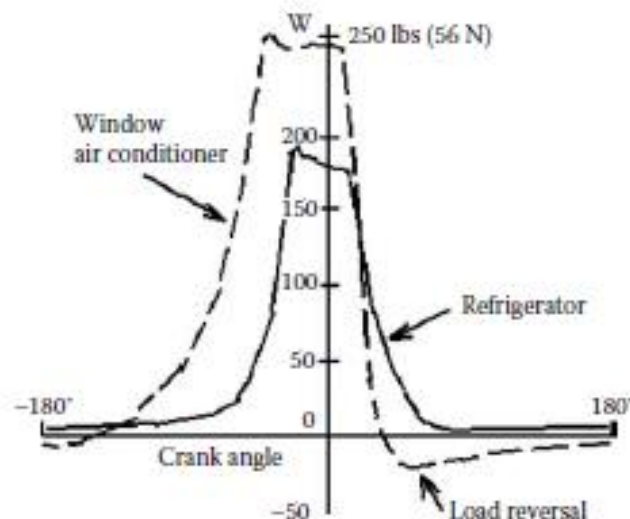


FIGURE 2.26 Wrist pin bearing load ( $W$ ) curves versus crank angle.

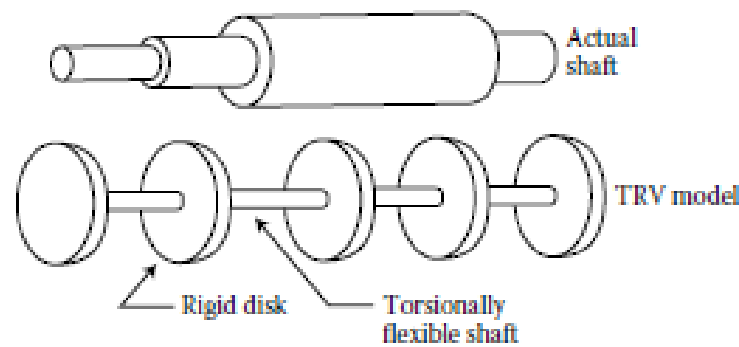


FIGURE 3.1 Multielement TRV model for a single-shaft rotor.

### 3.3.1.1 Lumped Mass Matrix

In this approach, it is assumed that for each uniform-diameter shaft element, half its polar moment of inertia,  $I^{(s)}$ , is lumped at each of the

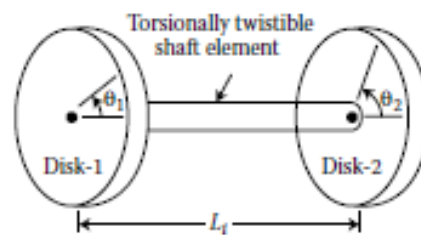


FIGURE 3.2 Rotor torsional finite-element 2-DOF building block.

element's two end points (stations). Implicit in this approximation is an incremental step change in angular acceleration for each shaft element at its axial midpoint. That is, the continuous axial variation in angular acceleration is approximated by a series of small discrete step changes. A concentrated (nonstructural) polar moment of inertia,  $I^{(d)}$ , may be optionally added at any rotor station as appropriate to model gears, couplings, impellers, turbine disks, pulleys, flywheels, thrust-bearing collars, nonstiffening motor and generator rotor components, and so on. The complete *single-rotor ("sr") lumped ("l") mass matrix* is thus a diagonal matrix, given as follows:

$$[M]_{sr}^I =$$

$$\begin{bmatrix} \frac{1}{2}I_1^{(s)} + I_1^{(d)} & & & & \\ & \frac{1}{2}(I_1^{(s)} + I_2^{(s)}) + I_2^{(d)} & & & \\ & & \ddots & & \\ & & & \frac{1}{2}(I_{i-1}^{(s)} + I_i^{(s)}) + I_i^{(d)} & \\ & & & & \ddots \\ & & & & & \frac{1}{2}I_{N-1}^{(s)} + I_N^{(d)} \end{bmatrix}_{N \times N} \quad (3.4)$$

$N$  = No. of rotor stations = No. of DOFs = No. of elements + 1.  
 Subscript on  $I^{(s)}$  = Element Number, Subscript on  $I^{(d)}$  = Station Number.

### 3.3.1.2 Distributed Mass Matrix

As similarly explained in Section 2.3 for LRV models, the underlying assumption here is that the angular acceleration of each shaft element about its axis varies linearly over its own length. Therefore, model resolution accuracy is better with the *distributed mass* formulation than with the *lumped mass* formulation. The better the model resolution accuracy, the fewer the number of finite elements (or DOFs) needed to accurately characterize the relevant modes of the actual continuous media system using a discrete model. Consistent with the assumption that angular acceleration varies linearly between rotor stations, the angular velocity then also must vary linearly between rotor stations. The instantaneous TRV kinetic energy stored in the  $i$ th single shaft element can be formulated from the integration of kinetic energy distributed over the  $i$ th element's length, similar to Equation 2.39 for LRV radial velocity components,

as follows:

$$T_i^{(s)} = \frac{1}{2} \frac{I_i^{(s)}}{L_i} \int_0^{L_i} (\dot{\theta} + \omega)^2 dz \quad (3.5)$$

Substituting a linearly varying  $\dot{\theta}$  and  $\omega \equiv \text{constant}$  into Equation 3.5 yields the  $i$ th shaft element's torsional kinetic energy terms associated with the  $\theta_i$  and  $\theta_{i+1}$  Lagrange equations for the  $i$ th and  $(i+1)$  rotor stations. This yields the following results, consistent with Equation 3.2 (i.e.,  $\omega \equiv \text{constant}$ ,  $\therefore \dot{\omega} = 0$ ).

$$\begin{aligned} \frac{d}{dt} \left( \frac{\partial T}{\partial \dot{\theta}_i} \right) &= \frac{1}{3} I_i^{(s)} \ddot{\theta}_i + \frac{1}{6} I_i^{(s)} \ddot{\theta}_{i+1} \\ \frac{d}{dt} \left( \frac{\partial T}{\partial \dot{\theta}_{i+1}} \right) &= \frac{1}{6} I_i^{(s)} \ddot{\theta}_i + \frac{1}{3} I_i^{(s)} \ddot{\theta}_{i+1} \end{aligned} \quad (3.6)$$

The complete *single-rotor distributed mass matrix* is thus a tridiagonal matrix, as follows. Note the optional  $I^{(d)}$  at each station, just as in Equation 3.4.

*Polar moment-of-inertia formulas for shaft elements and concentrated disks are the same as given at the beginning of Section 2.3 for LRV models.*

### 3.3.2 Stiffness Matrix

The TRV stiffness matrix  $[K]_{ff}$  for a *free-free* single rotor, such as shown in Figure 3.1, is quite simple to formulate. It is the torsional equivalent of the type of translational system shown in Figure 1.8. That is, each rotor mass station has elastic coupling only to its immediate neighbors. Therefore, the single-rotor TRV stiffness matrix, shown as follows, is tridiagonal just as shown for the system in Figure 1.8.

$$[M]_{ff}^{(d)} =$$

$$\begin{bmatrix} \frac{1}{3} I_1^{(s)} + I_1^{(d)} & \frac{1}{6} I_1^{(s)} & & & & \\ \frac{1}{6} I_1^{(s)} & \frac{1}{3} (I_1^{(s)} + I_2^{(s)}) + I_2^{(d)} & \frac{1}{6} I_2^{(s)} & & & \\ & \ddots & \ddots & \ddots & \ddots & \\ & & \frac{1}{6} I_{i-1}^{(s)} & \frac{1}{3} (I_{i-1}^{(s)} + I_i^{(s)}) + I_i^{(d)} & \frac{1}{6} I_i^{(s)} & \\ & & & \ddots & \ddots & \ddots \\ & & & & \frac{1}{6} I_{N-2}^{(s)} & \frac{1}{3} I_{N-2}^{(s)} + I_N^{(d)} \end{bmatrix}_{N \times N} \quad (3.7)$$

$$[K]_{ff} =$$

$$\begin{bmatrix} K_1 & -K_1 & & & & \\ -K_1 & K_1 + K_2 & -K_2 & & & \\ & \ddots & \ddots & \ddots & & \\ & & -K_i & K_i + K_{i+1} & -K_{i+1} & \\ & & & \ddots & \ddots & \\ & & & & -K_{N-2} & K_{N-2} + K_{N-1} & -K_{N-1} \\ & & & & & -K_{N-1} & K_{N-1} \end{bmatrix}_{N \times N} \quad (3.8)$$

Subscript on  $K$  = Element Number.  
Shaft element torsional stiffness:

$$K = \frac{\pi(d_o^4 - d_i^4)G}{32L}$$

$$[K]_c = \begin{bmatrix} K_1^{(c)} & & & & \\ & K_2^{(c)} & & & \\ & & \ddots & & \\ & & & K_i^{(c)} & \\ & & & & \ddots & \\ & & & & & K_{N-1}^{(c)} & \\ & & & & & & K_N^{(c)} \end{bmatrix}$$

$$[K]_{ss} = [K]_{ff} + [K]_c \quad (3.9)$$

Equations of motion for the undamped single-rotor model are then as follows:

$$[M]_{ss}\ddot{\theta} + [K]_{ss}\theta = \{m(t)\} \quad (3.10)$$

Here,  $\{m(t)\}$  contains any *externally applied* time-dependent torque components, such as to model synchronous generators or turbo-generators during severe electrical disturbances like *high-speed reclosure* (HSR) of circuit breakers after fault clearing of transmission lines leaving power stations. Of course, to compute the undamped natural frequencies and corresponding mode shapes, only the mass and stiffness matrices are utilized.

### 3.4 Coupled Rotors

The single-rotor mass and stiffness matrices developed in the previous section form the basic model building blocks for TRV coupled-rotor models. One of the many advantages of assembling the equations of motion in matrix form is the ease with which modeled substructures can be joined to assemble the complete equations of motion of a multisubstructure system.

*Coupled rotor model configurations are the simplest TRV*



- Coupled rotors may have *speed ratios* other than 1:1.
- Torsional coupling may be either *rigid* (e.g., gears) or *flexible* (e.g., belt).
- System may be *branched* instead of *unbranched*.

An understanding of these complexities can be obtained by following the formulation details of their TRV model constructions, which are presented subsequently in this section. The handling of these complexities is simplified by the fact that correct TRV equations of motion can be derived as though the rotors are not spinning, as shown in Section 3.2, Equation 3.3, that is, modeled as though the coupled-rotor machine is not running.

### 3.4.1 Coaxial Same-Speed Coupled Rotors

This is a quite common configuration category and the most typical case involves two single rotors joined by a so-called *flexible coupling*. Assembling the mass and stiffness matrices for this case is quite simple, as shown by the following equations. The total mass matrix can be expressed as follows:

$$[M] = \begin{bmatrix} [M_1]_{sr} & [0] \\ [0] & [M_2]_{sr} \end{bmatrix} \quad (3.11)$$

Usually, a flexible coupling can be adequately modeled by two concentrated polar moment-of-inertias connected by a torsional spring stiffness. The two concentrated coupling inertias  $I_1^{(c)}$  and  $I_2^{(c)}$  are added as concentrated inertias to the last diagonal element of  $[M_1]_{sr}$  and the first diagonal element of  $[M_2]_{sr}$ , respectively. To assemble the total stiffness matrix, the equivalent torsional spring stiffness  $K^{(c)}$  of the coupling is used to join the respective single-rotor stiffness matrices of the two rotors, as follows:

$$[K] = \begin{bmatrix} [K_1]_{sr} & [0] \\ [0] & [K_2]_{sr} \end{bmatrix} + [K_c]_{2 \times 2} = \begin{bmatrix} \begin{bmatrix} K_{ij}^{(1)} & \\ & K^{(c)} \\ & -K^{(c)} \end{bmatrix} & \begin{bmatrix} \bigcirc & \\ -K^{(c)} & \\ K^{(c)} & \end{bmatrix}_{2 \times 2} \\ \begin{bmatrix} \bigcirc & \\ & K_{ij}^{(2)} \end{bmatrix} & \end{bmatrix} \quad (3.12)$$

The complete equations of motion for two coaxially coupled rotors are then expressible in the same matrix format as Equation 3.10, that is,  $[M]\{\ddot{\theta}\} + [K]\{\theta\} = \{M(t)\}$ . For three or more simply connected same-speed flexible-coupled rotors, the above process is taken to its natural extension.



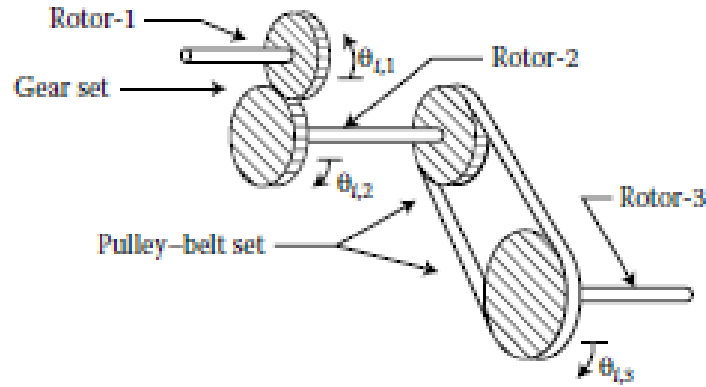


FIGURE 3.3 Unbranched three-rotor system with a gear set and a pulley-belt set.

### 3.4.2.1 Rigid Connections

The gear set of the system in Figure 3.3 will be assumed to be torsionally much stiffer than other torsional flexibilities of the system, and thus taken as perfectly *rigid*. The TRV angular displacements of the two gears are then constrained to have the same ratio as the nominal speed ratio of the two-gear set. Thus, one equation of motion must be eliminated either from rotor-1 (last station) or rotor-2 (first station). Here the equation of motion for the first station of rotor-2 is absorbed into the equation of motion for last station of rotor-1. The concentrated inertia of the rotor-2 gear is thus transferred to the rotor-1 station with the mating gear. Defining  $n_{21}$  as the speed ratio of rotor-2 to rotor-1, and  $\theta_{ij}$  as  $i$ th angular coordinate of the  $j$ th rotor, the TRV angular coordinate of the rotor-2 gear is expressed in terms of the rotor-1 gear's coordinate, as follows. Note the opposite positive sense for  $\theta_{i,2}$ , Figure 3.3.

$$\theta_{1,2} = n_{21}\theta_{N_1,1} \quad (3.13)$$

where  $N_1$  = number of stations on rotor-1 = station number rotor-1's last station.

The TRV kinetic energy of the two rigidly coupled gears is thus expressible as follows:

$$T_{12}^{\text{gears}} = \frac{1}{2}I_{N_1,1}^{(d)}\dot{\theta}_{N_1,1}^2 + \frac{1}{2}I_{1,2}^{(d)}\dot{\theta}_{1,2}^2 = \frac{1}{2}\left(I_{N_1,1}^{(d)} + n_{21}^2 I_{1,2}^{(d)}\right)\dot{\theta}_{N_1,1}^2 \quad (3.14)$$

where  $I_{ij}^{(d)} \equiv$  nonstructural concentrated inertia for the  $i$ th station of the  $j$ th rotor.

The combined TRV nonstructural inertia of the two gears is thus lumped in the motion equation for station  $N_1$  of rotor-1 as follows:

$$\frac{d}{dt}\left(\frac{\partial T_{12}^{\text{gears}}}{\partial \dot{\theta}_{N_1,1}}\right) = \left(I_{N_1,1}^{(d)} + n_{21}^2 I_{1,2}^{(d)}\right)\ddot{\theta}_{N_1,1} \quad (3.15)$$

That is, postulating a linear variation of angular velocity along the shaft element, and substituting from Equation 3.13 for  $\theta_{1,2}$ , yields the following equation for the TRV kinetic energy of shaft element-1 of rotor-2.

$$T_{1,2}^{(s)} = \frac{I_{1,2}^{(s)}}{6} \left( n_{21}^2 \dot{\theta}_{N_1,1}^2 + n_{21} \dot{\theta}_{N_1,1} \dot{\theta}_{2,2} + \dot{\theta}_{2,2}^2 \right) \quad (3.16)$$

The following equation-of-motion *distributed mass* inertia contributions of this shaft element to the stations that bound it are accordingly obtained:

$$\begin{aligned} \frac{d}{dt} \left( \frac{\partial T_{1,2}^{(s)}}{\partial \dot{\theta}_{N_1,1}} \right) &= \frac{1}{3} n_{21}^2 I_{1,2}^{(s)} \ddot{\theta}_{N_1,1} + \frac{1}{6} n_{21} I_{1,2}^{(s)} \ddot{\theta}_{2,2} \\ \frac{d}{dt} \left( \frac{\partial T_{1,2}^{(s)}}{\partial \dot{\theta}_{2,2}} \right) &= \frac{1}{6} n_{21} I_{1,2}^{(s)} \ddot{\theta}_{N_1,1} + \frac{1}{3} I_{1,2}^{(s)} \ddot{\theta}_{2,2} \end{aligned} \quad (3.17)$$

where  $I_{ij}^{(s)} \equiv$  structural inertia for the  $i$ th shaft element of the  $j$ th rotor.

Postulating a *rigid connection* between the two gears in Figure 3.3 eliminates one DOF (i.e., the first station of rotor-2). The corresponding detailed formulations needed to merge the rotor-1 and rotor-2 mass matrices are contained in Equations 3.13 through 3.17. Merging the rotor-1 and rotor-2 stiffness matrices must also incorporate the same elimination of one DOF. Specifically, shaft element-1 of rotor-2 becomes a direct torsional stiffness between the last station of rotor-1 and the second station of rotor-2. This stiffness connection is almost as though these two stations were adjacent to each other on the same rotor, except for the speed-ratio effect. The easiest way to formulate the details for merging rotor-1 and rotor-2 stiffness matrices is to use the potential energy term of the Lagrange formulation for the equations of motion, as follows (see Equation 2.50):

$$V_{1,2} = \frac{1}{2} K_{1,2} (\theta_{1,2} - \theta_{2,2})^2 \quad (3.18)$$

where  $V_{ij} \equiv$  TRV potential energy stored in  $i$ th shaft element of the  $j$ th rotor and  $K_{ij} \equiv$  Torsional stiffness of the  $i$ th shaft element of the  $j$ th rotor.

Substituting from Equation 3.13 for  $\theta_{1,2}$  into Equation 3.18 thus leads to the following terms for merging rotor-1 and rotor-2 stiffness matrices:

$$\begin{aligned} \frac{\partial V_{1,2}}{\partial \theta_{N_1,1}} &= K_{1,2} (n_{21}^2 \theta_{N_1,1} - n_{21} \theta_{2,2}) \\ \frac{\partial V_{1,2}}{\partial \theta_{2,2}} &= K_{1,2} (-n_{21} \theta_{N_1,1} + \theta_{2,2}) \end{aligned} \quad (3.19)$$

### 3.4.2.2 Flexible Connections

The pulley–belt set in Figure 3.3 connecting rotor-2 to rotor-3 is assumed to be a *flexible connection* and thus no DOF is eliminated, contrary to the *rigid connection* case. A flexible connection does not entail modifications to the mass matrix of either of the two flexibly connected rotors. Only the stiffness of the belt must be added to the formulation to model the flexible connection. It is assumed that both straight spans of the belt connecting the two pulleys are in tension, and thus both spans are assumed to have the same tensile stiffness,  $k_b$ , and their TRV stiffness effects are additive like two springs in parallel. The easiest way to formulate the merging rotor-2 and rotor-3 stiffness matrices is to use the potential energy term of the Lagrange formulation, as shown in Equation 2.50. To model *gear-set flexibility*, replace  $2k_b$  with pitch-line  $k_g$  and define  $R_j$  as  $j$ th pitch radius, not  $j$ th pulley radius.

$$\begin{aligned} V_b &= \frac{1}{2}(2k_b)(\theta_{N_2,2}R_2 - \theta_{1,3}R_3)^2 \\ &= k_b(\theta_{N_2,2}^2R_2^2 - 2\theta_{N_2,2}\theta_{1,3}R_2R_3 + \theta_{1,3}^2R_3^2) \end{aligned} \quad (3.20)$$

$$\begin{aligned} \frac{\partial V_b}{\partial \theta_{N_2,2}} &= 2k_b(\theta_{N_2,2}R_2^2 - \theta_{1,3}R_2R_3) \\ \frac{\partial V_b}{\partial \theta_{1,3}} &= 2k_b(-\theta_{N_2,2}R_2R_3 + \theta_{1,3}R_3^2) \end{aligned} \quad (3.21)$$

where  $R_j \equiv$  pulley radius for the  $j$ th rotor,  $V_b \equiv$  TRV potential energy in belt and  $N_2 =$  Number of stations on rotor-2 = Station number rotor-2's last station.

At this point, all components needed to write the equations of motion for the TRV system in Figure 3.3 are ready for implementation.

Equation 3.8. At this point, constructing the total system mass and stiffness matrices only entails catenating the single-rotor matrices and implementing the already developed modifications to the matrices dictated by the rigid and flexible connections. Employing modifications extracted from Equations 3.15 and 3.17,  $[M_1]$  is augmented as follows. Superscript “rc” refers to *rigid connection*.

$$[M_1^*] = [M_1] + [M_1^{rc}], \text{ where } [M_1^{rc}] = \begin{bmatrix} \bigcirc & \bigcirc \\ 0 & n_{21}^2 I_{1,2}^{(d)} + \frac{1}{3} n_{21}^2 I_{1,2}^{(s)} \end{bmatrix}_{N_1 \times N_1} \quad (3.22)$$

All elements in  $[M_1^{rc}]$  are  
zero except element  $(N_1, N_1)$ .

Eliminating its first row and first column,  $[M_2]$  is reduced to  $[M_2^*]$ . The complete system mass matrix can be assembled at this point, catenating  $[M_1^*]$ ,  $[M_2^*]$ , and  $[M_3^*]$ , and adding the cross-coupling terms contained in Equation 3.17, as follows:

$$[M] = \begin{bmatrix} [M_1^*]_{M_{cc}} & & \\ & M_{cc}[M_2^*] & \\ & & [M_3^*] \end{bmatrix}_{N \times N} \quad (3.23)$$

Subscript “cc” refers to *cross-coupling*.

$$M_{N_1, N_1+1} = M_{N_1+1, N_1} = \frac{1}{6} n_{21} I_{1,2}^{(s)} \equiv M_{cc}, \quad N = N_1 + (N_2 - 1) + N_3$$

The complete system stiffness matrix  $[K]$  is similarly constructed. Employing modifications extracted from Equation 3.19,  $[K_1]$  is augmented as follows:

$$[K_1^*] = [K_1] + [K_1^{rc}], \text{ where } [K_1^{rc}] = \begin{bmatrix} \bigcirc & \bigcirc \\ 0 & n_{21}^2 K_{1,2} \end{bmatrix}_{N_1 \times N_1} \quad (3.24)$$

All elements in  $[K_1^{rc}]$  are  
zero except element  $(N_1, N_1)$ .

Eliminating its first row and first column,  $[K_2]$  is reduced to  $[K_2^*]$ , which is augmented to form  $[K_2^*]$  as follows. Superscript “fc” refers to *flexible connection*.

$$[K_2^*] = [K_2^*] + [K_2^{fc}], \text{ where } [K_2^{fc}] = \begin{bmatrix} \bigcirc & \bigcirc \\ 0 & 2k_b R_2^2 \end{bmatrix}_{N_2 \times N_2} \quad (3.25)$$

All elements in  $[K_2^{fc}]$  are  
zero except element  $(N_2^*, N_2^*)$ .

$$N_2^* = N_2 - 1$$

$[K_3]$  is augmented to form  $[K_3^*]$  as follows.

$$[K_3^*] = [K_3] + [K_3^{kc}], \text{ where } [K_3^{kc}] = \begin{bmatrix} 2k_b R_3^2 & 0 \\ \text{O} & \text{O} \end{bmatrix}_{N_2 \times N_2} \quad (3.26)$$

All elements in  $[K_3^{kc}]$  are zero except element (1,1).

The complete system stiffness matrix can be assembled at this point, concatenating  $[K_1^*]$ ,  $[K_2^*]$ , and  $[K_3^*]$ , and adding the cross-coupling terms contained in Equations 3.19 and 3.21, as follows:

$$[K] = \begin{bmatrix} \begin{bmatrix} K_1^* \end{bmatrix} & & \\ & K_{cc}^{1,2} \begin{bmatrix} K_2^* \end{bmatrix} & \\ & & K_{cc}^{2,3} \begin{bmatrix} K_3^* \end{bmatrix} \end{bmatrix}_{N \times N} \quad (3.27)$$

$$K_{cc}^{1,2} \equiv -n_{21} K_{1,2}; \text{ extracted from Equation 3.19}$$

$$K_{cc}^{2,3} \equiv -2k_b R_2 R_3; \text{ extracted from Equation 3.21}$$

The complete TRV equations of motion for the Figure 3.3 system are thus expressible in the same matrix format as Equation 3.10, that is,  $[M]\{\ddot{\theta}\} + [K]\{\theta\} = \{m(t)\}$ . The  $[M]$  and  $[K]$  matrices here are tridiagonal, which is consistent with the designation of *unbranched*. The formulations developed here are readily applicable to any *unbranched* TRV system of coupled rotors.



### 3.4.3 Branched Systems with Rigid and Flexible Connections

The system shown in Figure 3.4 bears a close similarity to the system in Figure 3.3, except that its gear set and pulley set are located inboard of their respective rotor ends, each of these connections thus making it a *branched* system. Its  $[M]$  and  $[K]$  matrices are therefore not tridiagonal, as now shown.

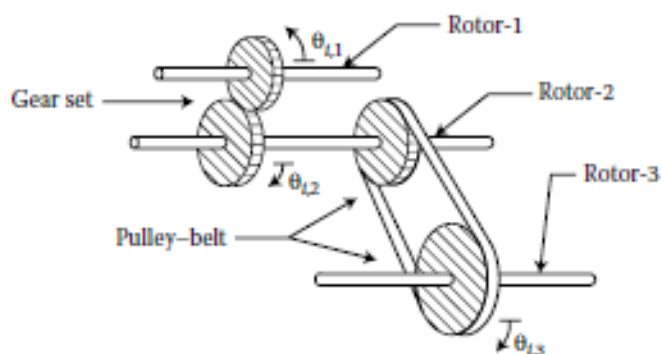


FIGURE 3.4 Branched three-rotor system with a gear set and a pulley-belt set.

Constructing mass and stiffness matrices for the Figure 3.4 system follows the same procedures of the previous subsection for *unbranched* systems. For the individual rotors, the *distributed mass* approach is again used, applying Equation 3.7 for construction of the single-rotor mass matrices,  $[M_1]$ ,  $[M_2]$ , and  $[M_3]$ . Also, Equation 3.9 is again used to construct the single-rotor stiffness matrices  $[K_1]$ ,  $[K_2]$ , and  $[K_3]$ , adding any *to-ground* flexible connections to the *free-free* TRV stiffness matrices from Equation 3.8. Using the standard substructuring approach previously applied here to *unbranched* systems, constructing the  $[M]$  and  $[K]$  matrices for the Figure 3.4 system is only slightly more involved than for the Figure 3.3 system.



### 3.4.3.1 Rigid Connections

The two gears joining rotor-1 to rotor-2 are assumed here to be a perfectly rigid torsional connection between the two rotors. Accordingly, the equation of motion for the rotor-2 gear station ( $N_{G2}$ ) is absorbed into the equation of motion for the rotor-1 gear station ( $N_{G1}$ ), with the eliminated rotor-2 gear DOF ( $\theta_{N_{G2},2}$ ) expressed by the constant speed ratio ( $n_{21}$ ) times the rotor-1 gear coordinate ( $\theta_{N_{G1},1}$ ), as follows ( $n_{21} \equiv \omega_2/\omega_1$ ).

$$\theta_{N_{G2},2} = n_{21} \theta_{N_{G1},1} \quad (3.28)$$

Similar to Equation 3.14, the TRV kinetic energy of the two rigidly coupled gears is thus expressible as follows:

$$T_{12}^{\text{gears}} = \frac{1}{2} I_{N_{G1},1}^{(d)} \dot{\theta}_{N_{G1},1}^2 + \frac{1}{2} I_{N_{G2},2}^{(d)} \dot{\theta}_{N_{G2},2}^2 = \frac{1}{2} \left( I_{N_{G1},1}^{(d)} + n_{21}^2 I_{N_{G2},2}^{(d)} \right) \dot{\theta}_{N_{G1},1}^2 \quad (3.29)$$

The combined TRV nonstructural inertia of the two gears is thus lumped in the motion equation for station  $N_{G1}$  of rotor-1 as follows:

$$\frac{d}{dt} \left( \frac{\partial T_{12}^{\text{gears}}}{\partial \dot{\theta}_{N_{G1},1}} \right) = \left( I_{N_{G1},1}^{(d)} + n_{21}^2 I_{N_{G2},2}^{(d)} \right) \ddot{\theta}_{N_{G1},1} \quad (3.30)$$

Using the *distributed mass* approach, the TRV kinetic energy of the rotor-2 shaft element just to the left of rotor-2's station  $N_{G2}$  and of the element just to the right of station  $N_{G2}$  are derived to be the following, similar to Equation 3.16:

$$\begin{aligned} T_{N_{G2}-1,2}^{(s)} &= \frac{I_{N_{G2}-1,2}^{(s)}}{6} \left( n_{21}^2 \dot{\theta}_{N_{G1},1}^2 + n_{21} \dot{\theta}_{N_{G1},1} \dot{\theta}_{N_{G2}-1,2} + \dot{\theta}_{N_{G2}-1,2}^2 \right) \\ T_{N_{G2},2}^{(s)} &= \frac{I_{N_{G2},2}^{(s)}}{6} \left( n_{21}^2 \dot{\theta}_{N_{G1},1}^2 + n_{21} \dot{\theta}_{N_{G1},1} \dot{\theta}_{N_{G2}+1,2} + \dot{\theta}_{N_{G2}+1,2}^2 \right) \end{aligned} \quad (3.31)$$

The following *distributed mass* matrix contributions of these two rotor-2 shaft elements are thus obtained, similar to Equation 3.17:

$$\begin{aligned}
\frac{d}{dt} \left( \frac{\partial T_{N_{G2}-1,2}^{(s)}}{\partial \dot{\theta}_{N_{G2}-1,2}} \right) &= \frac{1}{6} n_{21} I_{N_{G2}-1,2}^{(s)} \ddot{\theta}_{N_{G1},1} + \frac{1}{3} I_{N_{G2}-1,2}^{(s)} \ddot{\theta}_{N_{G2}-1,2} \\
\frac{d}{dt} \left( \frac{\partial T_{N_{G2},2}^{(s)}}{\partial \dot{\theta}_{N_{G1},1}} \right) &= \frac{1}{3} n_{21}^2 I_{N_{G2},2}^{(s)} \ddot{\theta}_{N_{G1},1} + \frac{1}{6} n_{21} I_{N_{G2},2}^{(s)} \ddot{\theta}_{N_{G2}+1,2} \\
\frac{d}{dt} \left( \frac{\partial T_{N_{G2},2}^{(s)}}{\partial \dot{\theta}_{N_{G2},2}} \right) &= \frac{1}{6} n_{21} I_{N_{G2},2}^{(s)} \ddot{\theta}_{N_{G1},1} + \frac{1}{3} I_{N_{G2},2}^{(s)} \ddot{\theta}_{N_{G2}+1,2}
\end{aligned} \tag{3.32}$$

Equations 3.30 and 3.32 contain all the terms needed to merge rotor-1 and rotor-2 mass matrices.

The following formulation details for merging rotor-1 and rotor-2 stiffness matrices are developed using the potential energy term of the Lagrange formulation, the same procedure as used to develop Equations 3.18 and 3.19.

$$\begin{aligned}
V_{N_{G2}-1,2} &= \frac{1}{2} K_{N_{G2}-1,2} (\theta_{N_{G2},2} - \theta_{N_{G2}-1,2})^2 \\
V_{N_{G2},2} &= \frac{1}{2} K_{N_{G2},2} (\theta_{N_{G2}+1,2} - \theta_{N_{G2},2})^2
\end{aligned} \tag{3.33}$$

Substituting from Equation 3.28 for  $\theta_{N_{G2},2}$  into Equation 3.33 thus leads to the following terms for merging rotor-1 and rotor-2 stiffness matrices:

$$\begin{aligned}
\frac{\partial V_{N_{G2}-1,2}}{\partial \theta_{N_{G1},1}} &= K_{N_{G2}-1,2} (n_{21}^2 \theta_{N_{G1},1} - n_{21} \theta_{N_{G2}-1,2}) \\
\frac{\partial V_{N_{G2}-1,2}}{\partial \theta_{N_{G2}-1,2}} &= K_{N_{G2}-1,2} (-n_{21} \theta_{N_{G1},1} + \theta_{N_{G2}-1,2}) \\
\frac{\partial V_{N_{G2},2}}{\partial \theta_{N_{G1},1}} &= K_{N_{G2},2} (n_{21}^2 \theta_{N_{G1},1} - n_{21} \theta_{N_{G2}+1,2}) \\
\frac{\partial V_{N_{G2},2}}{\partial \theta_{N_{G2},2}} &= K_{N_{G2},2} (-n_{21} \theta_{N_{G1},1} + \theta_{N_{G2}+1,2})
\end{aligned} \tag{3.34}$$

### 3.4.3.2 Flexible Connections

As a torsionally flexible connection between rotor-2's station  $N_{P2}$  and rotor-3's station  $N_{P3}$ , the pulley-belt set in Figure 3.4 needs no corresponding modifications to the mass matrix of either of the two rotors. Following the identical procedure used to develop Equations 3.20 and 3.21, the formulation details for merging the rotor-2 and rotor-3 stiffness matrices are as follows:

$$\begin{aligned} V_b &= \frac{1}{2}(2k_b)(\theta_{N_{P2},2}R_2 - \theta_{N_{P3},3}R_3)^2 \\ &= k_b(\theta_{N_{P2},2}^2R_2^2 - 2\theta_{N_{P2},2}\theta_{N_{P3},3}R_2R_3 + \theta_{N_{P3},3}^2R_3^2) \end{aligned} \quad (3.35)$$

$$\begin{aligned} \frac{\partial V_b}{\partial \theta_{N_{P2},2}} &= 2k_b(\theta_{N_{P2},2}R_2^2 - \theta_{N_{P3},3}R_2R_3) \\ \frac{\partial V_b}{\partial \theta_{N_{P3},3}} &= 2k_b(-\theta_{N_{P2},2}R_2R_3 + \theta_{N_{P3},3}R_3^2) \end{aligned} \quad (3.36)$$

As explained in Equation 3.20, this formulation is applicable to *flexible gear sets*.

At this point, all components needed to write the equations of motion for the TRV system in Figure 3.4 are ready for implementation.

---

## RDA Code for Lateral Rotor Vibration Analyses

---

### 4.1 Introduction

The RDA Fortran computer code is a general purpose tool for linear rotor vibration analyses. It is developed on the FE formulations derived in Chapter 2, Section 2.3. First written for use on early generation PCs, it was initially limited to fairly simple rotor-bearing configuration models with 10 or less mass stations (40 DOFs or less) because of the memory limitations of early PCs. RDA was initially written to simulate rotor-bearing systems as part of research efforts on *active control of rotor vibration* in the author's group at Case Western Reserve University (CWRU). Validation tests and other background information for RDA are provided by Maghraoui (1989) in his PhD dissertation (see Bibliography at the end of this chapter). RDA has been distributed and used by the author in *machinery dynamics* courses and student research projects at CWRU for over 20 years and in professional short courses in the United States and Europe. The current enlarged version supplied with this book, RDA99, has now been exercised by countless users since being provided free with the 2001 first edition of this book. RDA99 has been successfully used by the author in modeling several large power plant machinery, in vibration troubleshooting missions (see Part 4 of this book). It has also been successfully used by the author in troubleshooting and redesigning a high-speed vertical spin-pit test rig specially configured for research on aircraft jet engine blade-on-casing tip-rub-induced blade vibrations and transmitted blade-casing interaction dynamic forces.

The compiled code included here has been dimensioned to accommodate up to 99 rotor mass stations (396 DOF rotor), making it suitable for virtually any single-drive-line rotor-bearing system, including large steam turbo-generator rotors as subsequently demonstrated in Part 4 of this book. The author and his troubleshooting associates still use this newer RDA99 as the primary rotor vibration analysis tool both for troubleshooting work in plants as well as research.

As demonstrated in this chapter, RDA99 is a *user-interactive* code and thus does not utilize the *batch-mode* input approach typical of older computer codes written in the era of older mainframe computers. RDA99

has interactive input and output selection menus, each with several options. Not all these options are demonstrated here. Only the ones that are the most expedient for design or troubleshooting applications are demonstrated here.

There are many quite useful PC codes that were initially developed to run in the DOS environment prior to the introduction of Windows. The RDA executable code (RDA99.exe), supplied with this book, is but one example. The DOS operating system, developed for first-generation PCs and the forerunner of Windows, has therefore naturally been retained as an application within Windows. Earlier versions of Windows are actually an application within DOS. **RDA99.exe** will execute successfully on any PC as a DOS application within Windows.

Within the DOS operation mode, RDA99 is accessed simply by entering the appropriate drive and folder. Execution is then initiated simply by entering **RDA99**. The monitor then displays the following main menu.

```

~~~~~
ROTOR DYNAMICS ANALYSIS
~~~~~

      MAIN MENU

1. Solve the Undamped Eigenvalue Problem Only
2. Solve for Damped Eigenvalues Only
3. Solve Both Damped and Undamped Eigenvalue Problems
4. Perform a Stability Analysis of the System
5. Obtain the Steady-State Unbalance Response
6. Active Control Simulation
7. Data Curve Fitting By Cubic Spline
8. Exit
Choose Option <1-8> ...

```

All the MAIN MENU options are covered in Maghraoui (1989). When accessed by entering its number, each displays the DATA MENU from which the INPUT OPTIONS menu is accessed. Vibration specialists may wish to use options 1, 2, and 3 of the MAIN MENU to construct maps of eigenvalues as functions of rotor spin speed, and these are demonstrated in Maghraoui (1989). Options 6 and 7 may be ignored. MAIN MENU options 4 and 5 are the most important and useful ones. Therefore, the detailed instructions covered in this chapter are focused exclusively on options 4 and 5.



---

# 5

---

## *Bearing and Seal Rotor Dynamics*

---

---

### 5.1 Introduction

RDA, the modern FE-based PC code supplied with this book, is presented from a fundamentals perspective in Chapter 2 and a user's perspective in Chapter 4. There are a number of commercially available codes with similar capabilities. Engineering analysis codes in general and rotor dynamics codes in particular nearly always have one tacit fundamental trait in common. That trait is as follows:

Those aspects of the problem class that are reasonably well defined and modeled by first principles are what is "inside" the computer code. Whereas, those aspects which are not as well defined and modeled by first principles show up as some of the "inputs" to the computer code.

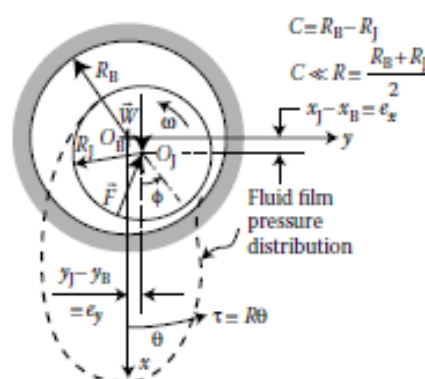
With this approach, the typical computer code developer and marketer has long been quick to tout their code as capable of handling "any" conceivable problem within the code's intended range of usage, *as long as one has all the "correct" inputs.*

For LRV analyses, those important inputs that present the biggest challenge are the dynamic properties (stiffness, damping, and inertia coefficients) for the components that *dynamically connect* the rotor to the stator (stator  $\equiv$  everything that does not rotate). These components include first and foremost the *radial bearings*. In many rotating machinery types (e.g., turbo-machinery) other liquid- and gas-filled internal close-clearance annular gaps, such as seals, are also of considerable LRV importance. Furthermore, the confined liquid or gas that surrounds a rotor component (e.g., centrifugal pump impeller and balancing drum) may also significantly contribute to the basic vibration characteristics of a rotating machine, both in an interactive way much like bearings and seals, and as explicit time-dependent unsteady-flow forces (e.g., hydraulic instability in centrifugal pumps, rotating stall in turbo-compressors). Motor and generator electromagnetic forces also contribute. Most modern LRV research has been devoted to all these rotor-stator effects. One could justifiably devote an entire book just to this single aspect of LRV. This chapter focuses on bearing and seal LRV dynamic properties. Small clearances critical to these properties are of significant uncertainty because of manufacturing tolerances.



### 5.2.1 Reynolds Lubrication Equation

The general starting point for modeling fluid mechanics problems is encompassed in the three coupled *fluid-momentum PDEs* [Navier–Stokes (N–S) equations] plus the single *conservation-of-mass PDE* (continuity equation). The three scalar N–S equations (which are nonlinear) are obtained by applying Newton’s Second Law  $\Sigma \vec{F} = d(m\vec{v})/dt$  to an inertial differential control volume (CV) of a continuum flow field. Attempting to solve these equations for 2D and 3D problems has historically been the challenge to occupy the careers of fluid mechanics theoreticians, because these equations are nonlinear and coupled. The ingenious contributions of the precomputer age fluid mechanics “giants” (like Osborne Reynolds) sprang from the application of their considerable physical insight into specific problems, leading them to make justifiable simplifying assumptions, thereby producing important solvable formulations. This was tantamount



**FIGURE 5.1** Generic journal bearing configuration and nomenclature.

### 5.2.1.1 For a Single RLE Solution Point

1. Specify  $e \equiv \sqrt{e_x^2 + e_y^2}$ ,  $\phi = \arctan(e_y/e_x)$ ,  $e_x = x_J - x_B$ ,  $e_y = y_J - y_B$   
With journal-to-bearing axial alignment,  $h = C - e_x \cos(\tau/R) - e_y \sin(\tau/R)$  giving  $(dh/d\tau) = (e_x/R) \sin(\tau/R) - (e_y/R) \cos(\tau/R)$ ,  $\dot{h} = -\dot{e}_x \cos(\tau/R) - \dot{e}_y \sin(\tau/R)$
2. Solve the RLE for the pressure distribution  $p = p(\tau, z)$
3. Integrate  $p(\tau, z)$  over the journal cylindrical surface to get  $x$  and  $y$  forces upon the journal:

$$\begin{aligned} F_x &= - \int_{-L/2}^{L/2} \int_0^{2\pi R} p(\tau, z) \cos(\tau/R) d\tau dz \\ F_y &= - \int_{-L/2}^{L/2} \int_0^{2\pi R} p(\tau, z) \sin(\tau/R) d\tau dz \end{aligned} \quad (5.2)$$

In a numerical finite-difference solution for  $p(\tau, z)$ , the pressure is determined only at the grid points of a 2D rectangular mesh. The above integrations are then done numerically, such as by using Simpson's rule.

4. Calculate resultant radial load and its angle:

$$W = \sqrt{F_x^2 + F_y^2}, \quad \theta_W = \arctan(F_y/F_x) \quad (5.3)$$

By performing the above steps, 1 through 4, over a suitable range of values for  $0 \leq e/C < 1$  and  $\phi$ , enough solution points are generated to construct design curves similar to those of Raimondi and Boyd. As stated earlier, the sequence of computations in design analyses is the reverse of the above sequence. That is, one starts by specifying the bearing load,  $W$ , and its angle  $\theta_W$ , and uses design curves preassembled from many RLE solutions to determine the corresponding journal eccentricity,  $e$ , and attitude angle,  $\phi$ .

### 5.2.2 Journal Bearing Stiffness and Damping Formulations

Solutions to the RLE are a nonlinear function of the journal-to-bearing radial displacement or eccentricity, even though the RLE itself is a linear

differential equation. Thus,  $F_x$  and  $F_y$  given by Equations 5.2 are nonlinear (but continuous) functions of journal-to-bearing motion. Therefore, they may each be expanded in a Taylor series about the static equilibrium position. For sufficiently "small" motions, the corresponding changes in the journal fluid-film force components about equilibrium can thus be linearized for displacement and velocity perturbations, as indicated by Equations 2.60.

Since solutions for the fluid-film radial force components  $F_x$  and  $F_y$  are usually obtained through numerical integration on  $p(\tau, z)$  as it is obtained from numerical solution of the RLE, the *partial derivatives* of  $F_x$  and  $F_y$  that are the bearing *stiffness and damping* coefficients must also be numerically computed. This is shown by the following equations:

$$\begin{aligned}
 -k_{xx} &\equiv \frac{\partial F_x}{\partial x} \approx \frac{\Delta F_x}{\Delta x} = \frac{F_x(x + \Delta x, y, 0, 0) - F_x(x, y, 0, 0)}{\Delta x} \\
 -k_{yx} &\equiv \frac{\partial F_y}{\partial x} \approx \frac{\Delta F_y}{\Delta x} = \frac{F_y(x + \Delta x, y, 0, 0) - F_y(x, y, 0, 0)}{\Delta x} \\
 -k_{xy} &\equiv \frac{\partial F_x}{\partial y} \approx \frac{\Delta F_x}{\Delta y} = \frac{F_x(x, y + \Delta y, 0, 0) - F_x(x, y, 0, 0)}{\Delta y} \\
 -k_{yy} &\equiv \frac{\partial F_y}{\partial y} \approx \frac{\Delta F_y}{\Delta y} = \frac{F_y(x, y + \Delta y, 0, 0) - F_y(x, y, 0, 0)}{\Delta y} \\
 -c_{xx} &\equiv \frac{\partial F_x}{\partial \dot{x}} \approx \frac{\Delta F_x}{\Delta \dot{x}} = \frac{F_x(x, y, \Delta \dot{x}, 0) - F_x(x, y, 0, 0)}{\Delta \dot{x}} \\
 -c_{yx} &\equiv \frac{\partial F_y}{\partial \dot{x}} \approx \frac{\Delta F_y}{\Delta \dot{x}} = \frac{F_y(x, y, \Delta \dot{x}, 0) - F_y(x, y, 0, 0)}{\Delta \dot{x}} \\
 -c_{xy} &\equiv \frac{\partial F_x}{\partial \dot{y}} \approx \frac{\Delta F_x}{\Delta \dot{y}} = \frac{F_x(x, y, 0, \Delta \dot{y}) - F_x(x, y, 0, 0)}{\Delta \dot{y}} \\
 -c_{yy} &\equiv \frac{\partial F_y}{\partial \dot{y}} \approx \frac{\Delta F_y}{\Delta \dot{y}} = \frac{F_y(x, y, 0, \Delta \dot{y}) - F_y(x, y, 0, 0)}{\Delta \dot{y}}
 \end{aligned} \tag{5.4}$$

$$-c_{xy} \equiv \frac{\partial F_x}{\partial \dot{y}} \simeq \frac{\Delta F_x}{\Delta \dot{y}} = \frac{F_x(x, y, 0, \Delta \dot{y}) - F_x(x, y, 0, 0)}{\Delta \dot{y}}$$

$$-c_{yy} \equiv \frac{\partial F_y}{\partial \dot{y}} \simeq \frac{\Delta F_y}{\Delta \dot{y}} = \frac{F_y(x, y, 0, \Delta \dot{y}) - F_y(x, y, 0, 0)}{\Delta \dot{y}}$$

Here,  $x \equiv e_x$ ,  $y \equiv e_y$ ,  $\dot{x} \equiv \dot{e}_x$ ,  $\dot{y} \equiv \dot{e}_y$ .

The definitions contained in Equations 5.4 for the eight *stiffness and damping* coefficients are compactly expressed using subscript notation, as follows:

$$k_{ij} \equiv -\frac{\partial F_i}{\partial x_j} \quad \text{and} \quad c_{ij} \equiv -\frac{\partial F_i}{\partial \dot{x}_j} \quad (5.5)$$

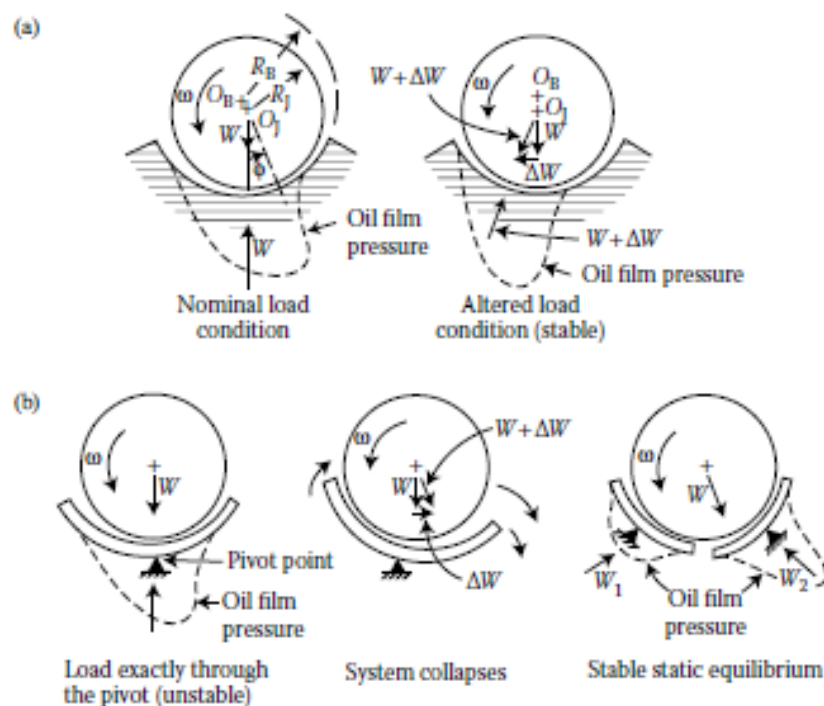
It is evident from Equations 5.4 that the journal radial force components  $F_x$  and  $F_y$  are expressible as continuous functions of journal-to-bearing radial displacement and velocity components, as follows:

$$F_x = F_x(x, y, \dot{x}, \dot{y})$$

$$F_y = F_y(x, y, \dot{x}, \dot{y}) \quad (5.6)$$

It is also evident from Equations 5.4 that for each selected static equilibrium operating condition  $(x, y, 0, 0)$ , five solutions of the RLE are required to compute the eight *stiffness and damping* coefficients. These five slightly different solutions are tabulated as follows:

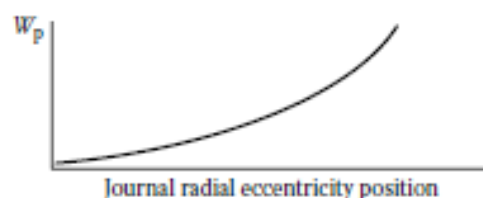
- $(x, y, 0, 0)$ , Equilibrium condition,
- $(x + \Delta x, y, 0, 0)$ ,  $x$ —displacement perturbation about equilibrium,
- $(x, y + \Delta y, 0, 0)$ ,  $y$ —displacement perturbation about equilibrium,
- $(x, y, \Delta \dot{x}, 0)$ ,  $x$ —velocity perturbation about equilibrium,
- $(x, y, 0, \Delta \dot{y})$ ,  $y$ —velocity perturbation about equilibrium.



**FIGURE 5.3** Comparison between cylindrical and tilting-pad journal bearings: (a) cylindrical bearing arc and (b) tilting-pad bearing.

three equally spaced pads, a load passing directly through one of the pivot points does not cause the bearing to collapse because the three or more pads at least capture the journal. But even with three or more pads, a load that is supported mostly by a single pad can produce poor rotor dynamical characteristics. By restraining a single pad pivot and journal (test setup or simulation), the load capacity of a single pad is obtained as a function of journal pivot radial eccentricity as typified by Figure 5.4, where the slope is pad pivot *radial film stiffness*.

It is seen that the pad radial film stiffness acts as a nonlinear spring in compression. Consider the four-pad bearing, illustrated in Figure 5.5 for two loading conditions: (a) load between two pads and (b) load on a





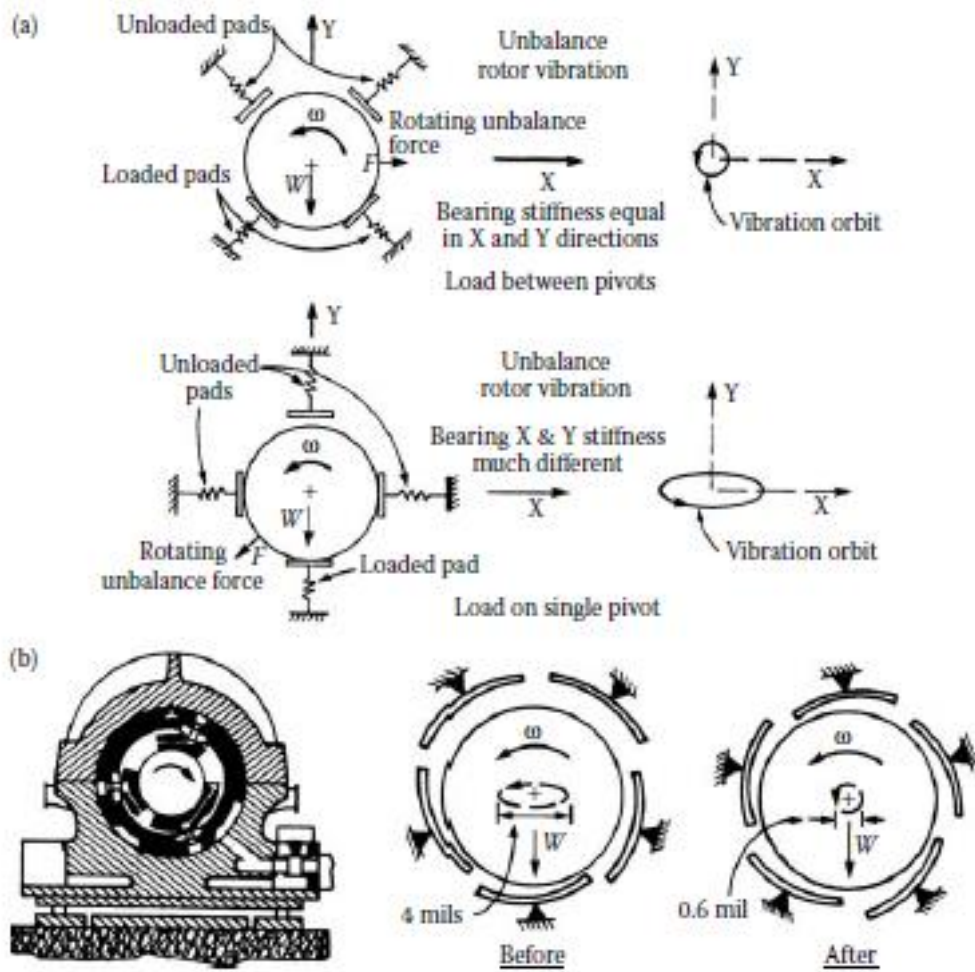


FIGURE 5.5 Load-direction vibration factors of tilting-pad journal bearings.

#### 5.2.4.1 Tables of Dimensionless Stiffness and Damping Coefficients

The bearing data files in the directory **BearCoef** use the standard non-dimensionalization most frequently employed for journal bearing rotor dynamic coefficients, as defined by the following dimensionless parameters for stiffness ( $\bar{k}_{ij}$ ) and damping ( $\bar{c}_{ij}$ ) as functions of a dimensionless speed,  $S$ :

$$\bar{k}_{ij} \equiv \frac{k_{ij}C}{W}, \quad \bar{c}_{ij} \equiv \frac{c_{ij}\omega C}{W}, \quad S \equiv \frac{\mu n}{P} \left( \frac{R}{C} \right)^2 \quad (5.8)$$

where  $C$  is the radial clearance,  $W$  is the static load,  $S$  is the Sommerfeld number,  $\mu$  is the lubricant viscosity,  $P = W/DL$ , the unit load,  $R$  is the nominal radius,  $D = 2R$ ,  $L$  is the length, and  $n$  (revs/s)  $= \omega/2\pi$ .



$$(m_s + m_f)\ddot{x}_f + c_f\dot{x}_f + k_fx_f = F_se^{i\omega t}$$

$$x_f = Xe^{i(\omega t + \phi)}$$
(5.10)

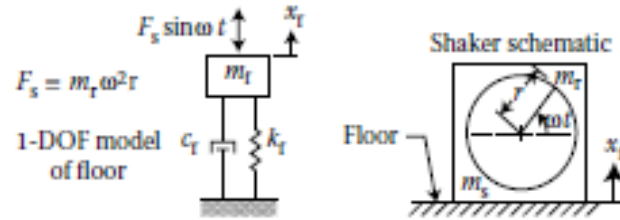


FIGURE 5.9 Vertical shaker test of floor where a machine is to be installed.

Equations 5.10 lead to the following complex algebraic equation:

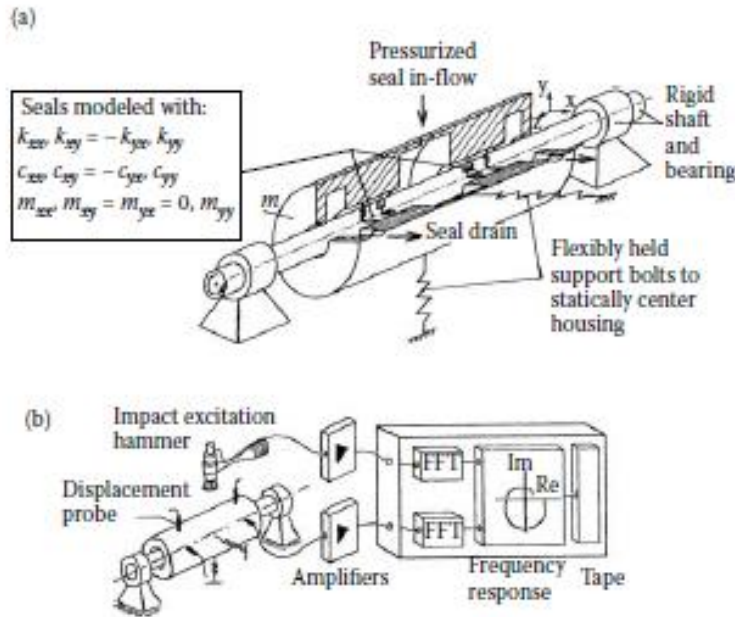
$$(k_f - \omega^2 m_f - \omega^2 m_s + ic_f \omega)Xe^{i\phi} = F_s$$
(5.11)

$$x = X e^{i(\Omega t + \phi_x)}, \quad y = Y e^{i(\Omega t + \phi_y)}, \quad f_x = F_x e^{i(\Omega t + \theta_x)}, \quad f_y = F_y e^{i(\Omega t + \theta_y)} \quad (5.12)$$

where  $\Omega$  is the orbital frequency. (Here,  $\Omega$  is not necessarily equal to  $\omega$ , the rotational speed.)

Equations 5.12 are substituted into Equations 5.9 to yield two complex equations. The basic formula  $e^{iz} = \cos z + i \sin z$  separates real and imaginary parts of the resulting two complex equations, to yield the following four real equations:

$$\begin{aligned} F_x \cos \theta_x &= \left[ (\Omega^2 m_{xx} - k_{xx}) \cos \phi_x + c_{xx} \Omega \sin \phi_x \right] X \\ &\quad + \left[ (\Omega^2 m_{xy} - k_{xy}) \cos \phi_y + c_{xy} \Omega \sin \phi_y \right] Y \\ F_x \sin \theta_x &= \left[ (\Omega^2 m_{xx} - k_{xx}) \sin \phi_x - c_{xx} \Omega \cos \phi_x \right] X \\ &\quad + \left[ (\Omega^2 m_{xy} - k_{xy}) \sin \phi_y - c_{xy} \Omega \cos \phi_y \right] Y \\ F_y \cos \theta_y &= \left[ (\Omega^2 m_{yx} - k_{yx}) \cos \phi_x + c_{yx} \Omega \sin \phi_x \right] X \\ &\quad + \left[ (\Omega^2 m_{yy} - k_{yy}) \cos \phi_y + c_{yy} \Omega \sin \phi_y \right] Y \\ F_y \sin \theta_y &= \left[ (\Omega^2 m_{yx} - k_{yx}) \sin \phi_x - c_{yx} \Omega \cos \phi_x \right] X \\ &\quad + \left[ (\Omega^2 m_{yy} - k_{yy}) \sin \phi_y - c_{yy} \Omega \cos \phi_y \right] Y \end{aligned} \quad (5.13)$$



**FIGURE 5.11** Experimental setup for impact excitation of radial seals: (a) quarter through-cut schematic illustration of test apparatus and (b) schematic of test measurements and data processing.

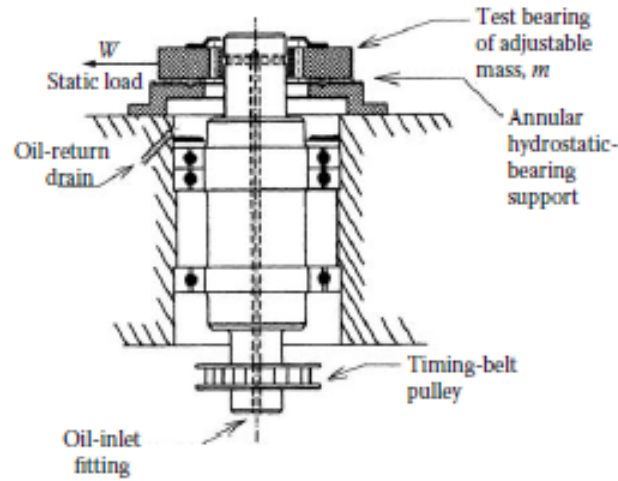
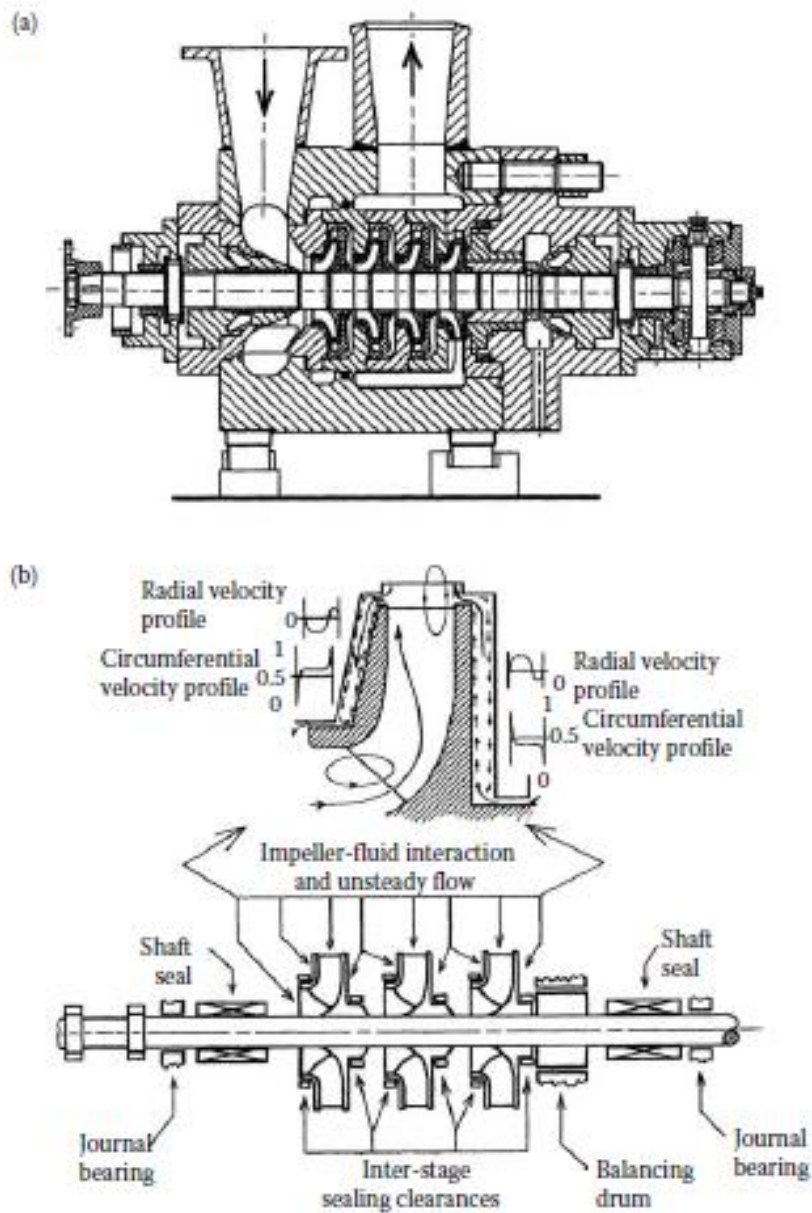


FIGURE 5.12 Vertical spindle rig for controlled instability-threshold-speed tests.

at selected operating conditions spanning a wide range of journal bearing Sommerfeld numbers (dimensionless speed). The controlled test parameters are rotational *speed*, bearing static radial *load*, lubricant *viscosity*, and test bearing *mass*. As with *mechanical impedance approaches*, the experiment mentioned here is correlated with a 2-DOF model given by the following equations:

$$\begin{aligned}
 m\ddot{x} + c_{xx}\dot{x} + k_{xx}x + c_{xy}\dot{y} + k_{xy}y &= 0 \\
 m\ddot{y} + c_{yy}\dot{y} + k_{yy}y + c_{yx}\dot{x} + k_{yx}x &= 0 \\
 c_{xy} &\equiv c_{yx}
 \end{aligned}
 \tag{5.15}$$



**FIGURE 5.13** Multistage BFP: (a) pump cross section and (b) sources of interaction and unsteady-flow rotor forces.

### 5.4.2 Ungrooved Annular Seals for Liquids

Three commonly used versions of *ungrooved annular seal* geometries are shown in Figure 5.14, with exaggerated clearances for illustrative purposes, as done with the journal bearing illustration in Figure 5.1. Although these ungrooved seals bear some geometric similarity to journal bearings, essential differences distinguish them. First, in most high-pressure applications the fluid being sealed is not a viscous oil but a much lower viscosity liquid like water or other process liquids or gases. The *flow* within the seal

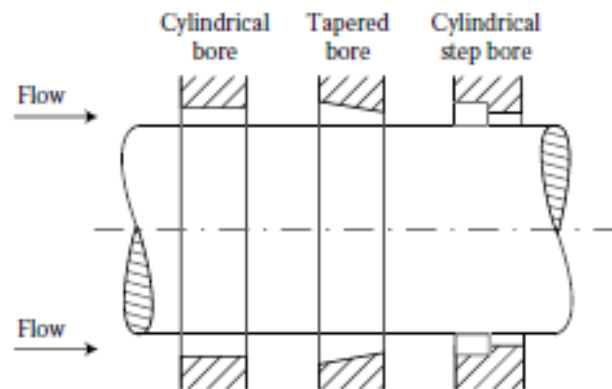


FIGURE 5.14 Ungrooved annular seals (illustrated clearances exaggerated).

clearance is thus usually *turbulent*, in contrast to most oil-film journal bearings that are characterized by the *laminar flow* RLE, Equation 5.1. Second, such seals usually have an axial length much smaller than the diameter (typically  $L/D < 0.1$ ).

#### 5.4.2.1 Lomakin Effect

The first person to publish about the influence of ungrooved annular seals on rotor vibration was Lomakin (1955, 1958). Figure 5.15 illustrates how a

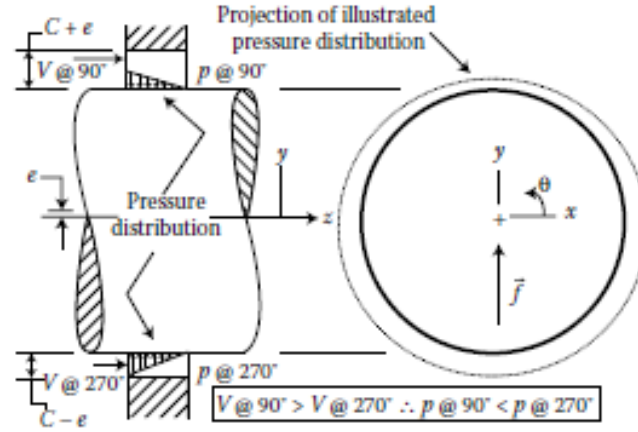


FIGURE 5.15 Lomakin effect pressure distribution in an ungrooved annular seal.

radial-pressure centering force is produced when the rotor and stator of an annular seal are eccentric to each other. Ignoring at this point the effects of shaft rotation and inlet flow preswirl, the entrance pressure loss is highest where the radial gap and thus the inlet flow velocity are largest. Conversely, the entrance pressure loss is lowest where the radial gap and thus the inlet flow velocity are smallest. This effect thus produces a *radial centering force* on the rotor, which increases with eccentricity between seal rotor and stator. That is, the radial displacement causes a skewing of the pressure distribution, producing a *radial stiffness effect* that is called the “Lomakin” effect. The  $x$  and  $y$  components of the centering force are expressible by directionally integrating the pressure distribution as shown in Equations 5.2 for journal bearings. In this simplest embodiment of the Lomakin effect, with shaft rotation and inlet flow prerotation not included, the centering force vector ( $\vec{f}$ ) is in line with the eccentricity ( $e$ ) and thus its magnitude is expressible as follows:

$$f = - \int_0^L \int_0^{2\pi} p(\theta, z) R \sin \theta d\theta dz \quad (5.17)$$



$$f = - \int_0^L \int_0^{2\pi} p(\theta, z) R \sin \theta d\theta dz \quad (5.17)$$

In precisely the same manner described for journal bearings, the centering force described by Equation 5.17 can be linearized for “small” eccentricities, thus yielding a radial stiffness coefficient as follows:

$$k_r = \frac{f}{e} \approx 0.4 \frac{\Delta p R L}{C} \quad (5.18)$$

where  $\Delta p$  is the pressure drop,  $R$  is the seal radius,  $L$  is the seal length, and  $C$  is the seal radial clearance.

#### 5.4.2.3 Bulk Flow Model Approach

Consistent with the brief description of the RLE provided in Section 5.2.1, the aim here is not to provide all the intricate derivation steps in applying the BFM to annular seals. Instead, the intent here is to facilitate the serious reader’s understanding of available derivations of an annular seal BFM, such as that detailed by Childs (1993). To that end, the following perspective is provided.

The BFM employs standard control volume (CV) formulation as covered in fluid mechanics courses of undergraduate mechanical engineering programs. In this application, the CV is a small arbitrary volume of fluid within the seal (Figure 5.16), bounded by seal rotor and stator surfaces, and by infinitesimal differential sides in the axial and circumferential directions. In fact, this is just how Reynolds set up the development of the RLE, except that variation of fluid velocities across the clearance gap are of paramount importance in laminar oil-film bearings and thus are not neglected as they are in the BFM approach.

Fluid flow mass balance for this CV is satisfied by the continuity (mass conservation) equation. Application of Newton’s Second Law ( $\vec{F} = m\vec{a}$ ) to this CV leads to two coupled PDEs, one for *circumferential momentum* balance and one for *axial momentum* balance. As Childs (1993) implies, the continuity equation is satisfied by appropriately substituting it into each of the two momentum equations, which are in turn considerably simplified in that derivation step. Employing the coordinate system shown in Figure 5.16, the following two momentum equations for the BFM are thus obtained.

#### 5.4.2.4 Circumferential Momentum Equation

$$-\frac{h}{R} \frac{\partial p}{\partial \theta} = \frac{\rho}{2} u u_s f_s + \frac{\rho}{2} (u - R\omega) u_r f_r + \rho h \left( \frac{\partial u}{\partial t} + \frac{u}{R} \frac{\partial u}{\partial \theta} + w \frac{\partial u}{\partial z} \right) \quad (5.19)$$

#### 5.4.2.5 Axial Momentum Equation

$$-h \frac{\partial p}{\partial z} = \frac{\rho}{2} w u_s f_s + \frac{\rho}{2} w u_r f_r + \rho h \left( \frac{\partial w}{\partial t} + \frac{u}{R} \frac{\partial w}{\partial \theta} + w \frac{\partial w}{\partial z} \right) \quad (5.20)$$

$$\begin{aligned}
f_x(e, \Omega) &= - \int_0^L \int_0^{2\pi} \Delta p(\theta, z, e, \Omega) R \cos \theta \, d\theta \, dz \\
f_y(e, \Omega) &= - \int_0^L \int_0^{2\pi} \Delta p(\theta, z, e, \Omega) R \sin \theta \, d\theta \, dz
\end{aligned} \tag{5.21}$$

Since this perturbation force is a function of orbit frequency, it lends itself to a second-order polynomial curve fit in frequency that directly extracts the *isotropic model* coefficients of Equation 5.16. To that end, expressing the perturbation force by its orthogonal components referenced to the instantaneous *radial* and *tangential* directions of the circular perturbation orbit yields the following expressions (refer Figure 2.13):

$$f_R \cong -(k_s + \Omega c_{ss} - \Omega^2 m_s) e, \quad f_T \cong (k_{ss} - \Omega c_s) e \tag{5.22}$$

#### 5.4.2.6 Comparisons between Ungrooved Annular Seals and Journal Bearings

The majority of journal bearings operate with their hydrodynamic films in the laminar flow regime, in which case aligned journal bearings are characterized by two dimensionless parameters, Sommerfeld number (dimensionless speed) and  $L/D$ . In some applications, however, the combination of journal surface speed, lubricant viscosity, and bearing clearance place journal bearing hydrodynamic lubricating films into the turbulent regime. Conventional wisdom of the experts is that a quite good approximation for turbulence effects in journal bearings is based on the use of an *apparent viscosity*, which is locally made higher than the actual viscosity as a function of the local Reynolds numbers for journal velocity and localized parameters of pressure gradient and film thickness. This approach is provided by Elrod and Ng (1967). In the Elrod–Ng approach, the RLE Equation 5.1 for laminar lubricant films is still employed, albeit with the local viscosity at each finite-difference grid point modified to its local *apparent viscosity*. There is then an additional dimensionless number (e.g., clearance based Reynolds number) to characterize the journal bearing. The Elrod–Ng approach rests upon a fundamental assumption that temporal and convective inertia terms of the N–S equations are negligible even though it is fluid inertia at the film flow’s fine structure level that is an essential ingredient of the turbulence. Thus, even with turbulence effects included, the theory and characterization of hydrodynamic journal bearings is not appreciably different than for laminar hydrodynamic lubrication. In stark contrast, ungrooved annular seals are characterized by several nondimensional parameters, including, but not limited to, the following list of major ones:

$$\text{Pressure drop: } \frac{(p_{\text{in}} - p_{\text{out}})}{\rho w_0^2} \quad w_0 \equiv \frac{Q}{2\pi C}$$

$Q \equiv \text{seal through flow.}$

Axial and circumferential Reynolds numbers, respectively:

$$R_z = \frac{2w_0\rho C}{\mu}, \quad R_\theta = \frac{R\omega\rho C}{\mu}$$

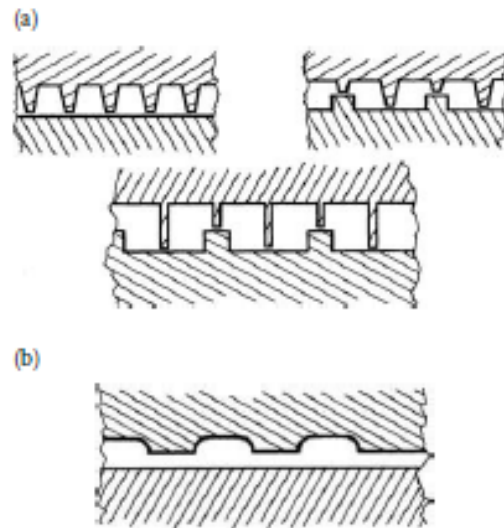
- *Clearance uncertainty* via seal rotor and stator diameter mfg. tolerances
- Variations in *fluid viscosity* from fluid temperature variations
- Seal rotor-to-stator *static eccentricity* (assumed zero for isotropic model)
- Seal rotor-to-stator tilt *misalignment*
- Seal *ring distortions* from loads, temperature gradients, wear, and so on
- Basic simplifying *assumptions* leading to the BFM governing equations
- Coefficients for entrance pressure loss and exit pressure recovery
- Entrance circumferential velocity (preswirl)
- Surface *roughness*.

### 5.4.3 Circumferentially Grooved Annular Seals for Liquids

Various fluid-annulus sealing zones, such as those shown in Figure 5.13, are not always ungrooved designs. Circumferential grooves are used in many designs to further reduce leakage flow between stages, through end seals and balancing drum (piston). The number of grooves, their axial spacing, width, and depth are not standardized parameters; different manufacturers have their own variation on the basic idea of circumferentially grooving to improve leakage reduction. The presence of such grooves also provides a more rub-forgiving less seizure-prone rotor-stator combination than without grooves. Grooves are employed on either rotor or stator. Figure 5.17 shows a variety of circumferential groove geometry for annular seals:

- a. Labyrinth seals; groove depth much larger than radial tip clearance.
- b. Shallow-grooves; groove depth approximately equal to tip clearance.

Published analysis and experimental results are sparse. Those cited by Childs (1993) suggest some trends. First, grooving significantly reduces LRV stiffness and damping effects, possibly as much as 80% reduction with wide deep grooves. Second, having the grooves on the seal stator



**FIGURE 5.17** Examples of circumferentially grooved annular seals: (a) labyrinth seals; groove depth much larger than radial tip clearance and (b) shallow grooves; groove depth approximately equal to tip clearance.

## 5.7 Magnetic Bearings

The generic configuration of an *active* magnetic bearing system is shown in Figure 5.21, which schematically illustrates the essential components.

The main feature of magnetic bearings which has attracted the attention of some rotating machinery designers is that they are *oil-free bearings*. This means for example that with large pipe line compressor rotors supported on oil-free bearings, the elimination of oil precludes the eventual coating of pipeline interior surfaces with lost oil that otherwise must be periodically cleaned out of the pipeline, at considerable service and downtime costs. Interestingly, this feature is not uppermost in the minds of magnetic bearing conceivers, who for the most part are academicians with a particular focus on control theory. They conceived the modern active magnetic bearing as an electromechanical actuator device that utilizes rotor position feedback to a controller in order for the magnetic bearing to provide electromagnetic

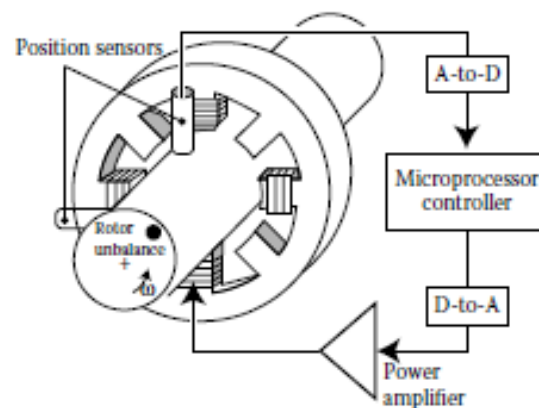


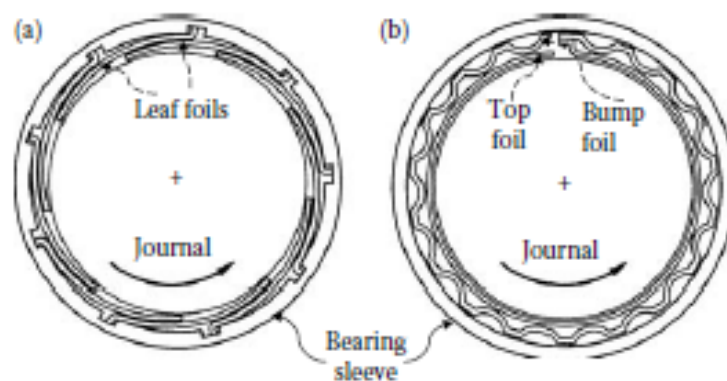
FIGURE 5.21 Active magnetic bearing schematic.



## 5.8 Compliance Surface Foil Gas Bearings

Gas film bearings of both hydrodynamic and hydrostatic functioning were already being investigated and used in a few novel applications nearly 50 years ago. However, use of those bearings never achieved wide industrial use, primarily because of quite low load capacity at modest rotational speeds and rotor dynamical instability problems at speeds sufficiently high to provide useable static load capacities. Hydrostatic gas bearings utilizing porous media bearing sleeves were also shown to be feasible in laboratory testing and analysis. The foil gas bearing concept achieved success in the predigital-age high-speed tape deck heads by manufacturers such as Ampex. The main modern application of the hydrodynamic air bearing, initially on mainframe computer high-speed flying-head disk readers, has found its present place in PC hard drives. Quite recently, a major Cleveland-based manufacturer of MRI medical scanners has successfully developed and employed hydrostatic air bearings to support the main rotational positioning barrel, advancing the position resolution in this product.

About 25 years ago the gas foil bearing concept evolved into a new family of configuration, namely the *compliance surface foil gas bearing* (Heshmat et al., 1982). Figure 5.23 illustrates two typical compliance surface foil gas



**FIGURE 5.23** Two types of compliant surface foil gas journal bearings: (a) leaf-type foil bearing and (b) bump-type foil bearing.

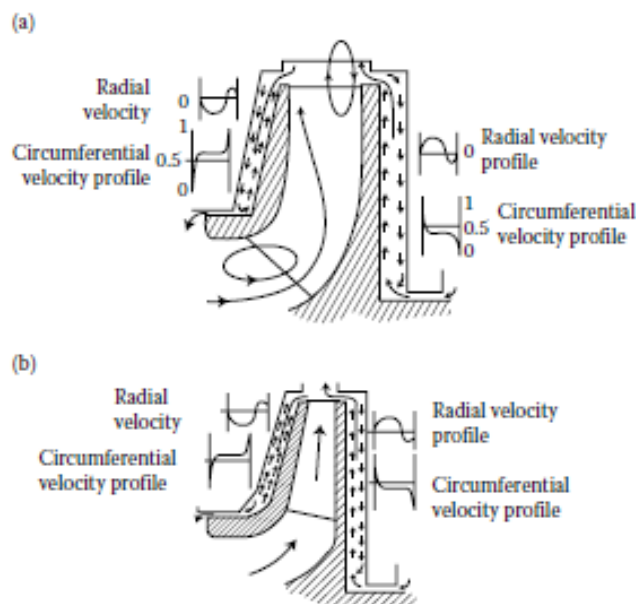
## 6.1 Centrifugal Pumps

Referring to Figure 6.1a, it is not surprising that static and dynamic hydraulic forces are imposed on the rotor of a centrifugal pump by the flow through the pump. These hydraulic rotor forces are dominant factors in determining the vibration behavior of a centrifugal pump, especially high-energy pumps such as those required for boiler feed water service.

### 6.1.1 Static Radial Hydraulic Impeller Force

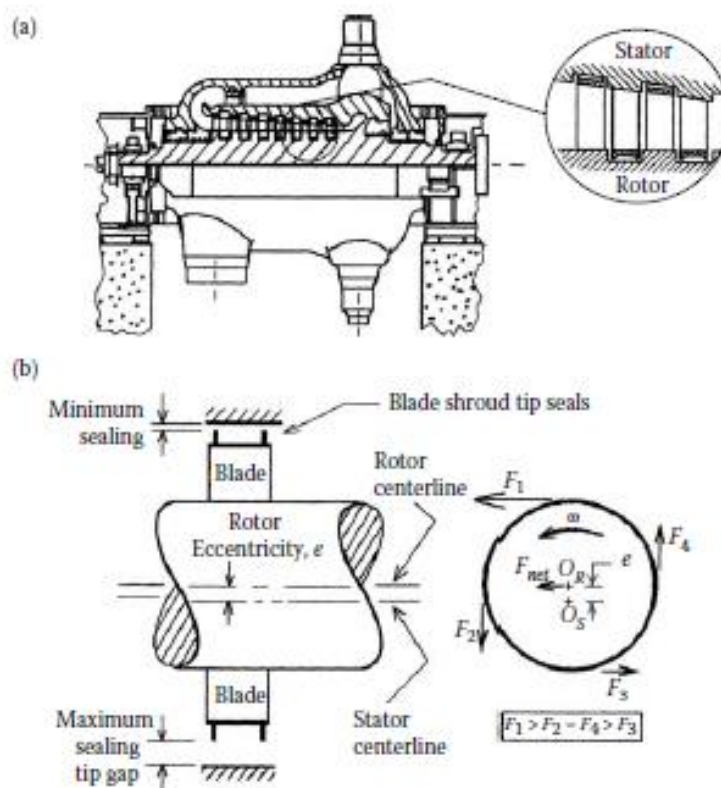
A *static radial force* is imposed on a pump impeller because the steady portion of the total pressure distribution over the impeller surface is not of perfect axial symmetry. This static radial hydraulic force is relatively larger in single-tongue volute-casing pumps, and smaller in multitongue volute-casing and diffuser-casing pumps. The combined static radial impeller force from all the impellers of a high-pressure multiimpeller pump, such as shown in Figure 5.13, can easily be much larger than the total weight of the pump rotating element. Thus, the static hydraulic impeller force can readily be the dominant factor in determining journal bearing static loads and thus the LRV stiffness and damping characteristics of the bearings. The static hydraulic radial force on an impeller varies considerably in magnitude and direction with pump flow. Therefore, the rotor dynamic properties of the journal bearings can vary considerably over the

251



$$P_s = \frac{K_s H D_2 B_2}{2.31} \quad (6.1)$$

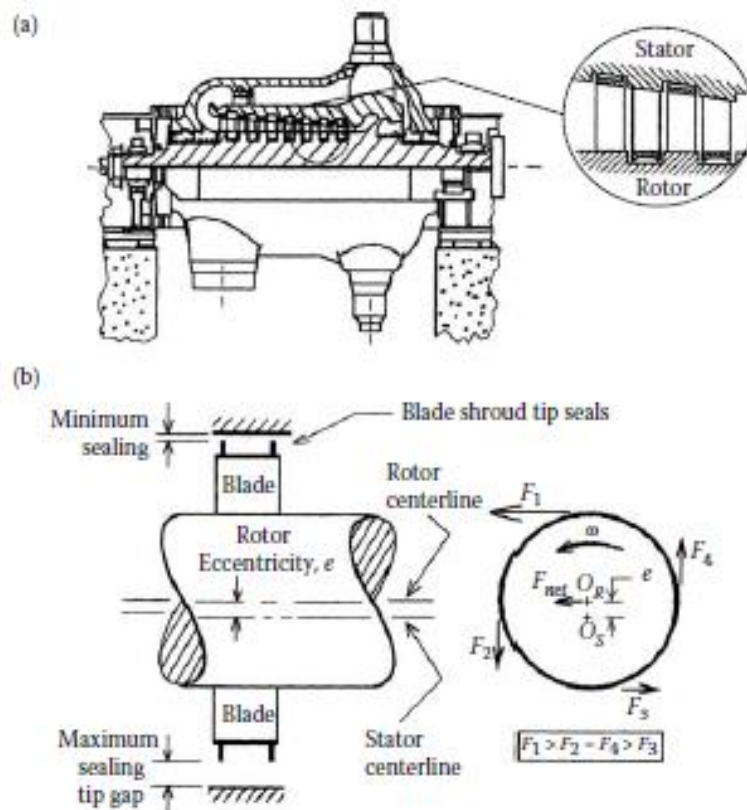
where  $P_s$  is the static force (pounds),  $H$  is the pump head (ft),  $D_2$  is the impeller outer diameter (in.),  $B_2$  is the impeller discharge width including



**FIGURE 6.2** Contribution to *steam whirl* from the “Thomas–Alford” effect: (a) sectional view of a single-flow high-pressure steam turbine and (b) nonuniform torque distribution resulting from eccentricity.

impeller side plates (in.), and  $K_s$  is the empirical coefficient that changes with pump flow approximately as follows:

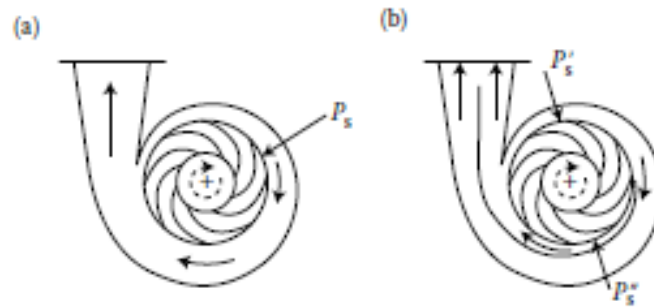
$$K_s = 0.36 \left[ 1 - \left( \frac{Q}{Q_{BEP}} \right)^2 \right], \quad \begin{array}{l} Q = \text{operating pump flow} \\ Q_{BEP} = \text{best efficient point pump flow} \end{array} \quad (6.2)$$



**FIGURE 6.2** Contribution to *steam whirl* from the “Thomas-Alford” effect: (a) sectional view of a single-flow high-pressure steam turbine and (b) nonuniform torque distribution resulting from eccentricity.

impeller side plates (in.), and  $K_s$  is the empirical coefficient that changes with pump flow approximately as follows:

$$K_s = 0.36 \left[ 1 - \left( \frac{Q}{Q_{BEP}} \right)^2 \right], \quad \begin{array}{l} Q = \text{operating pump flow} \\ Q_{BEP} = \text{best efficient point pump flow} \end{array} \quad (6.2)$$



**FIGURE 6.3** Static radial hydraulic force on volute-pump impellers: (a) single-volute pump and (b) double-volute pump,  $P_s = P'_s - P''_s$ .

reporting values for some single-volute pumps as high as 0.6 at shutoff operation.

The well-known *double-volute* (two tongues) configuration, as shown in Figure 6.3b, was devised to divide the pump volute into two equal 180° flow sections, with the intent that each section's static radial impeller force cancels the other's. The double volute does not completely accomplish that objective, but it does yield a drastic force reduction from that of a single-tongue volute. The author is familiar with centrifugal pump designs employing the *tri-volute* (three 120°-arc sections) and the *quad-volute* (four 90°-arc sections). Of course, if one further increases the number of volute tongues, the volute then resembles a diffuser.

Guelich et al. (1987) use the following less confusing form of Equation 6.1, which applies in any consistent system of units and explicitly shows density:

$$K_s = \frac{P_s}{\rho g H D_2 B_2} \quad (6.3)$$

where  $\rho$  is the mass density of the pumped liquid and  $g$  is the gravitational constant.



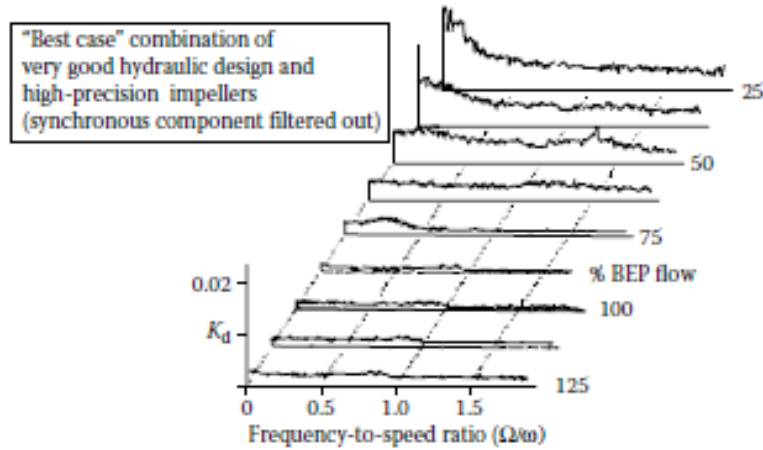


FIGURE 6.4 Spectra (rms) of normalized broadband impeller forces.

the BEP flow, the continuous strong increase in force magnitude results from impeller inlet and exit flow re-circulation (see Figure 6.1a) and flow separation.

#### 6.1.2.2 Interaction Impeller Forces

The handling of impeller LRV *interaction forces* that has evolved over the last 30 years is to *curve fit* experimental data to the same linear *isotropic* LRV model used for most annular seal LRV characterizations. The assumption typically invoked for annular seal LRV coefficient arrays is that the flow field is rotationally symmetric (Chapter 5), and this assumption leads to the *isotropic model* given by Equation 2.85. While this assumption is quite inappropriate for journal bearings, it has been justified for annular seals and yields considerable simplification of both computational and experimental methods to extract LRV coefficient arrays for annular seals. Conversely, the flow field of a centrifugal pump impeller is certainly not rotationally symmetric. Nevertheless, to simplify test rigs and minimize associated costs to extract pump impeller LRV coefficient arrays, initial experiments were based on the *isotropic model* given by Equation 2.85, rewritten as

$$\begin{Bmatrix} f_x \\ f_y \end{Bmatrix} = - \begin{bmatrix} k^s & k^{ss} \\ -k^{ss} & k^s \end{bmatrix} \begin{Bmatrix} x \\ y \end{Bmatrix} - \begin{bmatrix} c^s & c^{ss} \\ -c^{ss} & c^s \end{bmatrix} \begin{Bmatrix} \dot{x} \\ \dot{y} \end{Bmatrix} - \begin{bmatrix} m^s & m^{ss} \\ -m^{ss} & m^s \end{bmatrix} \begin{Bmatrix} \ddot{x} \\ \ddot{y} \end{Bmatrix} \quad (6.5)$$



- Journal bearing* operating with a liquid lubricant, an atmospheric ambient pressure, and thus cavitation formed slightly downstream of the minimum film thickness; pressure field governed by fluid viscosity (i.e., Reynolds Lubrication Equation).
- Journal bearing* operating with very high ambient pressure (e.g., pressurized water reactor (PWR) reactor coolant pump lower

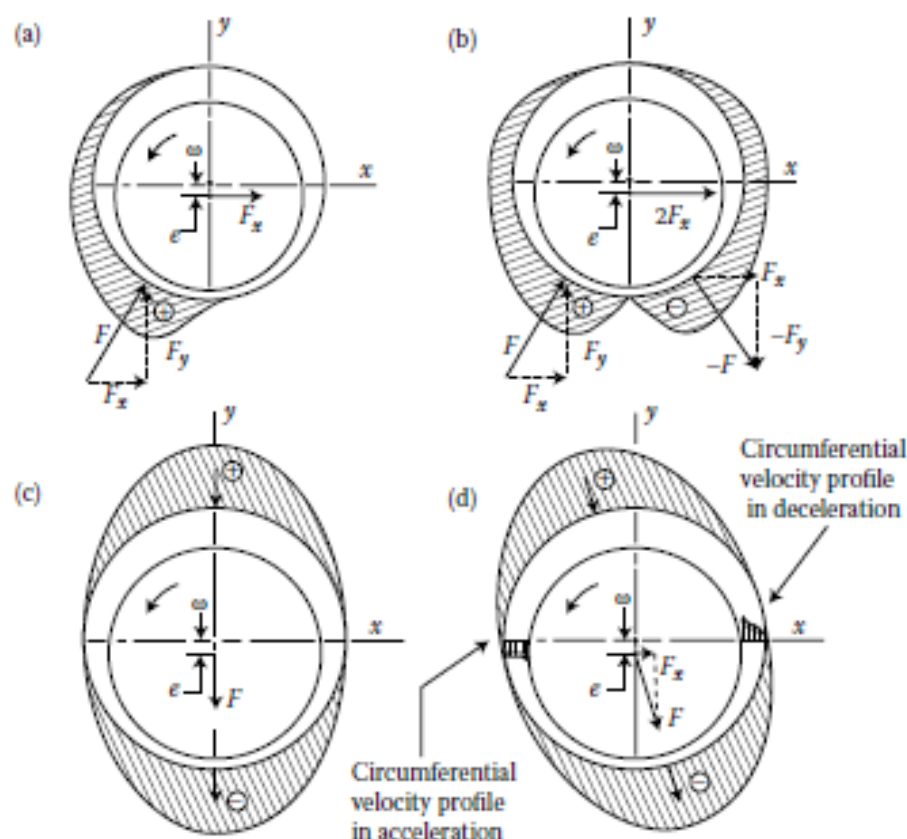


FIGURE 6.6 Circumferential pressure distributions relative to ambient: (a) journal bearing operating with atmospheric ambient pressure (cavitation); (b) journal bearing operating with high ambient pressure (no cavitation); (c) and (d) high rotational Reynolds number fluid annulus with high ambient pressure.

bearing; see Figure 12.1) and thus no cavitation; pressure field also governed by fluid viscosity.

- High rotational Reynolds number fluid annulus* in which the major inner core of fluid has a nearly "flat" circumferential velocity profile that is joined to the cylindrical boundaries through very thin boundary layers; pressure field governed by inertia of inner core of fluid.
- A slightly modified version of (c), which is the basis of the author's own explanation of the labyrinth seal contribution to steam whirl forces.

$$\text{Circumferential flow / unit axial length, } Q_\theta = \int_0^h V(r, \theta) dr = \text{constant} \quad (6.10)$$

A high rotational Reynolds number fluid annulus has its pressure field controlled by the fluid inertia in the inner core of circulating fluid. Thus, the clearance gap can be thought of as a Venturi meter wrapped around on itself and operating on the Bernoulli equation principle of conservation of energy, with maximum pressure occurring at the maximum radial gap and minimum pressure occurring at the minimum radial gap. With elevation and density changes discounted, the Bernoulli equation can be stated as follows:

$$p + \frac{\rho V^2}{2} = \text{constant} \quad (6.11)$$

where  $p$  is the pressure,  $V$  is the fluid velocity, and  $\rho$  is the fluid mass density.

If the kinetic energy term is based on the average velocity at each circumferential location ( $\theta$ ), then the pressure distribution in Figure 6.6c illustrates the result, and is based on the minimum possible local kinetic energy term (per unit of axial length), which is achieved with a perfectly flat velocity profile (zero thickness boundary layer), and is expressed as follows:

$$KE_{\min} = \frac{\rho(Q_\theta/h)^2}{2} \quad (6.12)$$